

## **UC Riverside**

### **UC Riverside Electronic Theses and Dissertations**

#### **Title**

Dynamic Self-Assembly: Growth and Breakage of Synthetic DNA Nano-Structures

#### **Permalink**

<https://escholarship.org/uc/item/526618mr>

#### **Author**

Green, Leopold Noel

#### **Publication Date**

2016

Peer reviewed|Thesis/dissertation

UNIVERSITY OF CALIFORNIA  
RIVERSIDE

Dynamic Self-Assembly: Growth and Breakage of Synthetic DNA  
Nano-Structures

A Dissertation submitted in partial satisfaction  
of the requirements for the degree of

Doctor of Philosophy

in

Bioengineering

by

Leopold Noel Green, Jr.

March 2017

Dissertation Committee:

Professor Elisa Franco, Chairperson  
Professor Sharon Walker  
Professor Ian Wheeldon

Copyright by  
Leopold Noel Green, Jr.  
2017

The Dissertation of Leopold Noel Green, Jr. is approved:

---

---

---

Committee Chairperson

University of California, Riverside

## Acknowledgments

First and foremost, I would like to express my sincere gratitude to my advisor Prof. Elisa Franco (Dept. of Mechanical Engineering) for her continuous support and guidance throughout my Ph.D study. Her patience, motivation, and immense knowledge was more than comforting when joining her lab as a first year student with no research experience in DNA nanotechnology and control theory. Dr. Franco allowed me to explore not only my scientific creativity, but also created an opportunity for me to travel the world and experience science from a global and diverse perspective. As a graduate student of Elisa Franco, I have become a true scientific researcher, and learned the art of presenting and communicating ideas clearly and artistically. Watching Dr. Franco transition from a professional during work hours to a mother every other moment in-between has indirectly instilled in me the ability to compartmentalize and maintain a healthy, yet successful balance of work and family. Most importantly, Dr. Franco has been consistently fair in balancing her course work, research, and mentorship, providing constructive, provide feedback as my experiments went through the many ups and downs over the course of five years. Thank you Dr. Franco for your hard work and commitment to my success as a researcher, scientist, and aspiring professor.

I would like to give special thanks to my committee members, Dr. Sharon Walker and Dr. Ian Wheeldon (Dept. of Chemical and Environmental Engineering). More than a committee member, Dr. Walker always made time, despite her vigorous schedule, to provide helpful tips to help organize and display my research ideas, as well as relieve stress in my daily life. Dr. Walker openly discussed her path to professorship and encouraged me to continue to strive toward my true passion, especially in my moments of doubt.

I am also deeply indebted to Dr. Ian Wheeldon for his willingness to serve on my committee. The progression of my research from the beginning stages to now would not have been made possible without his intellectual contributions. Dr. Wheeldon challenged my early results through insightful comments and encouragement. The difficult questions asked incentivized me to widen my research from various perspectives.

My sincere thanks also goes to Dr. Victor Rodgers (Dept. of Bioengineering), Bro. Dr. Ernest Levister, Dr. Desiré Whitmore, and Mr. Steven Henderson (along with CABE committee) for allocating the time and providing endless resources to assure my success both on and off campus. Dr. Rodgers has been a constant wave of confidence building through his unique teaching style. Whether in the classroom, passing through the hallways of campus, or during community outreach programs, Dr. Rodgers never failed to turn a moment into a teaching opportunity. Your kind, yet strong willed methods are greatly appreciated.

Bro. Dr. Ernest Levister never fell short of going further and beyond to help develop my network with his well established friendships. Not only was Dr. Levister quick to provide endless resources, he was never reserved when indicating my focus was wavering, or where I may be falling short in certain areas. His sometimes cruel, yet honest and old school approach was the consistent push needed for a minority student pursuing a doctorate degree. Dr. Levister helped organize the Counsel of the Advancement of Black Engineers (CABE) in which I have been an active board member and liaison to NSBE undergraduate chapter. Through CABE I have had the wonderful opportunity to work with Dr. Desiré Whitmore and Mr. Steven Henderson. Both Dr. Whitmore and Mr. Henderson have been more than just mentors, but in times of need acted as older siblings. Dr. Whitmore has provided a wealth of knowledge through her personal experiences that assisted in my development and being prepared for various

fellowship application, and future employment opportunities. Needless to say, Mr. Henderson has provided me with many tools of professionalism, along with the resources to make traveling to national conferences affordable.

I thank my fellow lab mates, collaborators and colleagues for the stimulating discussions, and sleepless nights in lab together. All of your insight during lab meetings, oral presentation preparation, and laughter provided during lunch outings were priceless. In particular, I am grateful to Dr. Hari Subramanian for your efforts from the moment you stepped foot into lab. Without your expertise, knowledge, and genuine passion for science and research, my success as a graduate student would not have been. I most greatly honor your odd sleep patterns which allowed me to rest peacefully in the wee hours of the night, as you assisted in imaging coupled nanotubes. I am extremely thankful for future Dr. Vahid Mardanlou for your hard work modeling nanotube reactions and together with future Dr. Christian Cuba for your willingness to assist in troubleshooting MATLAB scripts. Special thanks to Dr. Rizal Hariadi (Arizona State University) for your motivating push to complete my studies, and write our paper. The time and energy placed into teaching the art of figure crafting was magnificent and will be used in future manuscripts. Lastly, thank you Dr. Jongmin Kim for your time and efforts in discussing the progress of my dissertation work. Specifically, thank you for the advice and assistance during the molecular tuning of the oscillator as well as the final fits.

Last but not the least, I would like to thank my family, friends, mentees and brothers of Alpha Phi Alpha Fraternity, Inc. for supporting me spiritually and emotionally throughout conducting experiments and writing my thesis. The completion of my doctoral studies is a true testament to your unwavering love and everlasting motivation to my life.

This work has been supported through the National Science Foundation Graduate Research Fellowship Program (NSF-GRFP) in which I was awarded in 2013. The following research presented here will be submitted for peer review journal publication in the near future.

## **DEDICATION**

To my parents, Leopold and Deana Green;

my sister, future Lexa Green, J.D.;

and my dearest and loving wife, Cecilia Green;

this dissertation is respectfully dedicated. Thank you for endless love and support.

## ABSTRACT OF THE DISSERTATION

Dynamic Self-Assembly: Growth and Breakage of Synthetic DNA Nano-Structures

by

Leopold Noel Green, Jr.

Doctor of Philosophy, Graduate Program in Bioengineering  
University of California, Riverside, March 2017  
Professor Elisa Franco, Chairperson

Biological systems reconfigure their shape in response to external stimuli at the level of single cells, tissues, and organs, for a variety of purposes such as growth, development, and self-repair. Cell shape reconfiguration is accomplished by directing the spatial organization of molecular materials (for example, cytoskeletal proteins) through molecular circuits which sense, process, and transmit information. Embedding a similar architecture in a synthetic material may greatly advance our ability to build responsive materials which can grow, reconfigure, and self-repair. DNA and RNA are programmable biological polymers which have been used to rationally build sensors and circuits, and a variety of nanostructures. The integration of nucleic acid circuits and structures promises to yield a new class of complex, reconfigurable materials. We aim at directing assembly and disassembly of DNA nanostructures with dynamic DNA inputs and circuits, mimicking the organization of dynamic cellular materials.

We focus on DNA nanotubes, and design pathways to control growth and breakage of tubes assembled from double crossover tiles. Our tiles include a toehold domain enabling strand invasion at the sticky ends of tiles. Invasion rapidly weakens the self-assembled structure, causing the nanotubes to collapse into smaller fragments.

Removal of DNA species used for invasion, through second layer of strand displacement (denoted as anti-invasion), allows the nanotubes to reassemble isothermally. Our design thus makes it possible to control growth reversibly. We demonstrate this directed assembly process through a variety of experimental assays including optical microscopy and time lapse movies, atomic force microscopy, and gel electrophoresis. We also characterize the influence of experimental design parameters such as toehold orientation (inside vs. outside of tube) and length, buffer conditions, and temperature, showing the overall tunability of breakage and reassembly dynamics.

Here, we bridge dynamic and structural DNA nanotechnology and demonstrate the programmable, dynamic control of self-assembly of DNA nanotubes, a well known class of micron-sized DNA nanostructures. Nanotube assembly and disassembly is controlled with nucleic acid inputs and with transcriptional systems including an autonomous molecular oscillator.

# Contents

<b>List of Figures</b>	<b>xii</b>
<b>List of Tables</b>	<b>xiii</b>
<b>1 Introduction</b>	<b>1</b>
<b>2 Objectives</b>	<b>5</b>
<b>3 Designing Tiles for Dynamic Self-Assembly</b>	<b>7</b>
3.1 Introduction . . . . .	8
3.1.1 DNA Self Assembly . . . . .	8
3.1.2 DAE-E Tiles and nanotubes . . . . .	14
3.1.3 Comparison of tiles assembling into nanotubes with external or internal toehold . . . . .	15
3.2 Methods and Materials . . . . .	16
3.2.1 Sample preparation . . . . .	16
3.2.2 Fluorescence microscopy . . . . .	17
3.2.3 Fluorescence microscopy data processing . . . . .	17
3.2.4 Atomic Force Microscopy . . . . .	18
3.2.5 Gel electrophoresis . . . . .	18
3.2.6 DNA Sequences . . . . .	19
3.3 Results and Discussion . . . . .	20
3.3.1 Nanotube growth post anneal . . . . .	20
3.3.2 Analysis of Internal vs. External Toehold Positioning . . . . .	24
3.4 Concluding Remarks . . . . .	26
<b>4 Characterization of Triggered Assembly and Disassembly</b>	<b>28</b>
4.1 Introduction . . . . .	29
4.1.1 Toehold-Mediated Branch Migration . . . . .	29
4.2 Reaction Schemes . . . . .	32
4.2.1 Invasion reaction . . . . .	32
4.2.2 Anti-invasion reaction . . . . .	32
4.3 Results and Discussion . . . . .	34
4.3.1 Invasion and anti-invasion reactions: Example images . . . . .	34
4.3.2 Length distribution of nanotubes after invasion . . . . .	35
4.3.3 Nanotube invasion as a function of toehold length . . . . .	40
4.3.4 Length distribution of nanotubes after invasion and anti-invasion	43

4.3.5	Cycles of invasion and anti-invasion in nanotubes with 100% toe-held tiles . . . . .	50
4.3.6	MgCl <sub>2</sub> Concentration Optimization . . . . .	51
4.3.7	Invasion and anti-invasion reactions on nanotubes with internal toehold . . . . .	54
4.4	Concluding Remarks . . . . .	55
<b>5</b>	<b>Designing DNA Tiles Suitable for Transcriptional Buffer Conditions</b>	<b>56</b>
5.1	Introduction . . . . .	57
5.2	Methods and Materials . . . . .	58
5.2.1	Transcription . . . . .	58
5.2.2	DNA Sequences . . . . .	58
5.3	Reaction Schemes . . . . .	60
5.3.1	7 and 8 base long sticky-end of: Invasion, Anti-Invasion, and side reactions . . . . .	60
5.3.2	Reactions for transcriptional control of nanotube breakage and reassembly . . . . .	62
5.4	Results and Discussion . . . . .	64
5.4.1	Invasion and anti-invasion of nanotubes with 8 and 7 base sticky ends . . . . .	64
5.4.2	Nanotube disassembly and reassembly via a cotranscribed RNA invader and RNase H . . . . .	73
5.5	Concluding Remarks . . . . .	76
<b>6</b>	<b>Autonomous Control of DNA Tile Self-Assembly with Synthetic Oscillator</b>	<b>77</b>
6.1	Introduction . . . . .	78
6.1.1	Overview of Logic Circuits and Dynamic Circuits . . . . .	78
6.2	Methods and Materials . . . . .	79
6.2.1	Bulk fluorimetry . . . . .	79
6.2.2	Bulk fluorimetry data processing . . . . .	80
6.2.3	Transcription . . . . .	81
6.2.4	DNA Sequences . . . . .	82
6.3	Reaction Schemes . . . . .	84
6.3.1	Reactions designed to direct tube breakage and reassembly using an autonomous molecular oscillator . . . . .	84
6.4	Results and Discussion . . . . .	88
6.4.1	Directing nanotube disassembly and reassembly using a synthetic transcriptional oscillator . . . . .	88
6.5	Concluding Remarks . . . . .	104
<b>7</b>	<b>Conclusion</b>	<b>106</b>
7.1	Lessons Learned . . . . .	108
7.2	Outlook . . . . .	108

# List of Figures

3.1	Theory of Mathematical Tiling (Figure adapted from Winfree 1998 [53])	8
3.2	Scheme of folded scaffold (black) to form arbitrary shape held together by staple strands (colored) (Figure adapted from Rothemund 2006 [42])	9
3.3	Origami Structures (Figure adapted from Rothemund 2006 [42]) . . . . .	9
3.4	Super Origami Designs and Structures (Figure adapted from Zhao 2011 [69]) . . . . .	10
3.5	DAO structure (left) and DAE structure (right) (Figure adapted from Fu 1993 [17]) . . . . .	11
3.6	Schematic of DAO-O Tile Design and Tube Formation . . . . .	12
3.7	Schematic of DAE-E Tile Design and Tube Formation . . . . .	13
3.8	<b>Chemical reactions controlling activity of monomers can be used to direct self-assembly</b> A: We consider DNA double crossover tiles [17, 43] formed by five unique DNA strands. Tiles assemble into nanotubes via programmed interactions of their sticky ends (domains marked as a, b, a' and b'). Tiles were modified to include a single stranded overhang, or toehold, illustrated as the black domain on the 5' end of the yellow strand. B: Schematic illustration of a tile. C: Hybridization of sticky ends results in formation of hollow nanotubes with average 13.5 nm diameter; toeholds placed on the 5' end of the yellow strand are expected to be on the external surface of the nanotube (conversely, toeholds on the 3' end of the yellow strand would be internal to the nanotube). . . . .	14
3.9	<b>5 base sticky-end Tile variants with external toehold</b> A-D: Strand interactions in tiles with 5 base-long sticky ends. A: No toehold. B: 3 base toehold. C: 5 base toehold. D: 7 base toehold. . . . .	14
3.10	<b>Tiles resulting in nanotubes with external and internal toehold</b> These tiles have 5 base-long sticky ends. A - Left: To obtain a nanotube with toeholds facing the external surface of the nanotube, we located the toehold on the 5' end of strand S2. Right: Nanotubes with internal toehold can be obtained by placing the toehold on the 3' end of strand S2. B: Rendering of the tiles obtained with Nanoengineer []. C: Nanotubes with external toehold can be invaded at all points on the lattice where the toehold is exposed; in contrast, nanotubes with internal toeholds can be invaded primarily at the ends. Time-lapse movies supporting this expectation are available online. . . . .	15

3.11	<b>Growth of nanotubes in the absence of toehold domain</b> Nanotube length was measured over 30 hours (after annealing) from fluorescence microscopy images. Left: Violin plots of each experiment repeat. Right: mean and standard deviation of the mean of length over the three experiments to the left. . . . .	21
3.12	<b>Growth of nanotubes annealed from tile sample where 50% of tiles include a toehold domain</b> Nanotube length was measured over 30 hours (after annealing) from fluorescence microscopy images. Left: Violin plots of each experiment repeat. Right: mean and standard deviation of the mean of length over the three experiments to the left. . . . .	22
3.13	<b>Growth of nanotubes annealed from tile sample where 100% of tiles include a toehold domain</b> Nanotube length was measured over 30 hours (after annealing) from fluorescence microscopy images. Left: Violin plots of each experiment repeat. Right: mean and standard deviation of the mean of length over the three experiments to the left. . . . .	23
3.14	<b>Growth of nanotubes is not influenced by the presence of external toehold</b> We compare the mean length data from Fig. 3.11, 3.12, and 3.13; the nearly overlapping means indicate that the presence of a 7 base external toehold does not affect nanotube growth. . . . .	24
3.15	A1 and A2: Nanotubes (5b SE) with internal toeholds after incubation with Streptavidin-Truncated invader complex. A1 shows grown Cy5-labeled nanotubes. A2 is an image of the same sample with a Cy3 filter, which indicates virtually no streptavidin is bound to the nanotubes, following our expectation (toeholds are internal to the nanotube surface, therefore not available for streptavidin-truncated invader complex binding). B1 and B2: Nanotubes (5b SE) with external toehold after incubation with streptavidin-Truncated invader complex. B1 shows the Cy5 channel, and B2 shows the Cy3 channel. Both images show patches of fluorescence, which indicate that a) the streptavidin-bridged truncated invader complex binds to the external toeholds, b) due to tetravalent nature of streptavidin, it binds to multiple nanotubes and promotes aggregation.	26
4.1	3 Stages of Toehold-Mediated Branch Migration . . . . .	30
4.2	Schematic of Invasion Process . . . . .	31
4.3	Schematic of Anti Invasion Process . . . . .	31
4.4	<b>Illustration of invasion reaction</b> Invasion in 5 base-long sticky end tiles.	32
4.5	<b>Illustration of anti-invasion reaction</b> A: Anti-invasion in 5 base-long sticky end tiles. . . . .	33
4.6	<b>Anti-invader can bind to strand S4</b> A: Interaction in 5 base-long sticky end tiles is limited to 5 bases, and is therefore likely unstable. . .	33
4.7	Tubes with 50% tiles containing toehold (A:C) Fluorescent Microscopy and (D:F) Atomic Force Microscopy. Initial tubes (A,D). Invader reduces tube length significantly, yet tubes are still visible in both microscopy and AFM images (Figure B,E). The addition of anti-invader to tube solution allows nanotube regrowth (C,F). . . . .	34

4.8	Visualization of invasion and anti-invasion rxn of tubes with 100% tiles containing toehold (A:C) Fluorescent Microscopy and (D:F) Atomic Force Microscopy. Figures A and D illustrate tubes prior to invasion. After invasion reaction at room temperature, 10 min Figure B, and 20 min Figure E, tubes completely break apart. The presence of anti-invader promotes the re-assembly of tubes from monomer tiles or chunks, Figures C and F. . . . .	35
4.9	<b>In the absence of toeholds nanotubes do not break in the presence of invader strand.</b> We measure the nanotube length for 30 hours after addition of invader; prior to the beginning of the experiments, nanotubes were incubated for 30 hours, reaching a mean length of about 6 $\mu\text{m}$ [13]. The red triangle marks when invader is added to the sample. The results indicate that the invader does not significantly decrease nanotube length because the strand invasion reaction (Fig. 4.4) cannot be initiated in the absence of a toehold. However, the presence of invader appears to suppress further growth. Left: Violin plots of each experiment repeat. Right: mean and standard deviation of the mean of length over the three experiments to the left. . . . .	37
4.10	<b>Invasion reaction of nanotubes where 50% of tiles include a toehold domain.</b> After addition of invader (marked by the red triangle) the mean nanotube length rapidly decreases to half the initial length, and remains constant for the following 30 hours. Left: Violin plots of each experiment repeat. Right: mean and standard deviation of the mean of nanotube length over the three experiments to the left. . . . .	38
4.11	<b>Invasion reaction of nanotubes where 100% of tiles include a toehold domain.</b> After addition of invader (marked by the red triangle) nanotubes rapidly disassemble and no nanotubes can be seen in fluorescence microscopy images; nanotubes do not reform in the following 30 hours. Right: mean and standard deviation of the mean of nanotube length over the three experiments to the left. . . . .	39
4.12	<b>Invasion causes a decrease in mean nanotube length that depends on the concentration of toeholded tiles</b> This plot compares the mean length data from Fig. 4.9, 4.10, and 4.11. . . . .	40
4.13	<b>Invasion reaction on nanotubes with 100% tiles including a 3 base-long external toehold.</b> A 3 base toehold is not sufficient to initiate weak breakage of nanotubes, as indicated by the slight decrease in mean length after addition of invader (marked by the red triangle). On average, nanotubes subsequently regrow reaching mean length higher than their initial length. Left: Violin plots of separate experiments. Right: Mean and standard deviation of the mean for the length distributions measured in the experiments to the left. . . . .	41
4.14	<b>Invasion reaction on nanotubes with 100% tiles including a 5 base-long external toehold.</b> A 5 base toehold is sufficient to initiate weak breakage of nanotubes. Addition of invader (marked by the red triangle) results in roughly a 30% decrease in the mean nanotube length; however, nanotubes subsequently regrow reaching mean length comparable to the initial mean length. Left: Violin plots of separate experiments. Right: Mean and standard deviation of the mean for the length distributions measured in the experiments to the left. . . . .	42

4.15	<b>A 7 base-long toehold is necessary to fully break nanotubes and suppress growth.</b> We compare the mean length measured in invasion experiments using nanotubes grown from 3 base, 5 base and 7 base-long toehold tiles (100% tiles including an external toehold). Addition of invader is marked by the red triangle. A 7 base toehold is necessary to fully break nanotubes and suppress their regrowth. . . . .	43
4.16	<b>The mean length of nanotubes without toehold is not affected by the presence of invader and anti-invader.</b> Red and blue triangles mark respectively the addition of invader and anti-invader. The mean length of nanotubes does not decrease after addition of invader; addition of anti-invader does not promote further growth, suggesting that nanotubes have reached an equilibrium length distribution. Left: violin plots of each experiment. Right: mean and standard deviation of the mean for the experiments to the left. . . . .	45
4.17	<b>Invasion and anti-invasion of nanotubes with 50% toehold tiles</b> Consistently with the experimental results on invasion (Fig. 4.10), nanotube mean length decreases by about 50% after addition of invader (marked by the red triangle). Addition of anti-invader (marked by blue triangle) promotes regrowth to a mean length that is comparable to the initial mean length. Left: violin plots of each experiment. Right: mean and standard deviation of the mean for the experiments to the left. . . .	46
4.18	<b>Invasion and anti-invasion of nanotubes with 100% toehold tiles.</b> Addition of invader, marked by the red triangle, results in rapid disassembly of nanotubes (no nanotubes are visible in fluorescence microscopy images). When anti-invader is added, as marked by the blue triangle, nanotubes start regrowing reaching a mean length comparable to the initial length. Left: violin plots of each experiment. Right: mean and standard deviation of the mean for the experiments to the left. . . .	47
4.19	<b>Comparison of mean nanotube length following invasion and anti-invasion reactions for different percentage of toehold tiles.</b> This plot compares the results shown in Fig. 4.16, 4.17 and 4.17. . . . .	48

4.20	Gel Assays analyzing breakdown products of invasion and anti-invasion of various tile with toehold concentrations (external toehold). Tubes/tiles are labeled with Cy3. DX tile based tubes are too large to run through 0.5% agarose gel. Note dark (high fluorescent) bands at top of lane (A:C) indicates tubes that are not able to enter gel. Tile band (lowest bands in A:C) represents the breakdown products, or individual monomer tiles. Between the two tube and tile bands are polymer smears, or joined tiles not forming tubes. Control lane: tubes annealed with invader to form monomer tiles or breakdown products – Figures A,B = Lane 4, Figure C = Lane 5. A. 0% of tiles contain toehold. The intensity of tile bands in lanes 1:3 has no noticeable change. Tubes with 0% toehold are not shrinking when introduced to invader. B. Tubes with 50% tiles containing toehold. Lane 1, initial tube conditions after anneal, and incubation period has a faint tile band. After adding invader strand to tube solution (Lane 2), the intensity of breakdown products increases significantly. However, there are still tubes present in tube band, indicating that some tubes form shorter breakdown products, as other tubes remain intact. C. 100% of tiles has a toehold domain. Lane 1: Prior to invader, 'relatively' high fluorescent tube band; polymer smear; 'relatively' low fluorescent tile band. After 20 min of invasion rxn (Lane 2), complete tube disassembly is illustrated as both tube band and polymer smear completely disappear, resulting in 'relatively' high tile band. Lane 3 and 4 (Anti-invasion 1 hour and 2 hour incubation respectively), illustrates reappearance of polymer smear, and increase in tube band intensity. . . . .	49
4.21	<b>Repeated addition of invader and anti-invader result in reversible cycles of assembly and disassembly.</b> Left: Violin plots of each experiment. Right: Mean and standard deviation of the mean of the experiments to the left. . . . .	50
4.22	<b>Invasion and anti-invasion reactions in the presence of 24.8 mM MgCl<sub>2</sub></b> The concentration of MgCl <sub>2</sub> in these experiments is twice the concentration used in typical annealing conditions. The mean length of nanotubes after addition of invader (red triangle) decreases to zero (no nanotubes are visible in fluorescence microscopy experiments). Addition of anti-invader (blue triangle) promotes nanotube regrowth as at nominal MgCl <sub>2</sub> concentration. Left: Violin plots of each experiment. Right: Mean and standard deviation of the mean of the experiments to the left. . . . .	52
4.23	<b>Invasion and anti-invasion reactions in the presence of 6.1 mM MgCl<sub>2</sub></b> The concentration of MgCl <sub>2</sub> in these experiments is half the concentration used in typical annealing conditions. The mean length of nanotubes after addition of invader (red triangle) decreases to zero (no nanotubes are visible in fluorescence microscopy experiments). Addition of anti-invader (blue triangle) promotes nanotube regrowth reaching a mean length that exceeds that at nominal MgCl <sub>2</sub> concentration. Left: Violin plots of each experiment. Right: Mean and standard deviation of the mean of the experiments to the left. . . . .	53

4.24	<b>Comparison of mean nanotube length after invasion and anti-invasion at different concentrations of MgCl<sub>2</sub>.</b> This plot compares mean length shown in Fig. 4.22 and 4.23. These results indicate that a concentration of MgCl <sub>2</sub> lower than the nominal concentration (12.4 mM) facilitates nanotube regrowth. . . . .	54
4.25	<b>Invasion and anti-invasion reactions of nanotubes with internal toehold.</b> Left: Violin plots of each experiment. Right: Mean and standard deviation of the mean of the experiments to the left. . . . .	55
5.1	<b>Extended sticky-end tile variants for increased stability in transcriptional conditions</b> A: 7 base sticky-end Tile variants with external toehold. B: 8 base sticky-end Tile variants with external toehold . . . .	57
5.2	<b>Illustration of Invasion reactions of bound tiles</b> A: Interaction in 7 base-long sticky end tiles. B: Interaction in 8 base-long sticky end tiles. . . . .	60
5.3	<b>illustration of anti-invasion reaction resulting in tube formation.</b> A: Interaction in 7 base-long sticky end tiles. B: Interaction in 8 base-long sticky end tiles. . . . .	61
5.4	<b>Anti-invader can bind to strand S4</b> A: Interaction in 7 base-long sticky end tiles. B: Interaction in 8 base-long sticky end tiles. . . . .	62
5.5	<b>Transpirational and Enzymatic control of DNA Nanotubes</b> A: Activation of genelet promoting transcription of RNA invader (genelet ON). B: Deactivation of genelet (genelet OFF) via inhibitor strand displacing bound activator from genelet. C: Schematic of nanotube dynamic. When genelet is ON, RNA invader is produced causing nanotube breakage. In presence of RNase H enzyme, turning genelet OFF results in reformation of nanotubes in solution. . . . .	63
5.6	<b>Enzyme-driven invasion and anti-invasion reactions</b> A: A synthetic gene (Invader Insulator) is used to transcribe the species RNA invader. The gene can be turned off by displacement of the activator strand A1 [23] using an inhibitor strand dI1. (Species A1 and dI1 are the same used in the transcriptional oscillator described in Section 6.3.1, Figs. 6.2 and 6.3). B: Invasion reaction mediated by the RNA invader. C: RNA invader bound to tiles is degraded by RNase H, which results in the release of the sticky end domain. Tiles can therefore reassemble. . . . .	64
5.7	<b>Invasion and anti-invasion of nanotubes assembled from tiles with 7 base-long sticky ends (100% toeholded tiles).</b> Addition of invader (marked by the red triangle) results in rapid disassembly of nanotubes (no nanotubes are visible in fluorescence microscopy images). When anti-invader is added (marked by the blue triangle) nanotubes regrow reaching a mean length which exceeds their initial mean length. In this case, binding of anti-invader to the sticky end of strand S4 seems to not contribute slower growth 4.6. Left: violin plots of each experiment. Right: mean and standard deviation of the mean for the experiments to the left. . . . .	66

5.8	<b>Invasion and anti-invasion of nanotubes assembled from tiles with 8 base-long sticky ends (100% toehold tiles).</b>	Addition of invader (marked by the red triangle) results in rapid disassembly of nanotubes (no nanotubes are visible in fluorescence microscopy images). When anti-invader is added (marked by the blue triangle) nanotubes regrow reaching less than 50% the initial mean length. Limited regrowth may be due to two phenomena: 1) instability of the shortened tile arms, and 2) binding of anti-invader to one of the sticky ends of strand S4, which may form a stable complex in the 8 base-long sticky end tile as noted in Fig. 4.6. Left: violin plots of each experiment. Right: mean and standard deviation of the mean for the experiments to the left. . . . .	67
5.9	<b>Nanotubes assembled from tiles with 7 base sticky ends are not stable when incubated with T7 RNAP</b>	Nanotubes were annealed at 5 $\mu$ M tile concentration, subsequently diluted to a 500 nM tile concentration and incubated in transcription buffer, at 37 $^{\circ}$ C. A) Example image of nanotubes prior to addition of T7 RNA polymerase. B) Example image of nanotubes taken after 30 minutes addition of 10% (v/v) T7 RNA polymerase. Nanotubes annealed at higher tile concentration melt as well in the presence of T7 RNAP. . . . .	68
5.10	<b>Nanotubes annealed from tiles having 8 base sticky ends are stable in the presence of T7 RNA polymerase at high tile concentration.</b>	were annealed at 5 $\mu$ M tile concentration in 1X transcription buffer, and subsequently diluted in transcription mix (1x transcription buffer, 20 mM MgCl <sub>2</sub> , and 20 mM NTPs) including 10% (v/v) T7 RNA polymerase. A1, B1, C1: Example images of nanotubes at 400 nM, 750 nM, and 2 $\mu$ M tile concentration respectively, prior to addition of T7 RNA polymerase. A2: Example image of nanotubes incubated at 400 nM tile concentration in the presence of RNAP for 15 hours. B2: Example image of nanotubes incubated at 750 nM tile concentration in the presence of RNAP for 30 hours. C2: Example image of nanotubes incubated at 2 $\mu$ M tile concentration in the presence of RNAP for 30 hours. . . . .	69
5.11	<b>Nanotubes annealed from tiles having 8 base sticky ends are stable in the presence of T7 RNA polymerase at 750 nM tile concentration.</b>	Nanotubes were incubated at 37 $^{\circ}$ C in transcription mix, in the presence of 10% (v/v) T7 RNAP. Left: Violin plots of length distributions tracked over time. Right: Mean and standard deviation of the mean of the results shown in the left panel. . . . .	70
5.12	<b>Monitoring invasion and anti-invasion reactions using bulk fluorimetry</b>	A1: 8 base SE tiles were labeled with a TAMRA fluorophore on the 5' end of strand 4. A2: Fluorescence is quenched when strand 4 sticky ends form a double stranded complex (assembled tiles). B: Partially blunt-ended 8 base SE tile with truncated strand 2 (tiles cannot assemble). C: Invasion reaction results in disassembly of sticky ends and therefore increase in fluorescence. D: Bulk fluorimetry data showing that invaded tiles exhibit fluorescence nearly identical to that of partially blunt-ended tiles (that are unable to assemble) and to that of tiles annealed with invader strands. Addition of invader to Sample 1 is marked by the dark green triangle (+I), and addition of anti-invader to Sample 1 is marked by the light green triangle (+A). . . . .	71

5.13	<b>Co-transcriptional invasion mediated by RNA</b> Left: violin plots of each experiment. Right: mean and standard deviation of the mean for the experiments to the left. . . . .	74
5.14	<b>Co-transcriptional invasion mediated by RNA, and RNase H-mediated anti-invasion of nanotubes assembled from 8 base-long sticky end tiles.</b> Left: violin plots of each experiment. Right: mean and standard deviation of the mean for the experiments to the left. . . . .	76
6.1	<b>Topology of the oscillator and its biochemical reactions.</b> A: Topology of the synthetic molecular oscillator used in our experiments: two artificial genetic switches (SW12 and SW21) are mutually interconnected through their RNA transcripts (rA1 and rI2) forming a negative feedback loop. B: Reactions occurring in the system. Functionally distinct domains (toeholds, regulatory domains, spacers, promoter and hairpin regions) are colored consistently with strand schematics in Figs. 6.2 and 6.3. Red and black dots on gene T21 and activator A1 are fluorophore-quencher pairs used as reporters on the active/inactive state of the switch. Solid arrows indicate reactions between oligonucleotides; dashed arrows indicate enzymatic reactions (transcription and degradation). Figure is adapted from [23, 16, 52]. . . . .	85
6.2	<b>Switch 12 strands and their domain interactions.</b> This figure shows strands components of SW12 and their interactions, with functional domains in different colors. The mathematical model of the oscillator includes all complexes shown in this figure, including complex sI2·A2 which is the result of interactions between A2 and products of incomplete degradation of RNase H which can reach up to 7 bases [59, 41]. . . . .	86
6.3	<b>Switch 21 strands and their domain interactions.</b> As Fig. 6.2, we show sequences for SW21 with functional domains in different colors. The mathematical model of the oscillator includes all complexes shown in this figure. . . . .	87
6.4	<b>The oscillator was used to direct nanotube assembly and disassembly using an insulator gene.</b> This scheme summarizes the topology of interconnection of the oscillator and the nanotubes. The insulator gene (Fig. 5.6) was designed to be activated and inactivated by strands A1 and dI1 of the oscillator, and its transcript is an RNA invader. Tile reactivation is promoted by RNase H degradation. Strands and reactions for the transcriptional insulator, invasion, and RNase H anti-invasion are shown in Fig. 5.6. . . . .	88
6.5	<b>Oscillator and nanotubes in the absence of insulator gene.</b> Nanotubes at 1 $\mu$ M tile concentration were incubated in the same sample as the oscillator reaction, in the absence of insulator gene (which directs co-transcriptional invasion by producing an RNA invader). In these conditions, the nanotube mean length increases over time exceeding that measured in control experiments (Fig. 5.14). Left: Violin plots of nanotube length distributions. Right: Corresponding normalized oscillator traces (fraction of active T21). . . . .	91
6.6	<b>Mean nanotube length and averaged oscillator behavior.</b> We computed and overlapped the mean and standard deviation of nanotube length and active T21 concentration from Fig. 6.5. . . . .	92

6.7	<b>Nanotube growth directed by the oscillator circuit; 750 nM total tile concentration.</b> Nanotubes annealed from a total concentration of 750 nM tiles were incubated in the same sample as the oscillator reaction in the presence of insulator gene (which directs co-transcriptional invasion by producing an RNA invader). In these low-monomer concentration conditions, nanotubes quickly break after starting the reactions yet regrowth (mediated by RNase H) is suppressed presumably due to the low monomer concentration. Left: Violin plots of nanotube length distributions. Right: Normalized oscillator traces (fraction of active T21).	93
6.8	<b>Mean nanotube length and averaged oscillator behavior; 750 nM total tile concentration.</b> We computed and overlapped the mean and standard deviation of nanotube length and active T21 concentration from Fig. 6.7. . . . .	94
6.9	<b>Nanotube growth directed by the oscillator circuit; 1000 nM total tile concentration.</b> Nanotubes annealed from a total concentration of 1000 nM tiles were incubated in the same sample as the oscillator reaction in the presence of insulator gene (which directs co-transcriptional invasion by producing an RNA invader). Nanotubes break after starting the oscillator reaction by adding enzymes when the insulator is active. When T21 turns off, the insulator activity is also reduced; this means that RNase H degradation dominates over production of invader, and nanotube regrowth is promoted. Left: Violin plots of nanotube length distributions. Right: Corresponding normalized oscillator traces (fraction of active T21). . . . .	95
6.10	<b>Mean nanotube length and averaged oscillator behavior; 1000 nM total tile concentration.</b> We computed and overlapped the mean and standard deviation of nanotube length and active T21 concentration as a function of time from Fig. 6.9. . . . .	96
6.11	<b>Nanotube growth directed by the oscillator circuit; 1500 nM total tile concentration.</b> Nanotubes annealed from a total concentration of 1500 nM tiles were incubated in the same sample as the oscillator reaction in the presence of insulator gene (which directs co-transcriptional invasion by producing an RNA invader). After the oscillator reaction starts (addition of enzymes) the insulator is active, yet breakage is not effective presumably due to the high concentration of tiles, but growth is halted until T21 begins to be turned off. When T21 turns off, the insulator activity is also reduced, and less invader is produced. RNase H degradation dominates over production of invader, and facilitates rapid growth of nanotubes. Left: Violin plots of nanotube length distributions. Right: Corresponding normalized oscillator traces (fraction of active T21).	97
6.12	<b>Mean nanotube length and averaged oscillator behavior; 1500 nM total tile concentration.</b> We computed and overlapped the mean and standard deviation of nanotube length and active T21 concentration as a function of time from Fig. 6.11. . . . .	98

6.13	<b>Nanotube growth directed by the oscillator circuit; 1000 nM tile concentration, 70 nM insulator.</b> Nanotubes annealed from a total concentration of 1000 nM tiles were incubated in the same sample as the oscillator reaction in the presence of 70 nM insulator gene (which directs co-transcriptional invasion by producing an RNA invader). Left: Violin plots of nanotube length distributions. Right: Corresponding normalized oscillator traces (fraction of active T21). . . . .	99
6.14	<b>Nanotube growth directed by the oscillator circuit; 1000 nM tile concentration, 70 nM insulator</b> Triplicate experiments testing the two-oscillation operating point in the presence of insulator at 70 nM, which confirm that as the fraction of SW21 increases (and so does the invader concentration), there is a decrease in mean nanotube length. . .	100
6.15	<b>Nanotube growth directed by the oscillator circuit; 1000 nM tile concentration, 100 nM insulator.</b> Nanotubes annealed from a total concentration of 1000 nM tiles were incubated in the same sample as the oscillator reaction in the presence of 100 nM insulator gene (which directs co-transcriptional invasion by producing an RNA invader). Left: Violin plots of nanotube length distributions. Right: Corresponding normalized oscillator traces (fraction of active T21). . . . .	101
6.16	<b>Nanotube growth directed by the oscillator circuit; 1000 nM tile concentration, 100 nM insulator.</b> Triplicate experiments testing the two-oscillation operating point in the presence of insulator at 100 nM (right), which confirm that as the fraction of SW21 increases (and so does the invader concentration), there is a decrease in mean nanotube length.	102
6.17	<b>Nanotube growth directed by the oscillator circuit; 1000 nM tile concentration, varying concentration of insulator.</b> Nanotubes annealed from a total concentration of 1000 nM tiles were incubated in the same sample as the oscillator reaction in the presence of different amounts of insulator gene (which directs co-transcriptional invasion by producing an RNA invader); insulator concentration from top to bottom row is: 150 nM, 100 nM and 50 nM. Left: Violin plots of nanotube length distributions. Right: Corresponding normalized oscillator traces (fraction of active T21). . . . .	103
6.18	<b>Nanotube growth directed by the oscillator circuit; 1000 nM tile concentration, varying concentration of insulator.</b> We tuned the transcriptional oscillator to exhibit two oscillations. At this operating point, keeping the tile concentration fixed at 1 $\mu$ M tiles, we titrated the concentration of insulator genelet concentrations 50 nM, 100 nM, and 150 nM. Increasing insulator concentration causes oscillator amplitude to decrease (A) and nanotube mean length to decrease on average (B). At 100 nM insulator, the mean length decreases at two distinct points in time when the fraction of SW21 increases. . . . .	104

7.1	<b>Responsive nucleic acid biomaterials could be built by modularly interconnecting sensing, processing, and self-assembling components</b>	Nucleic acids nanotechnology has an expandable toolkit of sensing devices such as aptamers and ribozymes [3], as well as logic and dynamic signal processing devices [62], and nanostructures [66]. These components can be engineered to operate together modularly as a responsive material with programmable behaviors, and could potentially exploit feedback for self-regulation. As a proof of principle, in this paper we demonstrate that it is possible to use complex nucleic acid circuits to direct self-assembly of tubular DNA nanostructures (orange box). . . . .	109
-----	---	---	-----

# List of Tables

3.1	Sequences for tiles with 5-base long sticky ends, invaders, anti-invaders, and all their variants. Bold sequences indicate toehold domains. Expected secondary structures and interactions among tiles, invaders, and anti-invaders are shown in Figs. 3.9, 4.4, 4.5, 4.6 and 3.10. . . . .	19
5.1	Sequences for tiles with 7-base long sticky ends, invaders and anti-invaders. Bold sequences indicate toehold domains. Strand interactions are shown in Fig. 5.1 A, 5.2 A, 5.3 A, and 5.4 A. . . . .	58
5.2	Sequences for tiles with 8-base long sticky ends, invaders and anti-invaders. Bold sequences indicate toehold domains. Strand interactions are shown in Fig. 5.1 B, 5.2 B, 5.3 B, and 5.4 B. . . . .	59
6.1	Sequences for tiles with 8-base long sticky ends, invaders and anti-invaders. Bold sequences indicate toehold domains. Strand interactions are shown in Fig. 5.1 B, 5.2 B, 5.3 B, and 5.4 B. . . . .	82
6.2	DNA sequences for the insulator gene used to couple oscillator and nanotubes, together with its activator and inhibitor (which are the same as for switch 21 of the oscillator). The genelet includes a 3' end hairpin sequence to reduce transcription elongation; thus, the RNA invader includes a hairpin sequence (underlined). Fig. 5.6 shows the interactions among insulator components (activation and inhibition), production of RNA invader, invasion of tiles and RNase H-mediated reactivation of tiles.	82
6.3	DNA sequences for oscillator used to control the growth and decay of DNA nanotubes. Sequences are taken from [23, 16]. Gene sequences include a 3' end hairpin domain to reduce transcription elongation. Target strand interactions are shown in Fig. 6.2 and 6.3; a schematic of the oscillator reactions is shown in Fig. 6.1. . . . .	83

# Chapter 1

## Introduction

Self-assembly is defined as a system of many small components having the ability to automatically interact with themselves to form new, larger, more complex structures [9]. The process of self-assembly is demonstrated in various biological structures [26], including membranes [33], spherical viruses [4], and bacterial flagella [35]. Cells contain cytoskeletal filaments which uses energy as an input to maintain the cell's physical structure by assembling and disassembling microtubules[36]. Nucleic acids are good building materials to mimic such nanoscale dynamics, like cytoskeleton, due to their special programmability characteristics, a consequence of Watson-Crick base-pair interactions [46]. In addition, DNA is a biological material that can be interfaced with a variety of biological and non-biological ligands [14]. Therefore, in developing synthetic dynamic nanomaterials, we will use nucleic acids as the building blocks of our structures. Specifying complementary domains, and then finding sequence realizations through available software packages, we can design interactions among strands [11, 61].

Various nucleic-acid-based nano systems built so far can be roughly classified as either static structures [42, 53, 43, 20] or dynamic nucleic acid circuits [58]. The aim of structural DNA nanotechnology is building robust structures and achieving high levels of control in spatial arrangement of different species. Dynamic DNA nanotechnology uses programmability of DNA to modify DNA structures. Various DNA based nanomachines have been built by combining programmability and structural control [60, 55, 49].

In designing three-dimensional structures, it is important to first construct the individual monomers based on understood molecular interactions, and next to arrange these monomers into building blocks to form larger, more complex structures [53]. Three-dimensional DNA nano-structures have been assembled using multiple short DNA strands ranging from 20 to 60 bases, annealing to form individual monomers known as tiles (Figures 3.6 A. & 3.7 A.). Tiles designed to have sticky ends form DNA lattices,

which in turn generate tubes up to  $5\mu\text{m}$  long [43] (Figures 3.6 B. & 3.7 B).

Along with nucleic acid nano-structures, dynamic circuits, also comprised of nucleic acids, are widely available, and have the ability of operating in heterogeneous solutions. Using only DNA, we can construct large logic circuits and neural networks. Using DNA, RNA, and proteins, we can also build non- equilibrium dynamical systems, such as oscillators [62, 23]. However, due to the high complexity of the content in the cellular matrix, introducing synthetic logic circuits *in vivo* presents many problems [50]. Current *in vitro* systems promotes efficient operations of nucleic-acid-based circuits due to known components and parameters [24]. The next step is to design a molecular system that has flexibility to its surrounding environment, which will allow for the molecular circuit to perform as designed. Developing robust systems is vital in coupling DNA-based nano structures, and molecular circuits.

Little work has been done on the coupling of DNA based nano structures and more complex logic/dynamic circuits. Many similar concepts (branch migration, tile hybridization, etc.) are shared by both models; therefore, we will work to fulfill this gap by bridging the two, using circuits to apply dynamics to DNA based nano structures. We have chosen to use three-dimensional structures (tubes) rather than two-dimensional structures (DNA origami) in applying dynamics due to their difference in structural composition. DNA origami while very versatile in making different structures, needs a long single stranded DNA scaffold to tie together the entire structure. So, dynamically reprogramming DNA origami to give different structures will be very difficult due its restrictive design needs.

This research combines two emerging technologies: nucleic acid nano-structures and nucleic acid circuits. These tools will be used to build a new class of active biological materials, and provide insight on natural biomechanical systems. Nucleic acid based

materials are promising vehicles for drug delivery (presenting lower toxicity than carbon nanotubes, nano-particles, viral capsids, etc) [25]. We will devise methods to interface nano-structures and dynamic circuits. Our results will provide an understanding in natural biomechanical reconfigurable systems, such as cytoskeletal filaments and it will be a step toward a generation of smart, dynamic nano-materials.

## Chapter 2

# Objectives

My project aims at integrating experiments and mathematical modeling to build nanostructures in response to signals that are outputs of dynamic circuits. The optimal operational conditions of our designed nano-structures will be studied. A detailed analysis for the most favorable tube composition and buffer condition will be provided. The underlying goal of this thesis is to expand the current understanding of dynamic systems for future applications of reconfigurable synthetic networks.

Assembly of DNA nanotubes has been well characterized in the past [43]. The first objective of this thesis is to design and test programmable growth and breakage of DNA nanotubes. Such control over programability will allow us to couple this structural change to complex nucleic acid circuits such as synthetic oscillators in future. Using DNA double-crossover tiles [17], I will characterize, through an assortment of assays, the interactions of free tiles and tubes in solution, known as end-to-end joining, along with the stability and dynamics of the tubes when exposed to stressful environments. Using both fluorescent microscopy and Atomic Force Microscopy (AFM), I will analyze the nanotube's structure and how the structure changes under various compositions,

and when exposed to various environmental conditions.

The second objective is to use a molecular oscillator to dynamically drive the assembly and disassembly of the tubes. Using Watson-Crick base pair interactions, we can design a network composed of DNA and RNA that can work as a molecular clock [16]. Designing a robust oscillator is important. I will optimize the oscillatory conditions, such that the presence of tube and other species in solution will not alter the dynamics of the system.

Our experimental goal is to control nanotubes growth and decay with an invading strand, whose concentration in solution will be periodically modulated by the oscillator.

## Chapter 3

# Designing Tiles for Dynamic Self-Assembly

## 3.1 Introduction

### 3.1.1 DNA Self Assembly

#### Origami and Other Assembly Methods

A growing number of design methods in structural DNA nanotechnology, such as DNA tiles [17, 54, 43], DNA origami [42, 10], DNA bricks [22], wireframe structures [67, 2], and crystals [70] allow the construction of molecular objects with controlled nanoscale features, and size ranging from few nanometers to hundreds of microns. Initially, three-dimensional structures of cubes [5] and truncated octahedrons [68] were created using double helical edges, designed by interlinking single strands of DNA. Later, the theory of mathematical tiling, joining tiles together to form a structure where only matching edges (same color) are allowed to interact with each other, was used as the underlying concept of forming two-dimensional DNA crystals (Figure 3.1 [53]).

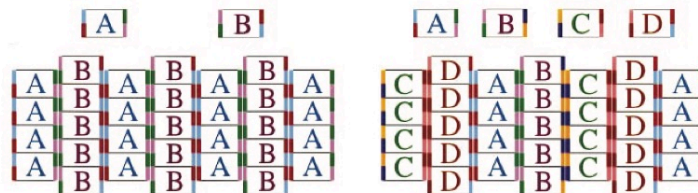


Figure 3.1: Theory of Mathematical Tiling (Figure adapted from Winfree 1998 [53])

Using single strands of DNA, tiles were constructed by designing thermodynamically favored interaction amongst the base pairs between complementary strands. Double crossover tiles were formed, which had the ability to link with other free tiles to form 2-D lattices of either 2-unit or 4-unit tiles (similar to the model illustrated in Figure 3.1). Such designs resulted in striped crystals lattices.

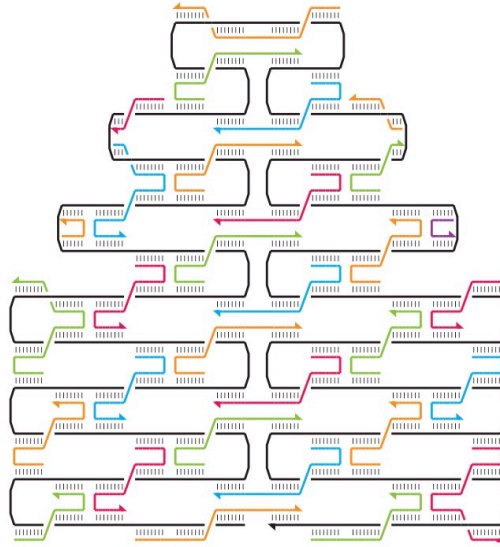


Figure 3.2: Scheme of folded scaffold (black) to form arbitrary shape held together by staple strands (colored) (Figure adapted from Rothemund 2006 [42])

Rothemund *et al* used Watson-Crick base pairing to create more complex nanostructures by folding long single stranded DNA into desired 2-D shapes and structures, known as a scaffold (shown in Figure 3.2[42]). These scaffolds were held in place by using hundreds of short oligonucleotides or staple strands. The resulting DNA structures shown in Figure 3.3 are known as DNA origami.

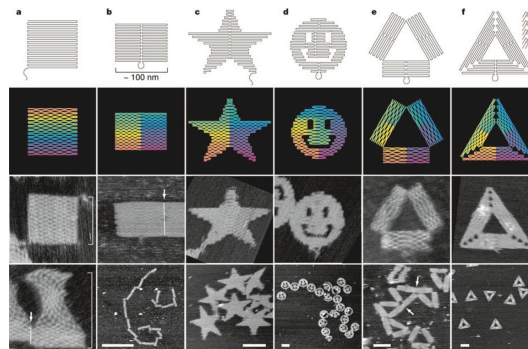


Figure 3.3: Origami Structures (Figure adapted from Rothemund 2006 [42])

Using long single stranded DNA and smaller staple strands, complex structures

can be formed. To change the structure of the origami, many domains of both the scaffold and staple strands must be altered. Zhao *et al.* described a system that could make this possible, known as super origami [69]. This method combines smaller DNA origami structures by bridging free origami structures to pre folded single stranded DNA scaffolds (Figure 3.4). Liu *et al* developed a method of extending DNA based origami in two dimensions without altering the structure of the scaffold[31]. Using monomers such as tiles, as described in Section 3.1.1, allows for predicted changing of size of the assembled structures.

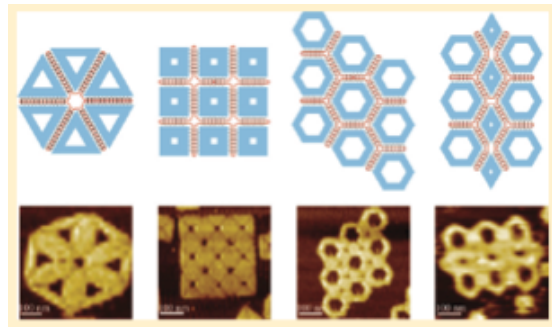


Figure 3.4: Super Origami Designs and Structures (Figure adapted from Zhao 2011 [69])

## DNA Tile Systems

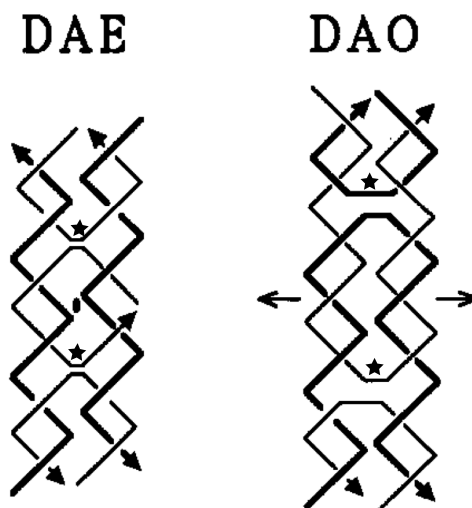


Figure 3.5: DAO structure (left) and DAE structure (right) (Figure adapted from Fu 1993 [17])

The development of highly stable double crossover DNA structures in the mid-nineties led to rapid advances in structural DNA nanotechnology. The Double-crossover (number of crossovers, indicated by stars), Anti-parallel (orientation of strands), Odd (half-turn count between intramolecular crossovers, between stars), Odd (half-turn count between intermolecular crossovers) DAO-O, and the Double-crossover (indicated by stars), Anti-parallel, Even, Even DAE-E structures are shown in Figure 3.5 [17]. Figures 3.6 (DAO-O) & 3.7 (DAE-E) illustrate structure of tiles (A.), the formation of intermediate stage sheets (B.), resulting in the formation of tubes (C.). The factors governing tile formation are the number of crossovers present intramolecularly, the orientation of strands through the crossover, the number of half-turns between intramolecular crossovers, and the number of half-turns between intermolecular crossover.

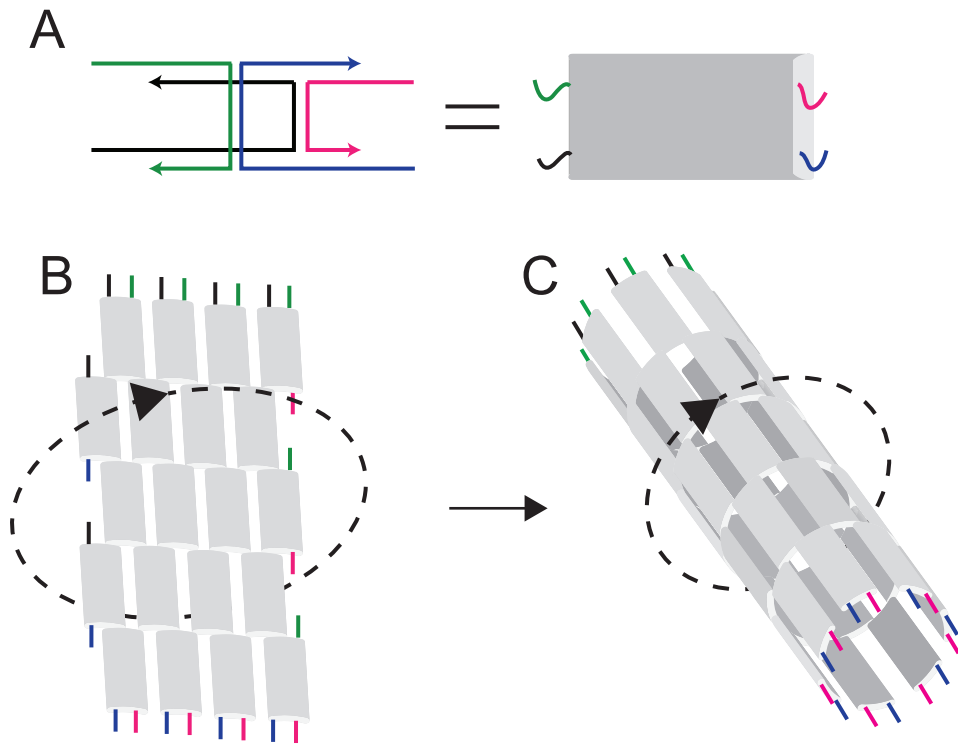


Figure 3.6: Schematic of DAO-O Tile Design and Tube Formation

The Double-crossover (number of crossovers shown by the two vertical lines in Figure 3.6 A, structure (DAO-O) [17, 43], is a non-symmetrical tile containing four single strands of DNA Figure 3.6 A [43]. The hanging ends (represented by the green, black, magenta, and blue free strands in the right illustration of Figure 3.6 A) are known as sticky ends. The sticky ends are designed to have complementary base pairing, allowing for tile interactions to occur (blue hybridizing with green, magenta hybridizing with black). Thermodynamically, tiles are aligned to form sheets. Due to the helical twist to the B-form DNA, and interacting backbones at the crossover junctions, when two tiles join, curvature occurs, eventually forming tubes (Figure 3.6 C) [43].

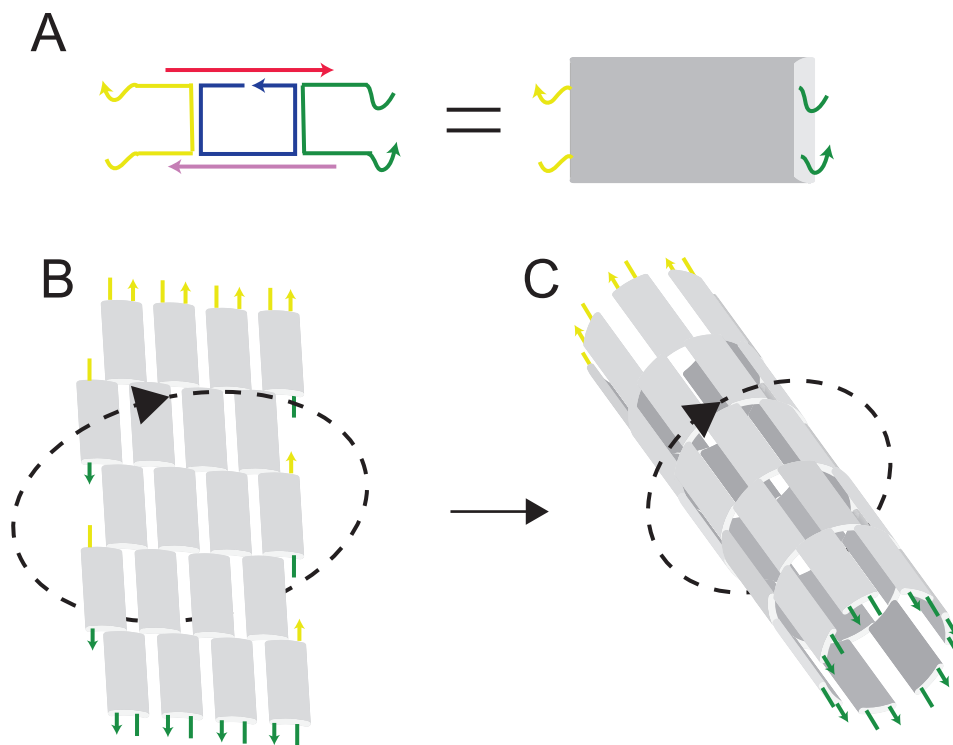


Figure 3.7: Schematic of DAE-E Tile Design and Tube Formation

Similarly to DAO-O tiles, DAE-E tiles also contain double crossover locations. However, the intramolecular and intermolecular half-turn count are both even. The more symmetrical structure of DAE-E tiles is due to the 5-strand design, where the central blue strand acts as the core. The interactions between two tiles are shown in Figure 3.7 B, at green and yellow sticky ends, forming curved sheets also seen in DAO-O design. The  $150^\circ$  angle between the planes of two interacting tiles results in a closure of tubes between 4 and 9 tiles [43].

In both DAO-O and DAE-E tiles, a single DNA strand is covalently bound with a fluorescent label illustrated as an orange circle. In our studies, DAE-E tiles and CY3 (or Alexa-488) is our label of choice. The loose "overhang" strand denoted in our illustration of tile designs represent a toehold domain. This toehold sequence of various

nucleotide lengths in out DAE-E tile will be the access point for implimenting dynamics to our system through toehold-mediated branch migration.

### 3.1.2 DAE-E Tiles and nanotubes

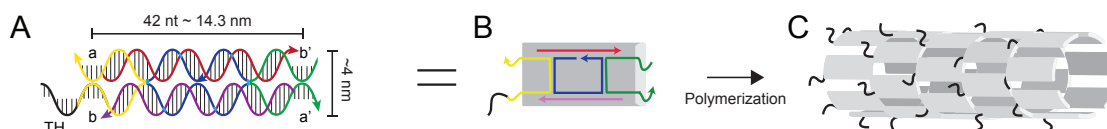


Figure 3.8: **Chemical reactions controlling activity of monomers can be used to direct self-assembly** A: We consider DNA double crossover tiles [17, 43] formed by five unique DNA strands. Tiles assemble into nanotubes via programmed interactions of their sticky ends (domains marked as a, b, a' and b'). Tiles were modified to include a single stranded overhang, or toehold, illustrated as the black domain on the 5' end of the yellow strand. B: Schematic illustration of a tile. C: Hybridization of sticky ends results in formation of hollow nanotubes with average 13.5 nm diameter; toeholds placed on the 5' end of the yellow strand are expected to be on the external surface of the nanotube (conversely, toeholds on the 3' end of the yellow strand would be internal to the nanotube).

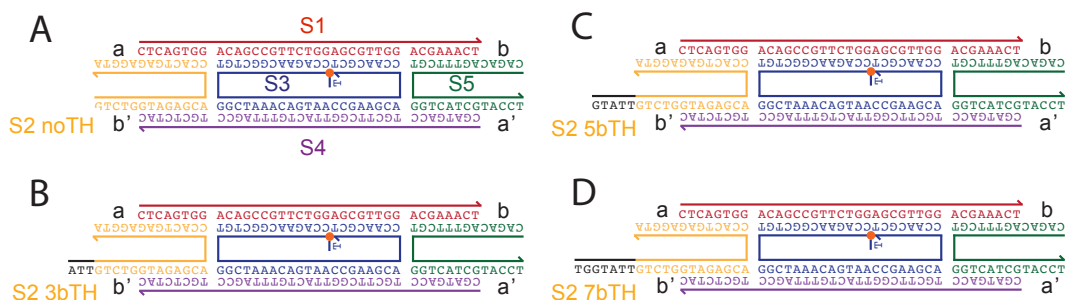


Figure 3.9: **5 base sticky-end Tile variants with external toehold** A-D: Strand interactions in tiles with 5 base-long sticky ends. A: No toehold. B: 3 base toehold. C: 5 base toehold. D: 7 base toehold.



## 3.2 Methods and Materials

### 3.2.1 Sample preparation

Lyophilized DNA oligonucleotides were purchased from Integrated DNA Technologies (Coralville, IA), resuspended in water, quantitated by UV absorbance at 260 nm using a Thermo Scientific Nanodrop 2000c Spectrophotometer, and stored at -20°C. All samples were stored or mixed using DNA Lo-bind tubes (# 022431021).

Nanotubes were annealed at either 1 or 5  $\mu\text{M}$  tile concentration by mixing each tile strand at 1 or 5  $\mu\text{M}$  (final concentration), in either of the following buffer mixes: 1) Tris-Acetate-EDTA (TAE) and 12.4mM  $\text{MgCl}_2$ , or 2) 1X transcription buffer (New England Biolabs, #B9012S). Nanopure water was added to achieve the appropriate concentration of components. Nanotubes were annealed using an Eppendorf Mastercycler PCR machine by heating the sample to 90°C, and cooling it to 25°C over a 6 hour period.

The position of the toehold in nanotubes was characterized by binding of streptavidin to the toeholds. Streptavidin-cy3 was purchased from Biolegend (Cat# 405215). A biotinylated strand (Truncated Invader 5'T, Table 3.1) was used to bridge streptavidin to the 5 base sticky end nanotubes.

Genelets for transcriptional control of nanotube assembly were individually annealed in 1x transcription buffer (New England Biolabs, #B9012S) using an Eppendorf Mastercycler PCR machine by heating the sample to 90°C, and cooling it to 25°C over a 1.5 hour period.

### 3.2.2 Fluorescence microscopy

Nanotube samples were imaged using an inverted microscope (Nikon Eclipse TI-E) with 60X/1.40 NA oil immersion objectives. Samples containing nanotubes were imaged at 50 nM tile concentration in corresponding experimental buffer conditions (either 1x TAE and 12.4mM MgCl<sub>2</sub>, or 1x transcription buffer). Samples were placed on Fischerbrand microscope cover glass (# 12-545E No. 1, thickness=0.13 to 0.17mm; size: 50 x 22mm); VWR Micro Slides (Plain, Selected, Pre-cleaned, 25 x 75 mm, 1.0mm thick) were placed gently on the cover glass. Nanotubes labeled with Cy3 fluorescent molecule were imaged using Cy3 filter cube (Semrock Brightline - Cy3-404C-NTE-ZERO). Exposure time was set to 90ms.

### 3.2.3 Fluorescence microscopy data processing

Fluorescence microscopy images were processed using ImageJ plugin Skeletonize to collect nanotube length distributions. Branching or looping nanotubes were eliminated from the length dataset using an in-house MATLAB script. Pixels were converted to  $\mu\text{m}$  using conversion factor 1pixel = 0.11 $\mu\text{m}$ . Due to camera limitations, tubes lengths less than 0.33 $\mu\text{m}$  were also eliminated from tube length distributions.

Nanotube length distributions measured in fluorescence microscopy experiments are shown as violin plots. These plots were prepared using `distributionPlot`, a MATLAB File Exchange script; in each violin plot, length data are plotted as a histogram normalized individually to have a maximum width of 0.8.

### 3.2.4 Atomic Force Microscopy

AFM images were obtained in tapping mode with a Digital Instruments Multimode AFM, equipped with a Nanoscope III controller. Sharp Nitride Lever (SNL) tips from Bruker with a nominal spring constant of 0.24 N/m were used for imaging, with a drive frequency of 9-10 kHz. Samples were imaged using 1X TAE and 12.5 mM MgCl<sub>2</sub> buffer.

### 3.2.5 Gel electrophoresis

A 0.5% high-melt agarose gel (made using Bio-Rad Certified Megabase Agarose, #1613108) was prepared in 1x TBE and 12.4 mM MgCl<sub>2</sub> by heating 0.5 g of Agarose in 100 mL of the buffer. Once the agarose was fully dissolved, the mixture was allowed to cool and before the mixture solidified, it was poured into the gel cast (Owl Easycast B1 gel system, 9 x 11 cm -Thermo Scientific). DNA nanotubes, labeled with Cy3, at 1  $\mu$ M tile concentration, and 2  $\mu$ l total volume were loaded into the wells of the agarose gel. The samples were loaded onto the gel with Bromophenol blue as a tracking dye. The gel wells were sealed using thin films of solid agarose affixed on top of the wells using molten agarose, to reduce the loss of nanotubes that stay in the wells till the end of the run. The gel was run at room temperature using an Owl Easycast B1 gel system (9 x 11 cm -Thermo Scientific) at 60 V for 3.5 hours. Gel images were taken using a BioRad ChemiDoc MP gel imaging system with a Cy3 filter.

### 3.2.6 DNA Sequences

Tile, invader, and anti-invader sequences:

<i>Name</i>	<i>Tile with 5-base sticky ends</i>
S1	5'- CTC AGT GGA CAG CCG TTC TGG AGC GTT GGA CGA AAC T
S2 7bTH	5'- <b>TGG TAT TGT</b> CTG GTA GAG CAC CAC TGA GAG GTA
S2 5bTH	5'- <b>GTA TTG</b> TCT GGT AGA GCA CCA CTG AGA GGT A
S2 3bTH	5'- <b>ATT</b> GTC TGG TAG AGC ACC ACT GAG AGG TA
S2 NoTH	5'-GTC TGG TAG GCA CCA CTG AGA GGT A
S2 3'-5bTH	5'-GTC TGG TAG AGC ACC ACT GAG AGG TAT <b>GGT</b> <b>ATT</b>
S3 Cy3	5'-T Cy3/CCA GAA CGG CTG TGG CTA AAC AGT AAC CGA AGC ACC AAC GCT
S3 Cy5	5'-T Cy5/CCA GAA CGG CTG TGG CTA AAC AGT AAC CGA AGC ACC AAC GCT
S4	5'- CAG ACA GTT TCG TGG TCA TCG TAC CT
S5	5'-CGA TGA CCT GCT TCG GTT ACT GTT TAG CCT GCT CTA C
Invader 7bTH	5'- ACC AGA CAA TAC CAA TCC GC
Truncated Invader 7bTH	5- AATACCATTT/3Bio/
Anti-Invader 7bTH	5'- GCG GAT TGG TAT TGT CTG GT
Invader 3'-7bTH	5'- GTC CGC AAT ACC ATA CCT CT
Anti-Invader 3'-7bTH	5'- AGA GGT ATG GTA TTG CGG AC

Table 3.1: Sequences for tiles with 5-base long sticky ends, invaders, anti-invaders, and all their variants. Bold sequences indicate toehold domains. Expected secondary structures and interactions among tiles, invaders, and anti-invaders are shown in Figs. 3.9, 4.4, 4.5, 4.6 and 3.10.

## 3.3 Results and Discussion

### 3.3.1 Nanotube growth post anneal

The addition of a 7 base toehold in strand S2 of 5 base sticky end tiles (Fig. 3.9 D) does not affect the growth pattern of assembling nanotubes. The measured mean length is consistent with results published by [13]. Nanotube growth was tested as a function of the toehold tile percentage, defined as the relative concentration of toehold S2 strand and non-toehold S2 strand in the annealing mix. We measured growth in three different assays: 1) tiles without toehold S2 strand, 2) 50% and 3) 100% concentration of toehold S2 strand. Length was measured at room temperature (25°C) using fluorescence microscopy (Methods Section 3.2.2) after a 6 hour anneal (Methods Section 3.2.1). Each assay was conducted in triplicates. Nanotube length violin plots for each assay, together with the resulting mean and standard deviation of the mean are shown in Figures 3.11, 3.12 and 3.13. Means for the three different assays are compared in Figure 3.14.

## Growth of nanotubes in the absence of toehold tiles

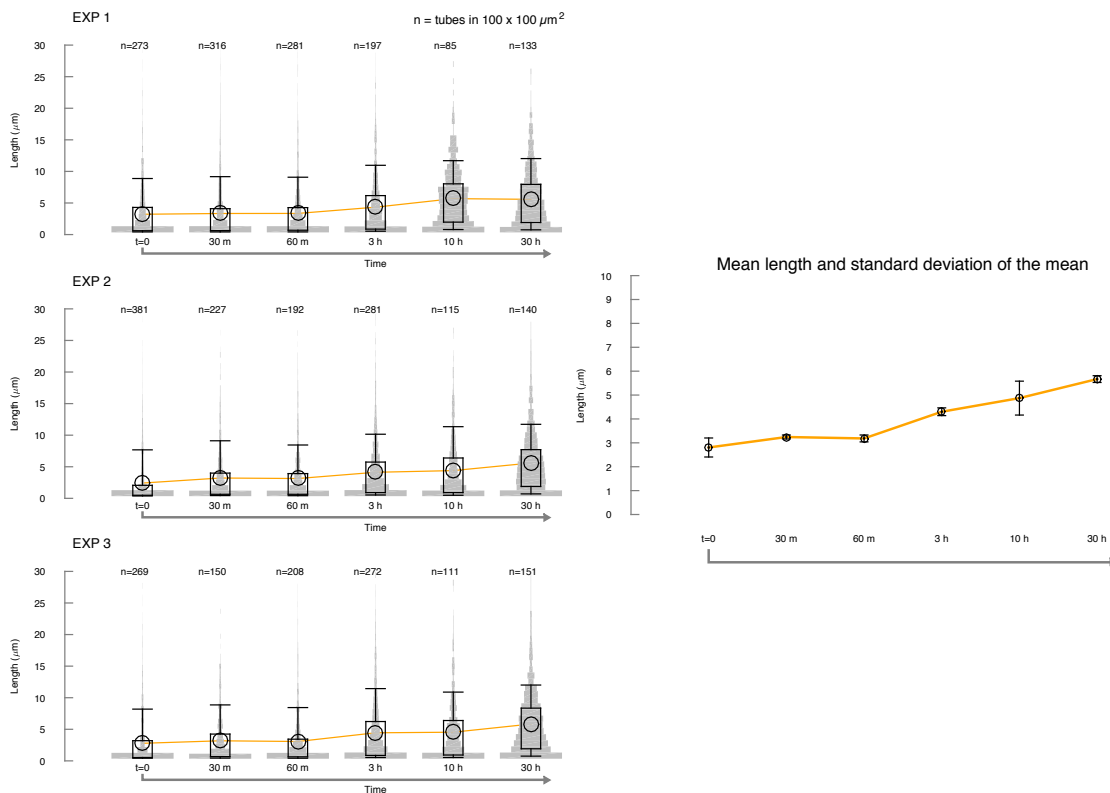


Figure 3.11: **Growth of nanotubes in the absence of toehold domain** Nanotube length was measured over 30 hours (after annealing) from fluorescence microscopy images. Left: Violin plots of each experiment repeat. Right: mean and standard deviation of the mean of length over the three experiments to the left.

## Growth of nanotubes with 50% toeholed tiles

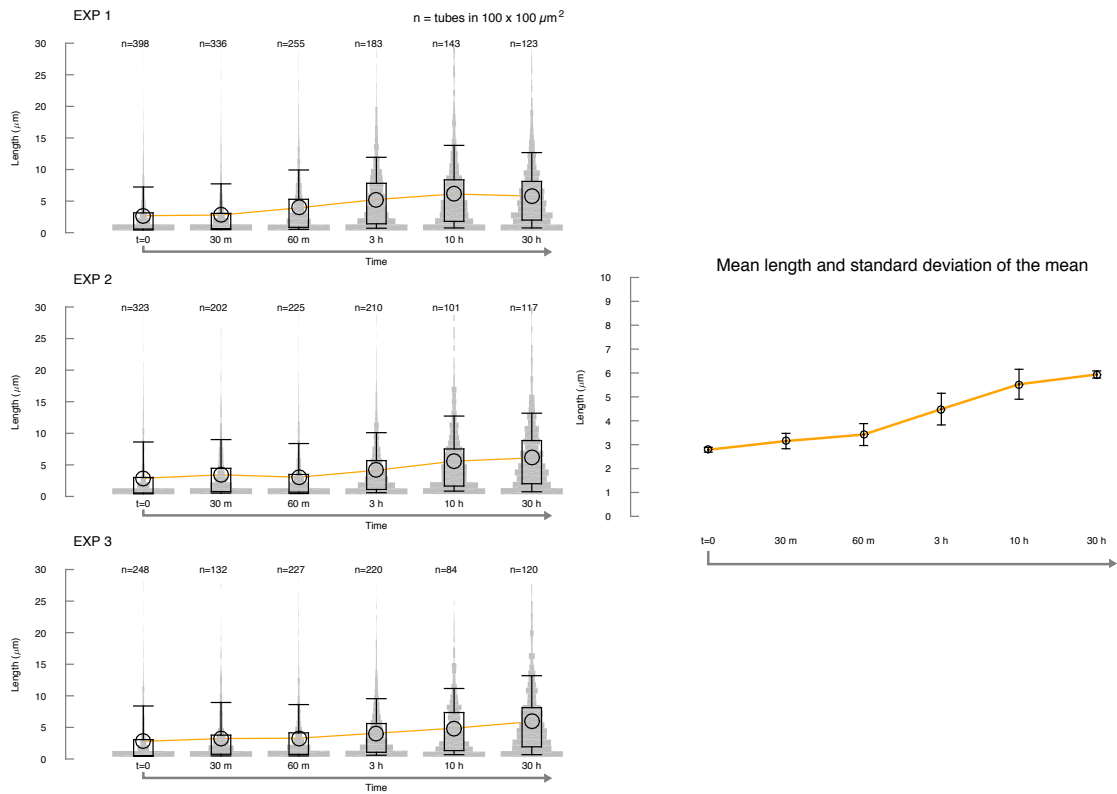


Figure 3.12: **Growth of nanotubes annealed from tile sample where 50% of tiles include a toehold domain** Nanotube length was measured over 30 hours (after annealing) from fluorescence microscopy images. Left: Violin plots of each experiment repeat. Right: mean and standard deviation of the mean of length over the three experiments to the left.

## Growth of nanotubes with 100% toeholded tiles

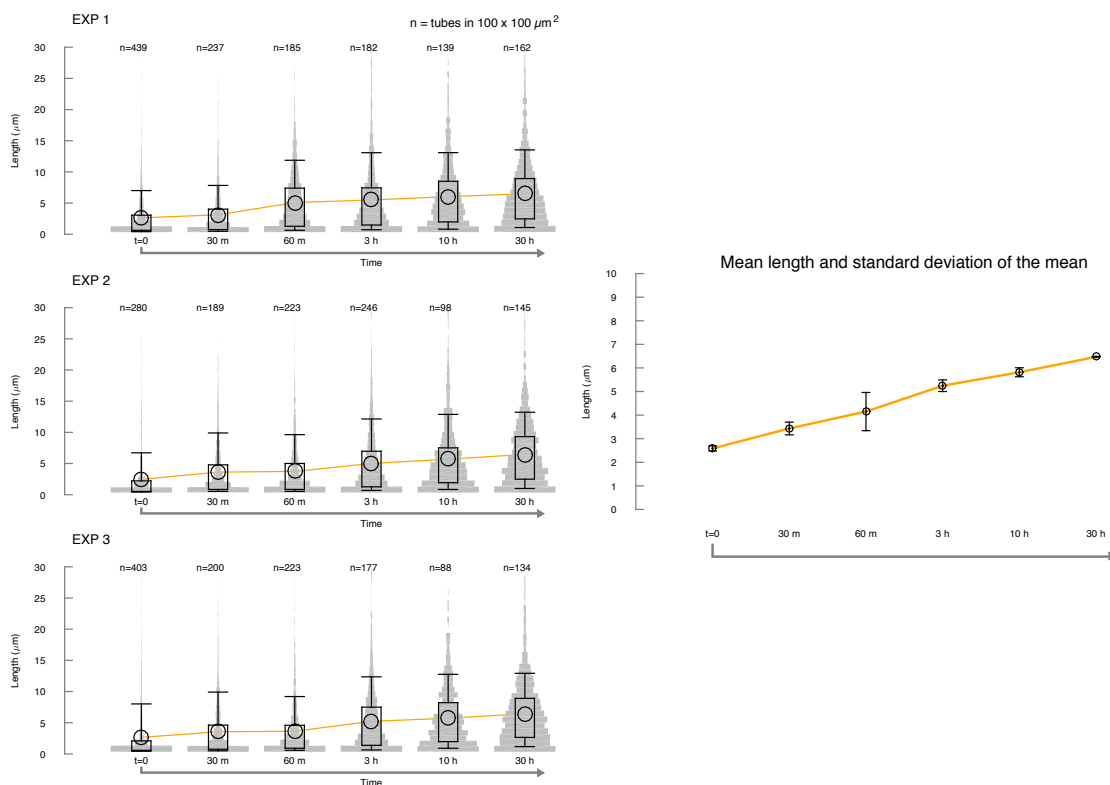


Figure 3.13: **Growth of nanotubes annealed from tile sample where 100% of tiles include a toehold domain** Nanotube length was measured over 30 hours (after annealing) from fluorescence microscopy images. Left: Violin plots of each experiment repeat. Right: mean and standard deviation of the mean of length over the three experiments to the left.

### Comparison of mean nanotube length during growth experiments with different percentage of toehold tile

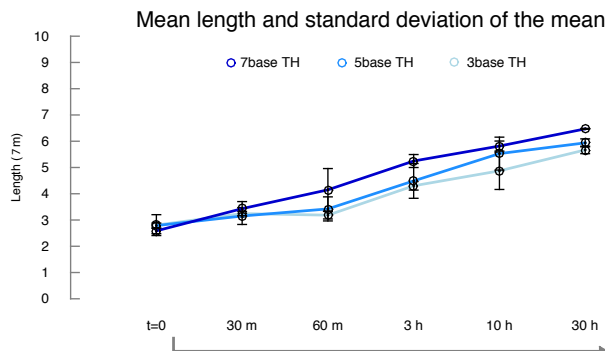


Figure 3.14: **Growth of nanotubes is not influenced by the presence of external toehold** We compare the mean length data from Fig. 3.11, 3.12, and 3.13; the nearly overlapping means indicate that the presence of a 7 base external toehold does not affect nanotube growth.

### 3.3.2 Analysis of Internal vs. External Toehold Positioning

#### Fluorescence assays confirm external and internal toehold location

The position of the toehold in the nanotube was characterized by binding of streptavidin (conjugated with a cy3 fluorophore) to a biotinylated truncated invader strand that, in turn, binds to the toeholds without causing nanotube disassembly. This truncated invader strand binds to both internal and external toeholds. Streptavidin binds to the 3 end of this strand. The expectation is that the toeholds that show up on the inner surface of the nanotubes will not be able to bind to the streptavidin-truncated invader complex since the protein will not fit inside the nanotube. The external toeholds are expected to bind to the streptavidin-truncated invader complex without any problem.

A mixture of streptavidin and truncated invader was prepared at 1:4 ratio (streptavidin is tetravalent) in 1x TAE and 12.5 mM  $MgCl_2$ . The final concentration of Truncated invader in the mix was  $1\mu M$ . The mixture was incubated at room temperature

for 30 minutes. Cy5-labeled nanotubes ( $1\mu\text{M}$ ) were mixed to the streptavidin-Truncated invader mix at 1:4 ratio of Nanotube:streptavidin-Truncated invader. The mixture was incubated at  $4^{\circ}\text{C}$  for 2 days. After incubation, the mixture was imaged in both Cy3 and Cy5 channels; example images are shown in Fig. 3.15. These images indicate that toeholds are exposed on the internal or external nanotube surface as intended. Fig. 3.15 A1 and A2 show results for internal toehold: no fluorescence is detectable in the Cy3 channel, indicating that there are no binding sites for streptavidin-bridged truncated invader; panels B1 and B2 show results for external toehold: fluorescent aggregates are visible in both channels, indicating that streptavidin-truncated invader complex binds to the external toeholds and since streptavidin is tetravalent, it binds to multiple nanotubes and promotes nanotube aggregation.

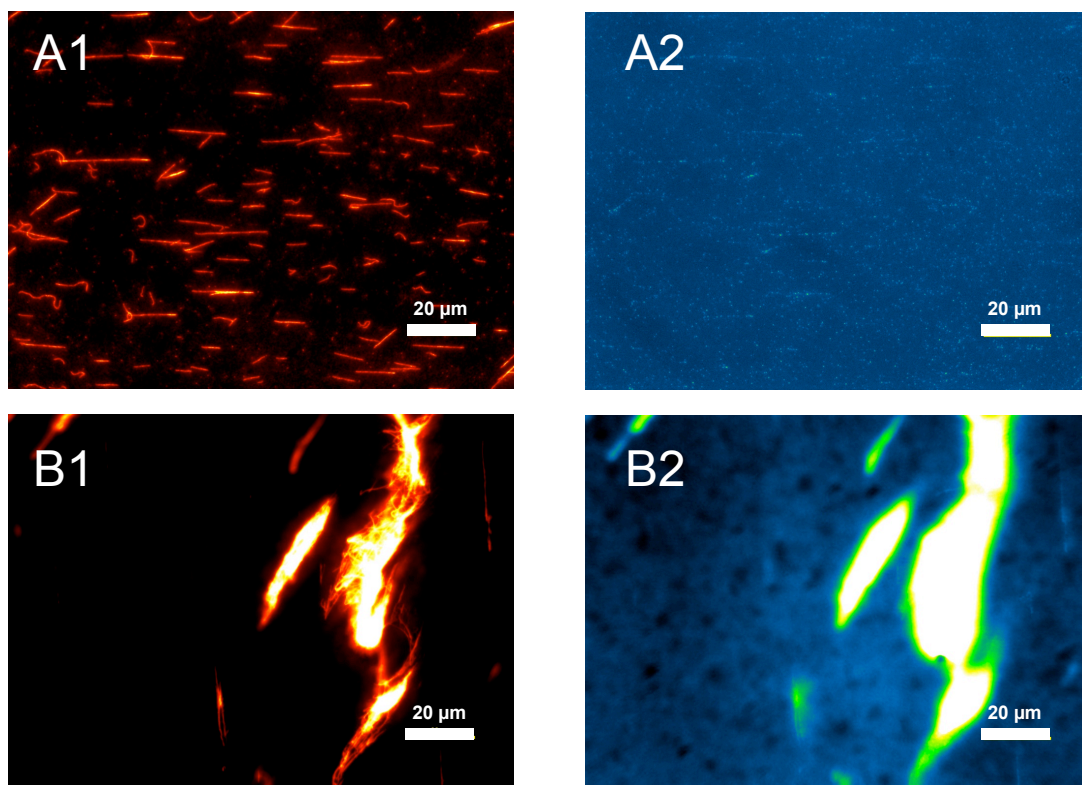


Figure 3.15: A1 and A2: Nanotubes (5b SE) with internal toeholds after incubation with Streptavidin-Truncated invader complex. A1 shows grown Cy5-labeled nanotubes. A2 is an image of the same sample with a Cy3 filter, which indicates virtually no streptavidin is bound to the nanotubes, following our expectation (toeholds are internal to the nanotube surface, therefore not available for streptavidin-truncated invader complex binding). B1 and B2: Nanotubes (5b SE) with external toehold after incubation with streptavidin-Truncated invader complex. B1 shows the Cy5 channel, and B2 shows the Cy3 channel. Both images show patches of fluorescence, which indicate that a) the streptavidin-bridged truncated invader complex binds to the external toeholds, b) due to tetravalent nature of streptavidin, it binds to multiple nanotubes and promotes aggregation.

### 3.4 Concluding Remarks

In this section we presented results of annealed DNA nanotubes with tile variation of toehold position and number of tiles with toehold as a function of nanotube stability and end growth in solution. The tiles were adopted from well defined double crossover DAE-E

tiles published in Rothmund 2004 [43]. Tile labeled with Cy3 fluorescent molecule and fluorescent microscopy allowed us to properly analyze nanotube length over the course of 30 hours post anneal at room temperature incubation. We find that the addition of toehold on 5' end of strand 2 (and the varied concentration of tiles with and without toehold) has no effect on nanotube end growth. Also, the addition of toehold on 3' end of strand 2 results in internal orientation (5' external) as predicted.

## Chapter 4

# Characterization of Triggered Assembly and Disassembly

## 4.1 Introduction

Dynamics of three-dimensional tubes will be defined as breaking and regrowing, and toehold mediated branch migration is the basis of our experiments. Each tile will be composed of a free toehold domain, that will allow for invasion of a single stranded DNA, fully complementary to the toehold region, and partially complimentary to several nucleotides of a hybridized sticky end of a tile. Once the invader and tile's toehold begin interacting, strand displacement will occur (resulting in the breaking of tiles). Branch migration will also be used in the re-formation of tubes.

### 4.1.1 Toehold-Mediated Branch Migration

A toehold region is defined as a short sequence of a single strand unbound nucleotides [63]. Used as the initiation location for strand displacement, many factors play a role in efficient hybridization of the incoming strand, resulting in final branch migration. Figure 4.1 illustrates the three stages that are used to simplify the process of toehold-mediate branch migration, Initiation: where the displacing strand is in close proximity to complex (A), Intermediate: displacing strand is interacting with complex (B.), and Completion: displacing strand is now completely bound, forming a new complex and fully removing previously bound strand (C.) [63]. Depending on the defined structures, this process can be either reversible, or non-reversible.

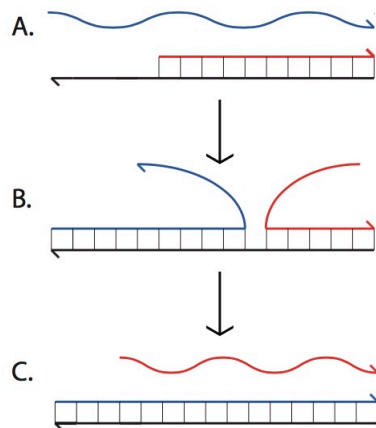


Figure 4.1: 3 Stages of Toehold-Mediated Branch Migration

Initial characterization of strand-displacement of Yurke and Mills (2003), observed the kinetics depends on the number of nucleotides available on toehold [59]. Further studies indicated the toehold domains should be between 4 and 10 nucleotides [64]. In our studies, we will use toehold domains as a point of branch migration initiation to apply dynamics to our three-dimensional structures.

### **Invasion**

Invasion is the process of nanotube breakage promoted by the addition of single stranded DNA invader (Fig 4.2). Tiles are engineered to have assemble in solution through sticky end interaction. Extruding from tiles are toehold domains, or access point for invader strand to weaken tile interaction along tube. Detailed tile-invader interactions are described in Section 4.2.1.

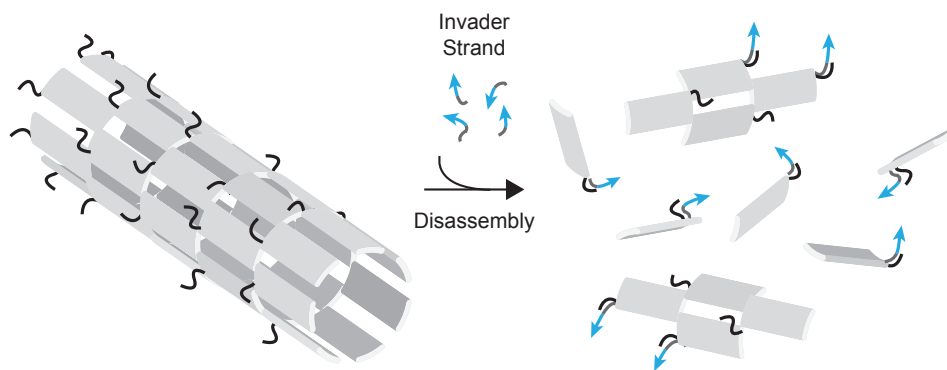


Figure 4.2: Schematic of Invasion Process

### Anti Invasion

Anti invasion is the reversible process allowing monomer tiles to reassemble forming tubes (Fig 4.3). This is possible through another layer of strand displacement by addition of second single strand DNA species; Anti invader (detailed reaction illustrated in Section 4.2.2).

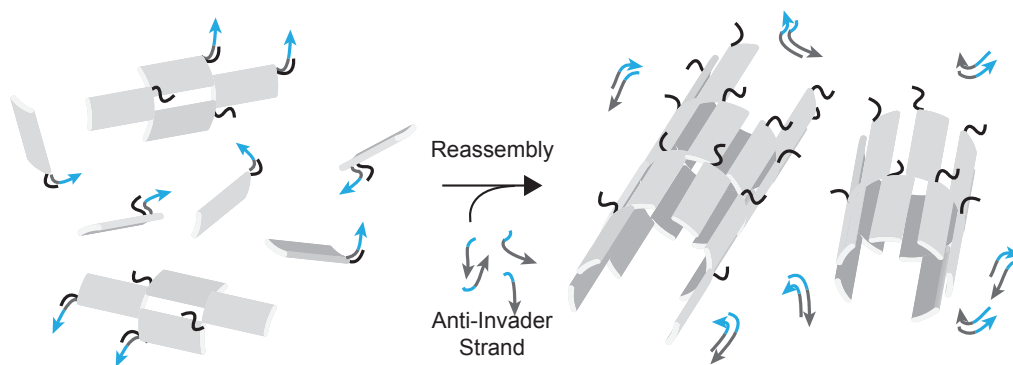


Figure 4.3: Schematic of Anti Invasion Process

## 4.2 Reaction Schemes

### 4.2.1 Invasion reaction

Fig. 4.4 illustrates the interaction of an invader strand binding to the toehold and displacing the sticky end of two hybridized tiles. (1) The example two-tile complex contains a free toehold region indicated by the black overhang domain of the complex. (2) The complementary domain of the free invader strand initiates tile displacement by interacting with the free toehold region of the tile-tile complex. (3) The invader strand completes hybridization with the toehold sticky end of the tile. To be stable, inter-tile bonds require cooperative binding of both sticky ends; thus the second sticky end is expected to unbind. This process causes nanotubes to disassemble.

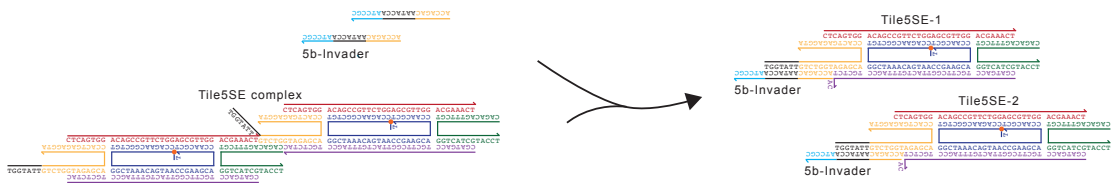


Figure 4.4: **Illustration of invasion reaction** Invasion in 5 base-long sticky end tiles.

### 4.2.2 Anti-invasion reaction

The mechanism of tube invasion has been designed to be reversible: by including a toehold on the invader strand, it is possible to displace it from tiles using a complementary anti-invader strand. By displacing and titrating the invader, the anti-invader restores the ability of tiles to nucleate and polymerize. This reaction is shown in Fig. 4.5 using two invaded tiles; displacement of the invader promotes inter-tile bond formation. (Stable bonds are formed only when both sticky ends bind to a nucleated site or growing

lattice/tube)

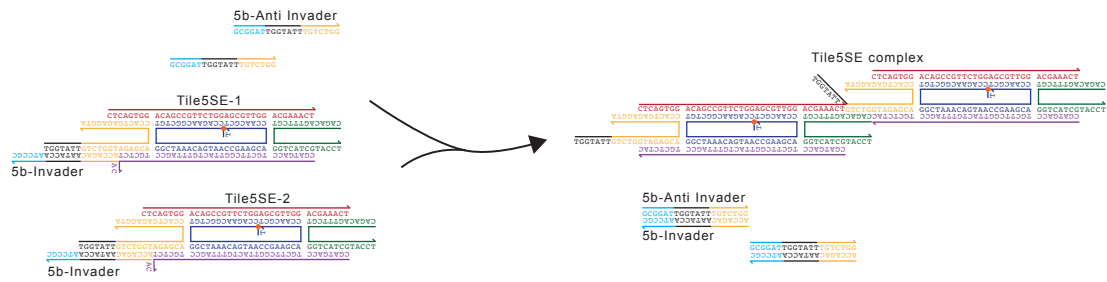


Figure 4.5: **Illustration of anti-invasion reaction A:** Anti-invasion in 5 base-long sticky end tiles.

### Side reactions

The anti-invader strand is complementary to one of the sticky end domains in strand S4. This undesirable bond is presumably weak in 5 base-long sticky ends but is expected to be more stable in 7 and 8 base-long sticky end tiles.

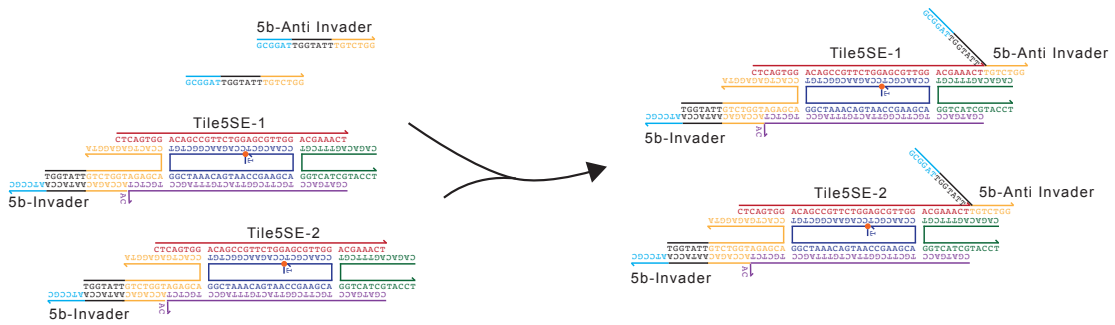


Figure 4.6: **Anti-invader can bind to strand S4** A: Interaction in 5 base-long sticky end tiles is limited to 5 bases, and is therefore likely unstable.

## 4.3 Results and Discussion

### 4.3.1 Invasion and anti-invasion reactions: Example images

Fluorescently labeled DNA nanotubes can be visualized and analyzed as described in Methods Section 3.2.2 and 3.2.4 as illustrated in 4.7 and 4.8. Nanotube lengths are processed from microscopy images A:C using methods described in Section, 3.2.3.

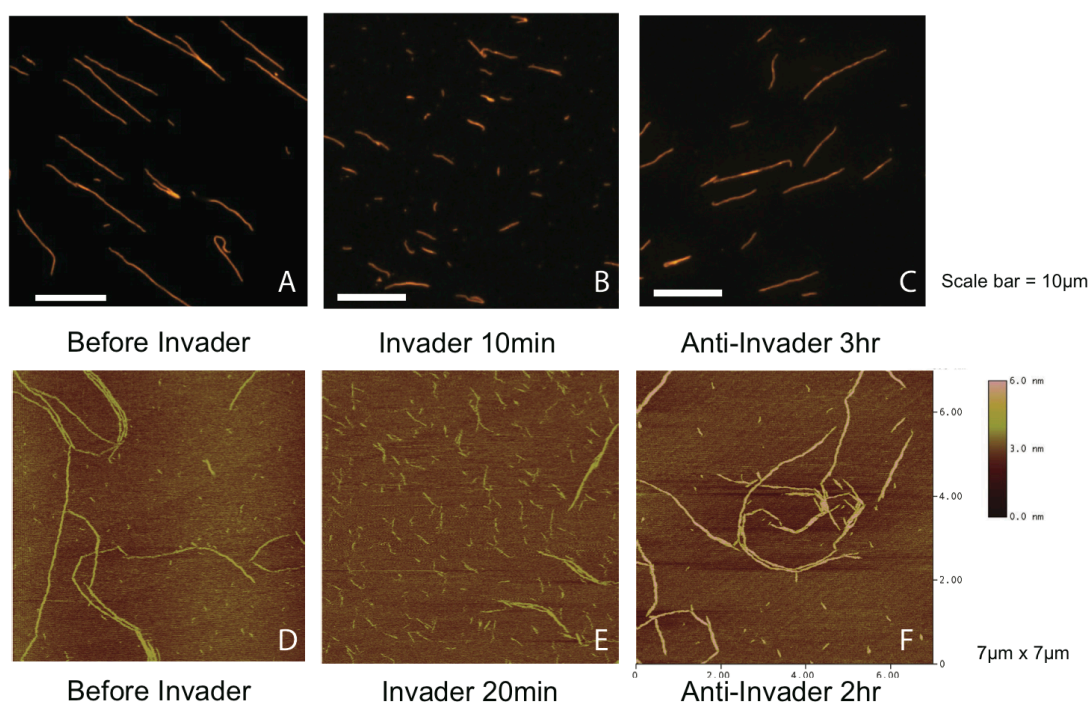


Figure 4.7: Tubes with 50% tiles containing toehold (A:C) Fluorescent Microscopy and (D:F) Atomic Force Microscopy. Initial tubes (A,D). Invader reduces tube length significantly, yet tubes are still visible in both microscopy and AFM images (Figure B,E). The addition of anti-invader to tube solution allows nanotube regrowth (C,F).

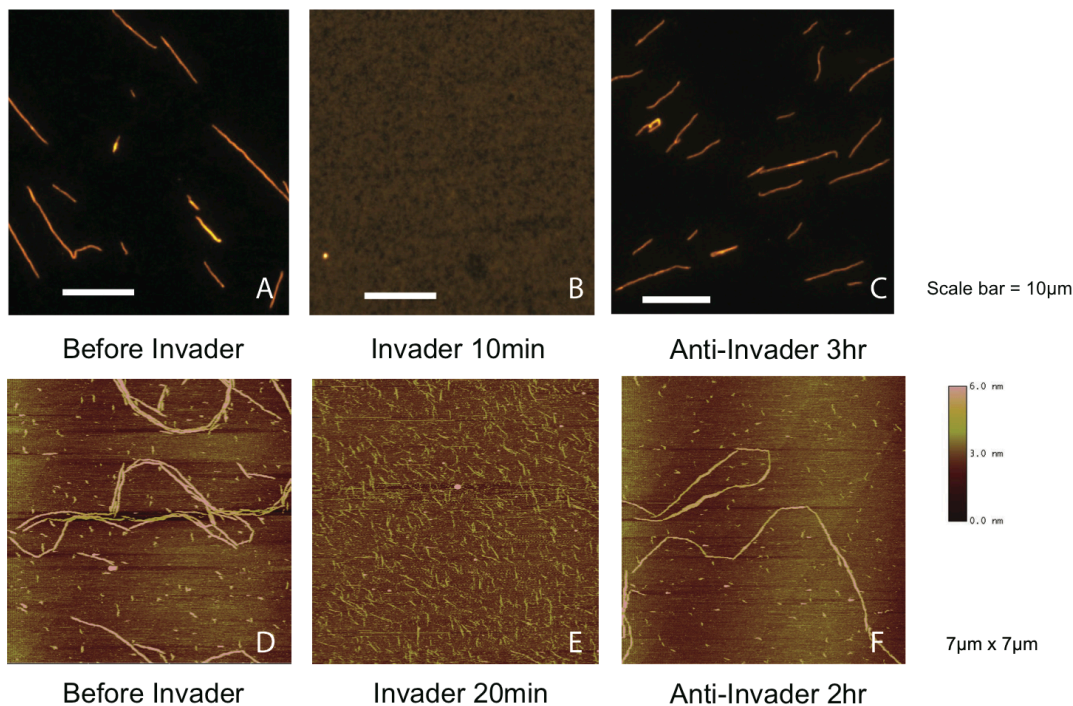


Figure 4.8: Visualization of invasion and anti-invasion rxn of tubes with 100% tiles containing toehold (A:C) Fluorescent Microscopy and (D:F) Atomic Force Microscopy. Figures A and D illustrate tubes prior to invasion. After invasion reaction at room temperature, 10 min Figure B, and 20 min Figure E, tubes completely break apart. The presence of anti-invader promotes the re-assembly of tubes from monomer tiles or chunks, Figures C and F.

#### 4.3.2 Length distribution of nanotubes after invasion

We screened the steady state distribution of nanotube length in the presence of excess invader as a function of toehold tile percentage, defined as the relative concentration of toehold S2 strand and non-toehold S2 strand in the annealing mix. We considered three different assays: 1) tiles without toehold S2 strand, 2) 50% and 3) 100% concentration of toehold S2 strand. Tiles were annealed at 1  $\mu$ M concentration, and invader was added at a 5% excess concentration. Our results show that nanotubes annealed without toehold tiles are relatively resilient to the presence of

invader, and their growth is suppressed. Invasion causes a  $\approx 50\%$  decrease in the mean length of nanotubes with 50% toehold tiles, and suppresses their regrowth. Finally, the mean length in samples of nanotubes with 100% toehold tiles appear is virtually zero: no nanotubes are visible in fluorescence microscopy images, and their regrowth is suppressed. However, small assemblies are visible in AFM images (assembly may be mica-assisted).

After annealing (Section 3.2.1), nanotubes were incubated for 30 hours at 25°C prior to addition of invader. The length was measured at room temperature (25°C) using fluorescence microscopy (Methods Section 3.2.2). Each assay was conducted in triplicates. Nanotube length violin plots for each assay, together with plots of mean and standard deviation of the mean, are shown in Figures 4.9, 4.10 and 4.11. Means for the three different assays are compared in Figure 4.12.

## Invasion of nanotubes in the absence of toeholded tiles

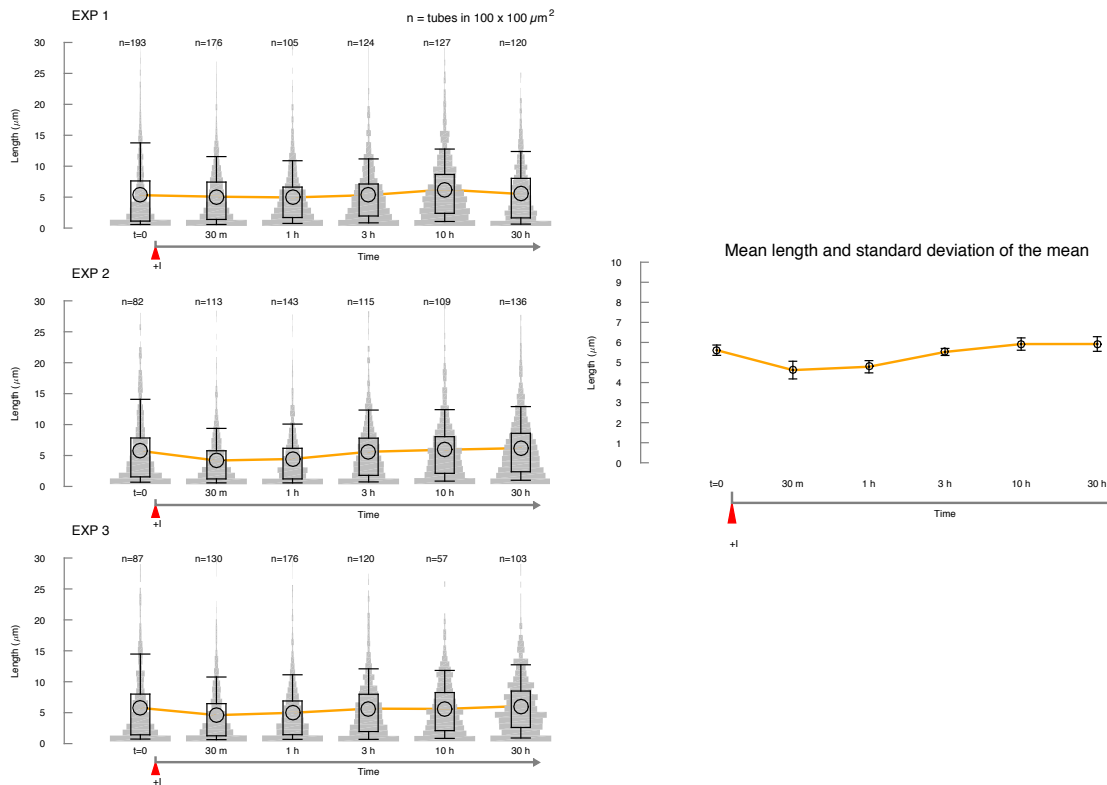


Figure 4.9: **In the absence of toeholds nanotubes do not break in the presence of invader strand.** We measure the nanotube length for 30 hours after addition of invader; prior to the beginning of the experiments, nanotubes were incubated for 30 hours, reaching a mean length of about 6  $\mu\text{m}$  [13]. The red triangle marks when invader is added to the sample. The results indicate that the invader does not significantly decrease nanotube length because the strand invasion reaction (Fig. 4.4) cannot be initiated in the absence of a toehold. However, the presence of invader appears to suppress further growth. Left: Violin plots of each experiment repeat. Right: mean and standard deviation of the mean of length over the three experiments to the left.

## Invasion of nanotubes with 50% toeholded tiles

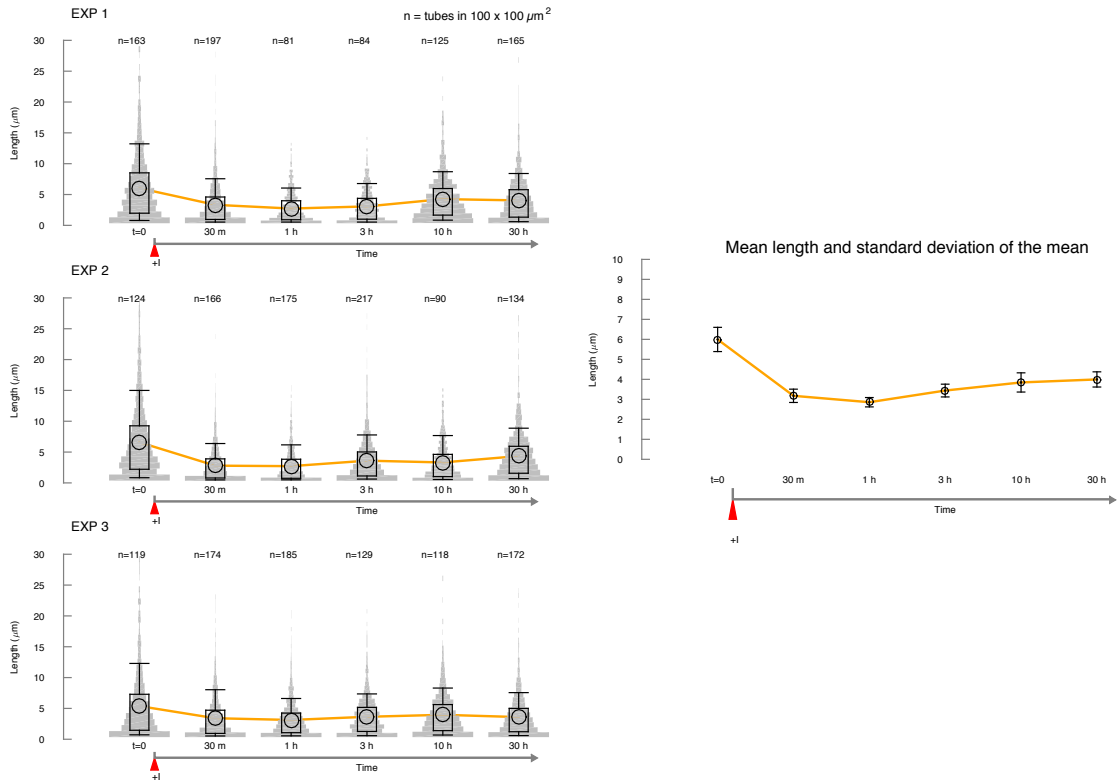


Figure 4.10: **Invasion reaction of nanotubes where 50% of tiles include a toehold domain.** After addition of invader (marked by the red triangle) the mean nanotube length rapidly decreases to half the initial length, and remains constant for the following 30 hours. Left: Violin plots of each experiment repeat. Right: mean and standard deviation of the mean of nanotube length over the three experiments to the left.

## Invasion of nanotubes with 100% toeholded tiles

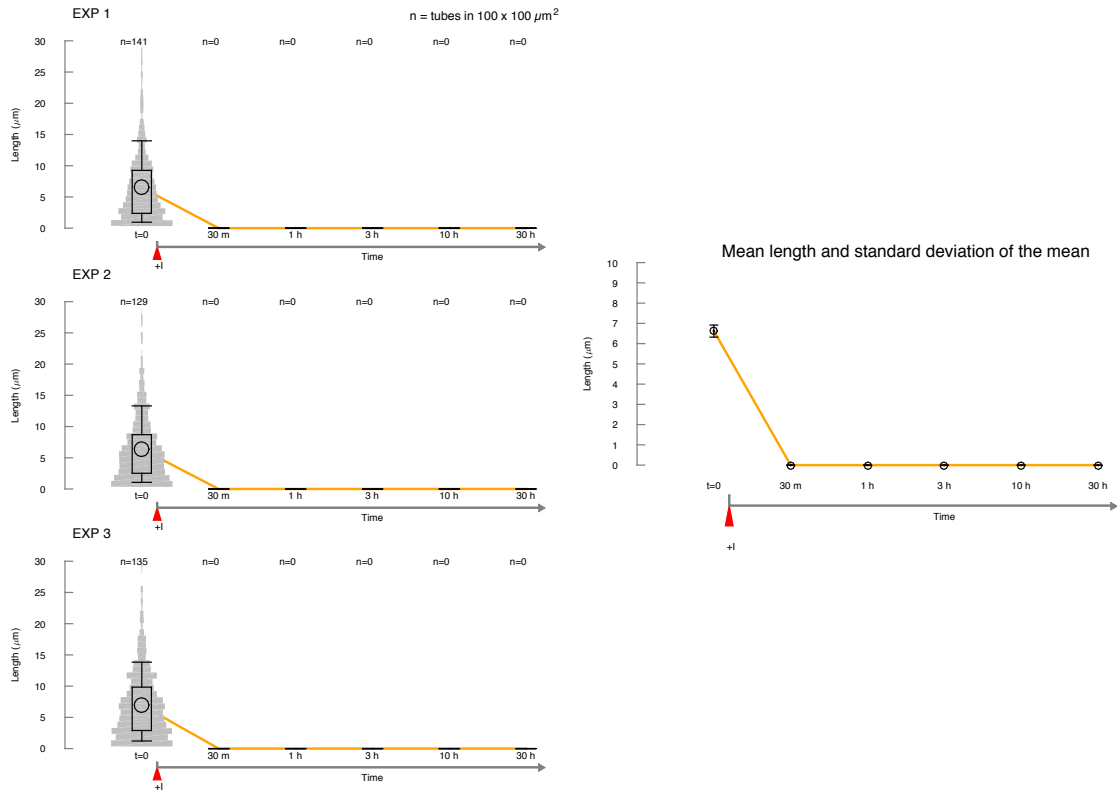


Figure 4.11: **Invasion reaction of nanotubes where 100% of tiles include a toehold domain.** After addition of invader (marked by the red triangle) nanotubes rapidly disassemble and no nanotubes can be seen in fluorescence microscopy images; nanotubes do not reform in the following 30 hours. Right: mean and standard deviation of the mean of nanotube length over the three experiments to the left.

## Comparison mean length during invasion reaction in nanotubes with different percentage of toehold tile

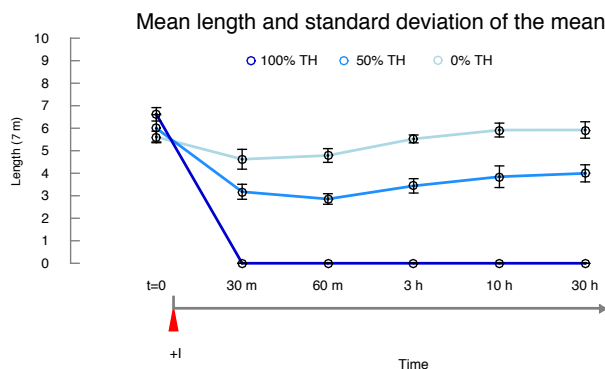


Figure 4.12: **Invasion causes a decrease in mean nanotube length that depends on the concentration of toehold tiles** This plot compares the mean length data from Fig. 4.9, 4.10, and 4.11.

### 4.3.3 Nanotube invasion as a function of toehold length

The length of the toehold in strand S2 determines the stability of the invader-tile complex. (It is also known that the speed of a toehold-mediated strand displacement reaction is proportional to the length of the toehold, as shown by [59] and many following studies). If the length of the toehold in S2 is decreased, the invader-S2 duplex is shortened and its dissociation rate is expected to become higher. To test this hypothesis, we evaluated invasion reactions in tiles with 3 and 5 bases long toehold in strand S2, and performed invasion assays as described in the previous Section 4.3.2. Our results validate this hypothesis: invasion of nanotubes assembled from tiles with shorter toeholds results in a reduction of mean length that is around 50% the initial length; in addition, after a transient nanotubes resume growth, indicating that a considerable fraction of the tile population is not bound to invader and thus available for nucleation and polymerization.

Nanotubes were annealed (Section 3.2.1) from 100% toehold tiles at  $1 \mu\text{M}$  tile concentration, using strands S2 3'T 5bp or S2 3'T 5bp (Table 3.1). After annealing,

tubes were incubated for 30 hours at 25°C. Invader was added at 5% tile concentration excess. Violin plots of the corresponding distributions, together with mean and standard deviation of the mean are shown in Figures 4.13 and 4.14. Mean length of these two assays are compared with the mean of invasion reaction on 7-base toehold tile (S2 3'T 7bp) in Figure 4.15.

### Invasion of nanotubes with 3-base toehold length

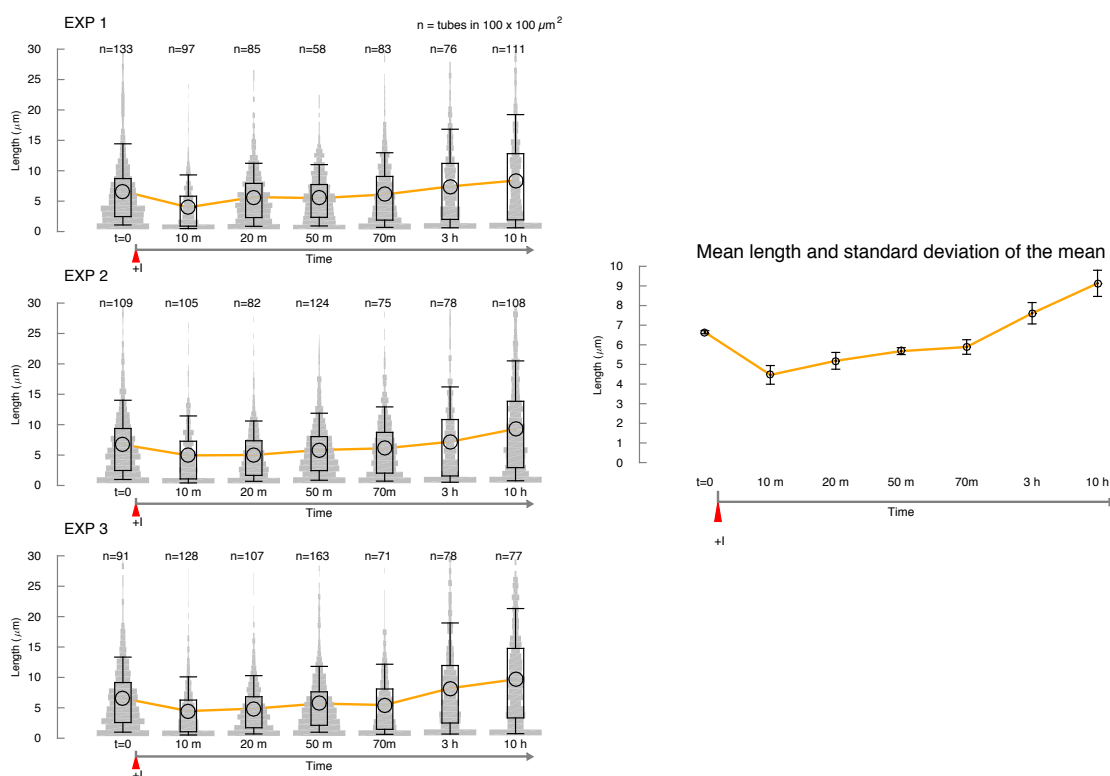


Figure 4.13: **Invasion reaction on nanotubes with 100% tiles including a 3 base-long external toehold.** A 3 base toehold is not sufficient to initiate weak breakage of nanotubes, as indicated by the slight decrease in mean length after addition of invader (marked by the red triangle). On average, nanotubes subsequently regrow reaching mean length higher than their initial length. Left: Violin plots of separate experiments. Right: Mean and standard deviation of the mean for the length distributions measured in the experiments to the left.

## Invasion of nanotubes with 5-base toehold length

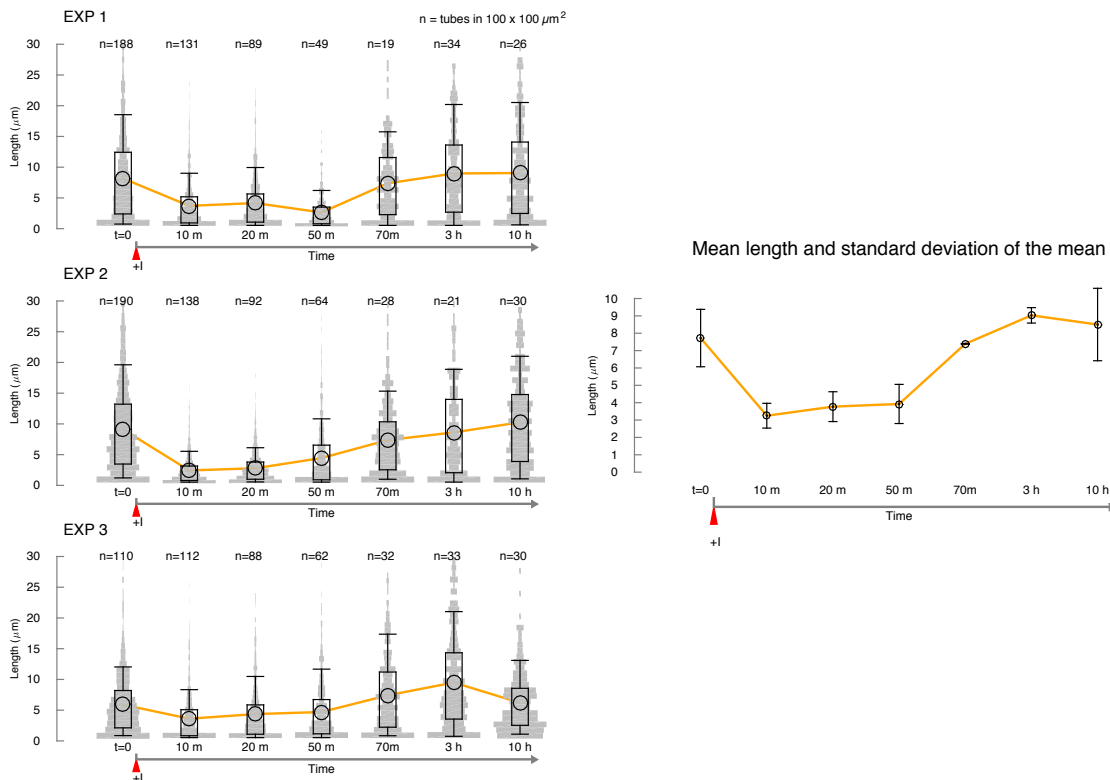


Figure 4.14: **Invasion reaction on nanotubes with 100% tiles including a 5 base-long external toehold.** A 5 base toehold is sufficient to initiate weak breakage of nanotubes. Addition of invader (marked by the red triangle) results in roughly a 30% decrease in the mean nanotube length; however, nanotubes subsequently regrow reaching mean length comparable to the initial mean length. Left: Violin plots of separate experiments. Right: Mean and standard deviation of the mean for the length distributions measured in the experiments to the left.

## Comparison of mean length during invasion reaction in nanotubes with different toehold length

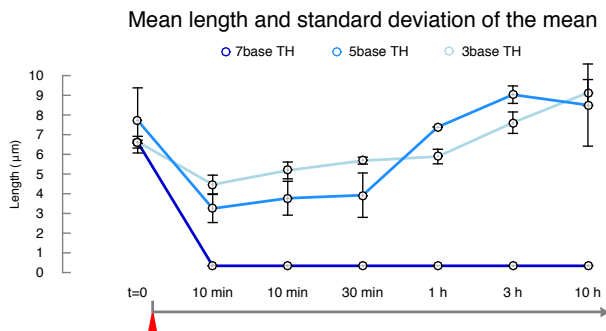


Figure 4.15: **A 7 base-long toehold is necessary to fully break nanotubes and suppress growth.** We compare the mean length measured in invasion experiments using nanotubes grown from 3 base, 5 base and 7 base-long toehold tiles (100% tiles including an external toehold). Addition of invader is marked by the red triangle. A 7 base toehold is necessary to fully break nanotubes and suppress their regrowth.

### 4.3.4 Length distribution of nanotubes after invasion and anti-invasion

Anti-invasion restores the ability of tiles to nucleate and polymerize by displacing and titrating the invader strand.

We screened the steady state distribution of nanotube length in the presence of invader and subsequent addition of anti-invader, as a function of toeholded tile percentage (defined as the relative concentration of toeholded S2 strand and non-toeholded S2 strand in the annealing mix). We report the results of three different assays: 1) tiles without toeholded S2 strand, 2) 50% and 3) 100% concentration of toeholded S2 strand. In all these experiments we used tiles with 7 base-long (external) toehold on strand S2 (Fig. 3.9 A4). Tiles were annealed at 1  $\mu$ M concentration (Section 3.2.1), and after completion of the annealing procedure, nanotubes were incubated for 30 hours at 25°C prior to addition of invader. Invader was added at a 5% excess concentration, and anti-invader was subsequently added at 10% excess concentration (relative to the

tile concentration). Invasion and anti-invasion reactions were done at room temperature (25°C).

Length distributions were measured using fluorescence microscopy images (Methods Section 3.2.2). Example images of nanotube samples post addition of invader and anti-invader are shown in Figures 4.7 (50% toehold tiles) and 4.8 (100% toehold tiles). Each assay was conducted with triplicate experiments. Nanotube length violin plots for each assay, together with mean and standard deviation of the mean, are shown in Figures 4.16, 4.17 and 4.18. Mean lengths measured in the three different assays are compared in Figure 4.19.

Addition of invader and anti-invader can be repeated multiple times, as shown in a final assay in this section. Violin plots of nanotube distributions for cycles of invasion and anti-invasion, and corresponding means are shown in Figure 4.21. In each cycle, invader was added at a 5% excess concentration, and anti-invader was subsequently added at 10% excess concentration (relative to the tile concentration).

## Invasion and anti-invasion of nanotubes in the absence of toeholded tiles

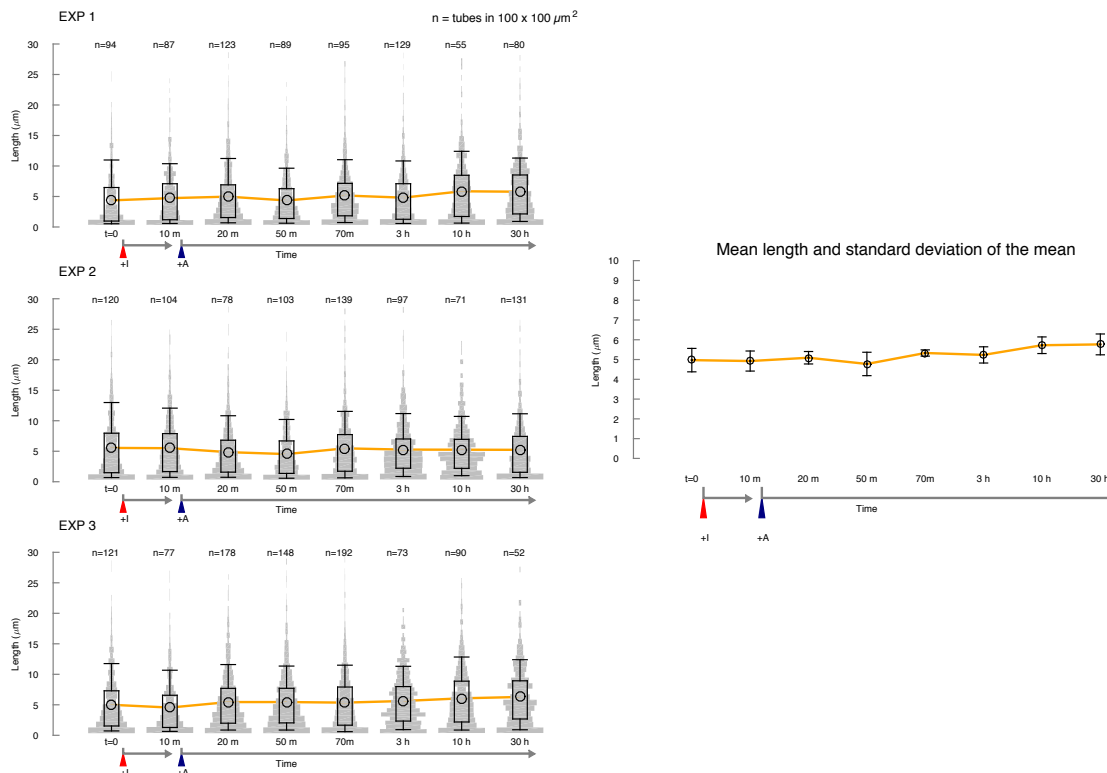


Figure 4.16: **The mean length of nanotubes without toehold is not affected by the presence of invader and anti-invader.** Red and blue triangles mark respectively the addition of invader and anti-invader. The mean length of nanotubes does not decrease after addition of invader; addition of anti-invader does not promote further growth, suggesting that nanotubes have reached an equilibrium length distribution. Left: violin plots of each experiment. Right: mean and standard deviation of the mean for the experiments to the left.

## Invasion and anti-invasion of nanotubes with 50% toeholded tiles

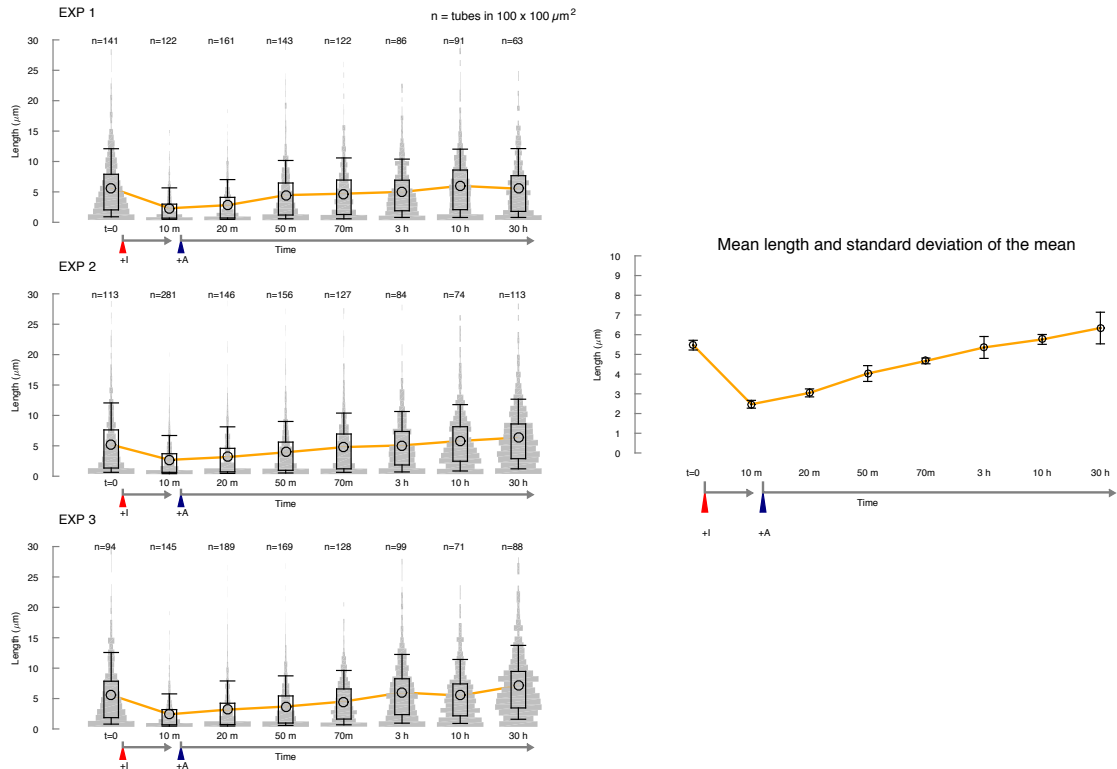


Figure 4.17: **Invasion and anti-invasion of nanotubes with 50% toeholded tiles** Consistently with the experimental results on invasion (Fig. 4.10), nanotube mean length decreases by about 50% after addition of invader (marked by the red triangle). Addition of anti-invader (marked by blue triangle) promotes regrowth to a mean length that is comparable to the initial mean length. Left: violin plots of each experiment. Right: mean and standard deviation of the mean for the experiments to the left.

## Invasion and anti-invasion of nanotubes with 100% toeholed tiles

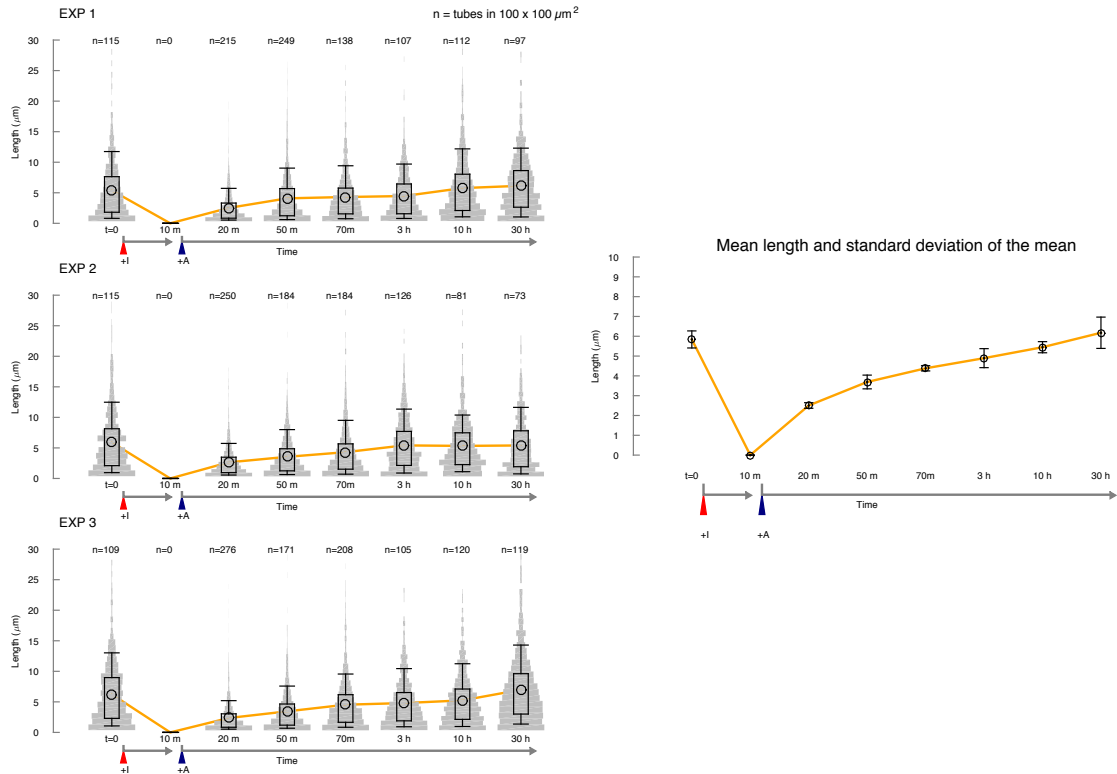


Figure 4.18: **Invasion and anti-invasion of nanotubes with 100% toeholed tiles.** Addition of invader, marked by the red triangle, results in rapid disassembly of nanotubes (no nanotubes are visible in fluorescence microscopy images). When anti-invader is added, as marked by the blue triangle, nanotubes start regrowing reaching a mean length comparable to the initial length. Left: violin plots of each experiment. Right: mean and standard deviation of the mean for the experiments to the left.

## Comparison of mean length during invasion and anti-invasion reactions in nanotubes with different percentage of toeholded tile

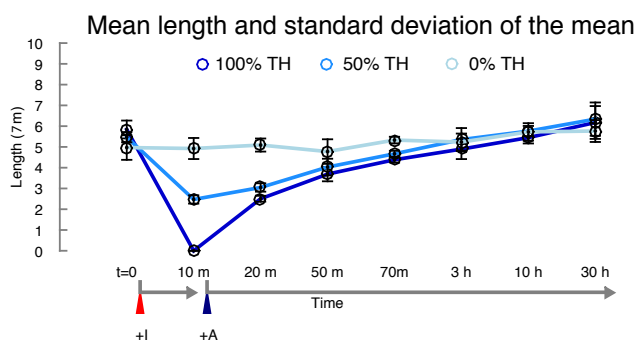


Figure 4.19: **Comparison of mean nanotube length following invasion and anti-invasion reactions for different percentage of toeholded tiles.** This plot compares the results shown in Fig. 4.16, 4.17 and 4.17.

## Gel analysis of invasion and anti-invasion reactions

Tubes containing tiles with toeholded strand S2 at different percentages were annealed using the protocol outlined in Section 3.2.1. Our tile monomer reference band was obtained by annealing all the DNA strands required for formation of tiles together with the invader strand. A high-melt agarose gel was prepared at 0.5%, 1x TAE and 12.4mM MgCl<sub>2</sub>, following the protocol described at Section 3.2.5. A sample of 2  $\mu$ L of Tubes (1  $\mu$ M ), labeled with Cy3, were reacted with 0.3  $\mu$ L (8.33  $\mu$ M) Invader for 20 min and then for anti-invasion samples, 0.35  $\mu$ L (8.33  $\mu$ M ) anti-invader was added for 2 hours at 25°C. The gel wells were sealed using thin films of solid and molten agarose. The gel was conducted at room temperature. To avoid over heating, the voltage was lowered to 60V and was allowed to run for a total time of 1 hour 30 minutes. Using Cy3 channel of BioRad Universal Hood III gel imager, the change in band intensity of breakdown products of monomer tiles, polymer smears, and tubes was analyzed and reported in Figure 4.20.

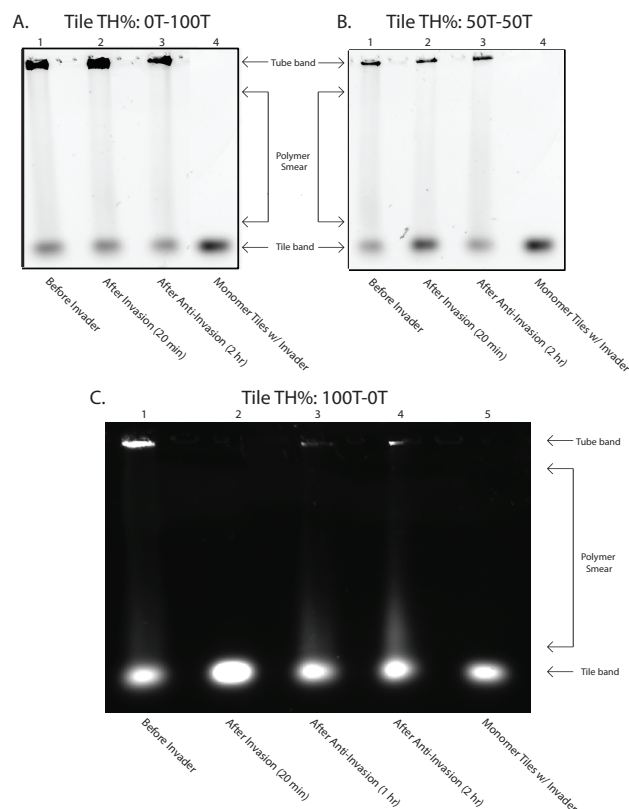


Figure 4.20: Gel Assays analyzing breakdown products of invasion and anti-invasion of various tile with toehold concentrations (external toehold). Tubes/tiles are labeled with Cy3. DX tile based tubes are too large to run through 0.5% agarose gel. Note dark (high fluorescent) bands at top of lane (A:C) indicates tubes that are not able to enter gel. Tile band (lowest bands in A:C) represents the breakdown products, or individual monomer tiles. Between the two tube and tile bands are polymer smears, or joined tiles not forming tubes. Control lane: tubes annealed with invader to form monomer tiles or breakdown products – Figures A,B = Lane 4, Figure C = Lane 5. A. 0% of tiles contain toehold. The intensity of tile bands in lanes 1:3 has no noticeable change. Tubes with 0% toehold are not shrinking when introduced to invader. B. Tubes with 50% tiles containing toehold. Lane 1, initial tube conditions after anneal, and incubation period has a faint tile band. After adding invader strand to tube solution (Lane 2), the intensity of breakdown products increases significantly. However, there are still tubes present in tube band, indicating that some tubes form shorter breakdown products, as other tubes remain intact. C. 100% of tiles has a toehold domain. Lane 1: Prior to invader, 'relatively' high fluorescent tube band; polymer smear; 'relatively' low fluorescent tile band. After 20 min of invasion rxn (Lane 2), complete tube disassembly is illustrated as both tube band and polymer smear completely disappear, resulting in 'relatively' high tile band. Lane 3 and 4 (Anti-invasion 1 hour and 2 hour incubation respectively), illustrates reappearance of polymer smear, and increase in tube band intensity.

### 4.3.5 Cycles of invasion and anti-invasion in nanotubes with 100% toe-holded tiles

Dynamics structures in nature have the ability to withstand unlimited rounds of dynamic modular behavior; whether actin cytoskeleton [57] or microtubules [8]. As motivation from the cytoskeleton's unstable dynamic ability we were able to show that invasion and anti-invasion reactions can be subsequently repeated in the same nanotube sample, yielding comparable decrease and increase of mean nanotube length at each cycle. Figure 4.21 shows the results of triplicate experiments where aliquots of invader and anti-invader were added during three separate cycles of reaction.

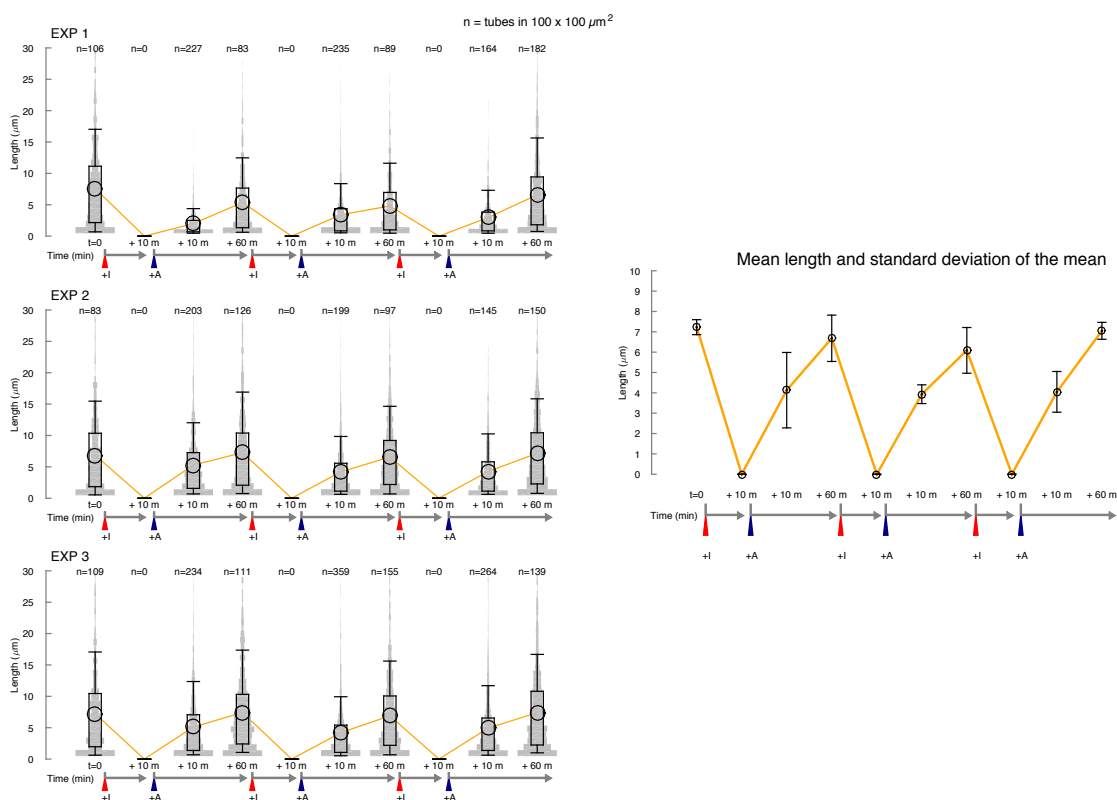


Figure 4.21: **Repeated addition of invader and anti-invader result in reversible cycles of assembly and disassembly.** Left: Violin plots of each experiment. Right: Mean and standard deviation of the mean of the experiments to the left.

### 4.3.6 MgCl<sub>2</sub> Concentration Optimization

The presence of divalent magnesium ions helps with the stability of B-helix DNA strands by interacting with the negatively charged phosphate sugar backbones [12]. In optimizing tube dynamics, we studied how divalent magnesium ions at different concentration affect the stability of the tubes being invaded and anti-invaded. Tubes were annealed using protocol in Section 3.2.1, varying the MgCl<sub>2</sub> concentration from the nominal 12.4 mM to 24.8mM, 6.2mM, and 3.1mM. Samples annealed at 3.1 mM did not result in any assembled nanotubes. All invader (5% excess to tile concentration) and anti-invader (10% excess to tile concentration) reactions were conducted in 1x TAE buffer with appropriate MgCl<sub>2</sub> concentration at 25°C.

## Invasion and anti-invasion reactions at 24 mM MgCl<sub>2</sub>

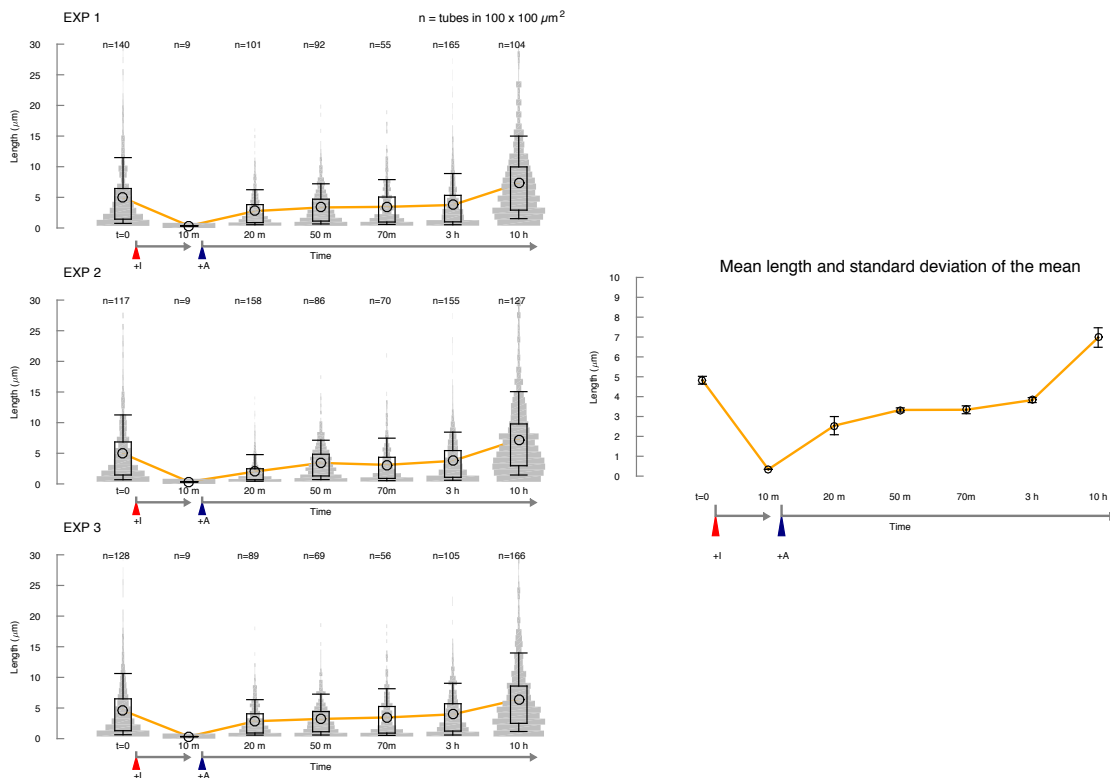


Figure 4.22: **Invasion and anti-invasion reactions in the presence of 24.8 mM MgCl<sub>2</sub>** The concentration of MgCl<sub>2</sub> in these experiments is twice the concentration used in typical annealing conditions. The mean length of nanotubes after addition of invader (red triangle) decreases to zero (no nanotubes are visible in fluorescence microscopy experiments). Addition of anti-invader (blue triangle) promotes nanotube regrowth as at nominal MgCl<sub>2</sub> concentration. Left: Violin plots of each experiment. Right: Mean and standard deviation of the mean of the experiments to the left.

## Invasion and anti-invasion reactions at 6 mM MgCl<sub>2</sub>

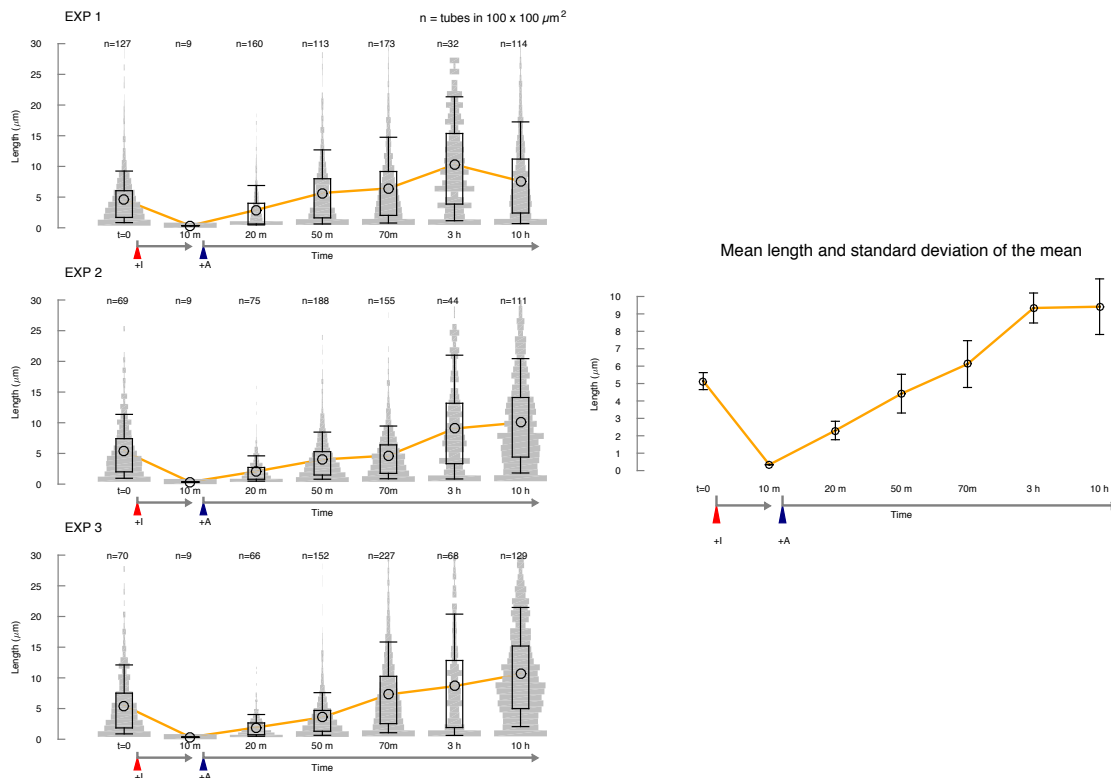


Figure 4.23: **Invasion and anti-invasion reactions in the presence of 6.1 mM MgCl<sub>2</sub>** The concentration of MgCl<sub>2</sub> in these experiments is half the concentration used in typical annealing conditions. The mean length of nanotubes after addition of invader (red triangle) decreases to zero (no nanotubes are visible in fluorescence microscopy experiments). Addition of anti-invader (blue triangle) promotes nanotube regrowth reaching a mean length that exceeds that at nominal MgCl<sub>2</sub> concentration. Left: Violin plots of each experiment. Right: Mean and standard deviation of the mean of the experiments to the left.

### Comparison of mean nanotube length after invasion and anti-invasion at varying $\text{MgCl}_2$ concentrations

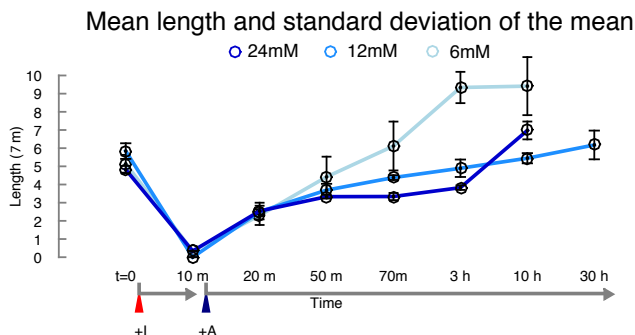


Figure 4.24: **Comparison of mean nanotube length after invasion and anti-invasion at different concentrations of  $\text{MgCl}_2$ .** This plot compares mean length shown in Fig. 4.22 and 4.23. These results indicate that a concentration of  $\text{MgCl}_2$  lower than the nominal concentration (12.4 mM) facilitates nanotube regrowth.

#### 4.3.7 Invasion and anti-invasion reactions on nanotubes with internal toehold

We tested the capacity of invasion and anti-invasion reactions to modulate the length of 5 base sticky-end nanotubes with 7 base-long toehold designed to be exposed on the internal surface of the nanotubes (toehold is positioned on the 3' end of strand S2, see sequence S2 3'T reported in Table 3.1). This assay was conducted with 100% of strand S2 having an internal toehold. After annealing, nanotubes were incubated at room temperature for 30 hours; incubation results in nanotubes with mean length of  $\approx 12\mu\text{m}$ , a two-fold increase relative to nanotubes with external toehold. The reason behind this increase is yet to be elucidated. At room temperature ( $25^\circ\text{C}$ ), invader was added at a 5% excess concentration, and anti-invader was subsequently added at 10% excess concentration (relative to the tile concentration). Violin plots for each experiment in this assay and the mean length are shown in Figure 4.25.

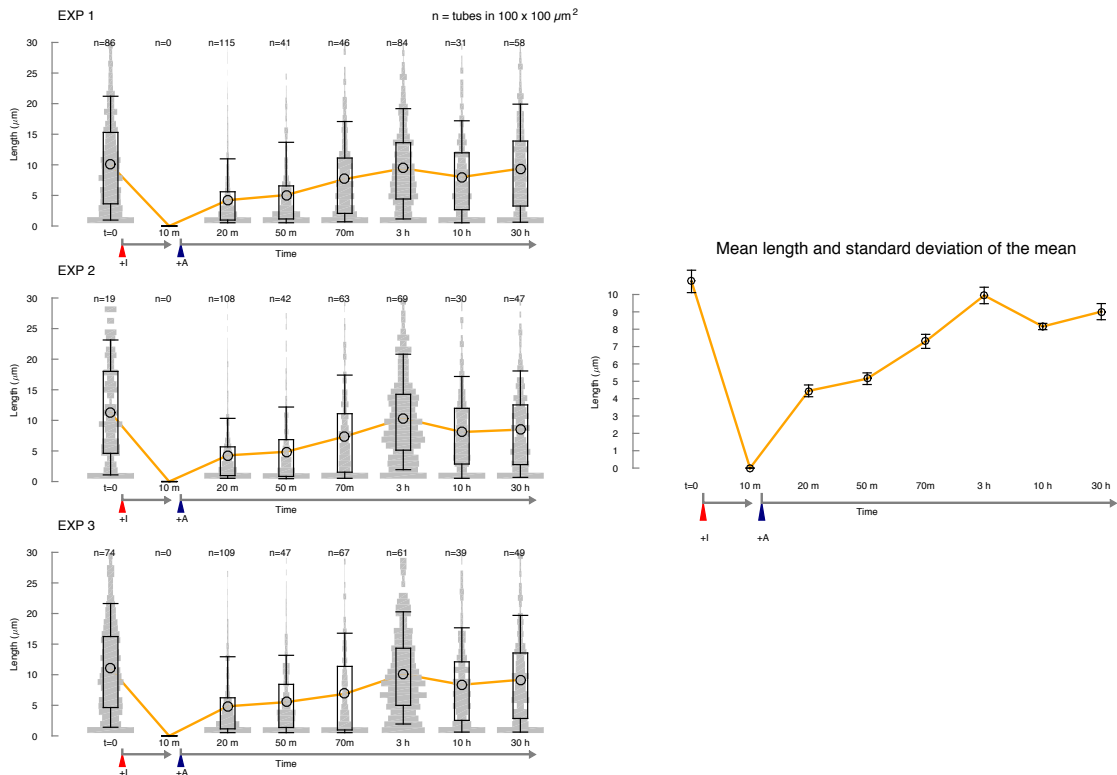


Figure 4.25: **Invasion and anti-invasion reactions of nanotubes with internal toehold.** Left: Violin plots of each experiment. Right: Mean and standard deviation of the mean of the experiments to the left.

## 4.4 Concluding Remarks

Our experiments show successful implementation of dynamics using toehold mediated strand displacement as the mechanism of nanotube breakage, and the reversible re-growth. We illustrate the robustness of our dynamic system by varying buffer conditions (magnesium++ concentration), along with partial dynamic control (varying concentration of toehold tiles). The optimal toehold length for complete and sustained breakage is 7 nucleotides. This tile design can also withstand multiple cycles of breakage and growth by repetitive addition of invader and anti invader strands.

## Chapter 5

# Designing DNA Tiles Suitable for Transcriptional Buffer Conditions

## 5.1 Introduction

In biological cells, gene networks are responsible for both the production of assembling components, and for the regulation of self-assembly pathways. Coupling DNA based nanostructure to synthetic enzymatic circuits and reactions requires robust compatibility of nanostructure in more complex buffer environments. Previous studies of synthesized two- and three-dimensional DNA bases nanostructures were conducted in well characterized and controlled buffer conditions similar to those outlined in Section 3.2.1. Because genelet systems operate at 37° C and require the presence of transcription mix (transcription buffer, high concentration of nucleoside triphosphates (NTPs) and high concentration of T7 RNA polymerase, we developed tile variants which can assemble into nanotubes under transcriptional experimental conditions. By extending the sticky ends of the tiles (without modifying the inter-tile crossover distance) from 5 bases to 7 and 8 nt long, we were able to increase the nanotube melting temperature, thus increase overall stability in transcriptional environment. These assemblies are also resilient to (presumably non-specific) binding of T7 RNAP which can cause nanotubes to melt described below in Section 5.4; T7 RNAP-mediated disruption of DNA nanostructures has been observed before [16], but is still a poorly characterized phenomenon.

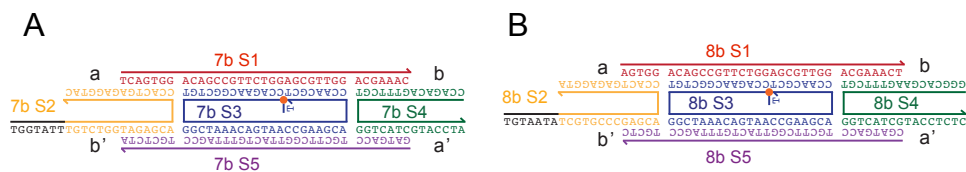


Figure 5.1: **Extended sticky-end tile variants for increased stability in transcriptional conditions** A: 7 base sticky-end Tile variants with external toehold. B: 8 base sticky-end Tile variants with external toehold

## 5.2 Methods and Materials

### 5.2.1 Transcription

Transcription mix was prepared mixing reagents for the following overall final concentrations: 1x transcription buffer (New England Biolabs, #B9012S), 5.5 mM each rNTP (Epicentre Biotechnologies, Cat. n. RN02825), 30 mM MgCl<sub>2</sub> and 0.015 U/  $\mu$ L yeast inorganic pyrophosphatase (New England Biolabs, #M2403L).

T7 RNAP was purchased from Cellscript (200 U/  $\mu$ L, # C-T7300K). *E. coli* cloned RNase H was purchased from Ambion, Cat. n. AM2292 (10 U/  $\mu$ L).

### 5.2.2 DNA Sequences

<i>Name</i>	<i>Tile with 7-base sticky ends</i>
7b S1	5'- TCA GTG GAC AGC CGT TCT GGA GCG TTG GAC GAA AC
7b S2	5'- <b>TGG TAT TTG</b> TCT GGT AGA GCA CCA CTG AGA GGT AC
7b S3	5'- T Cy3/CCA GAA CGG CTG TGG CTA AAC AGT AAC CGA AGC ACC AAC GCT
7b S4	5'- CCA GAC AGT TTC GTG GTC ATC GTA CCT C
7b S5	5'- GAT GAC CTG CTT CGG TTA CTG TTT AGC CTG CTC TA
7b Invader	5'- CCA GAC AAA TAC CAA TCC GC
7b Anti-Invader	5'- GCG GAT TGG TAT TTG TCT GG

Table 5.1: Sequences for tiles with 7-base long sticky ends, invaders and anti-invaders. Bold sequences indicate toehold domains. Strand interactions are shown in Fig. 5.1 A, 5.2 A, 5.3 A, and 5.4 A.

<i>Name</i>	<i>Tile with 8-base sticky ends</i>
8b S1	5'- AGT GGA CAG CCG TTC TGG AGC GTT GGA CGA AAC T
8b S2	5'- <b>TGT AAT ATC</b> GTG CCC GAG CAC CAC TGA GAG GTA
8b S3	5'-T Cy3/CCA GAA CGG CTG TGG CTA AAC AGT AAC CGA AGC ACC AAC GCT
8b S4	5'- GGG CAC GAA GTT TCG TGG TCA TCG TAC CTC TC
8b S5	5'- CGA TGA CCT GCT TCG GTT ACT GTT TAG CCT GCT C
8b Invader	5'- GGG CAC GAT ATT ACA CTA AGG
8B Anti-Invader	5'- CCT TAG TGT AAT ATC GTG CCC

Table 5.2: Sequences for tiles with 8-base long sticky ends, invaders and anti-invaders. Bold sequences indicate toehold domains. Strand interactions are shown in Fig. 5.1 B, 5.2 B, 5.3 B, and 5.4 B.

## 5.3 Reaction Schemes

### 5.3.1 7 and 8 base long sticky-end of: Invasion, Anti-Invasion, and side reactions

#### Invasion

Detailed reactions of tile variants 7 and 8 nucleotide long sticky ends of toehold mediated dynamics. Similar to reaction illustrated in Section 4.2.1, invader strand specific for 7 or 8 base sticky end tile interacts with respective toehold, resulting in separation of bound tiles via displacement Fig. 5.2 (tube breakage) .

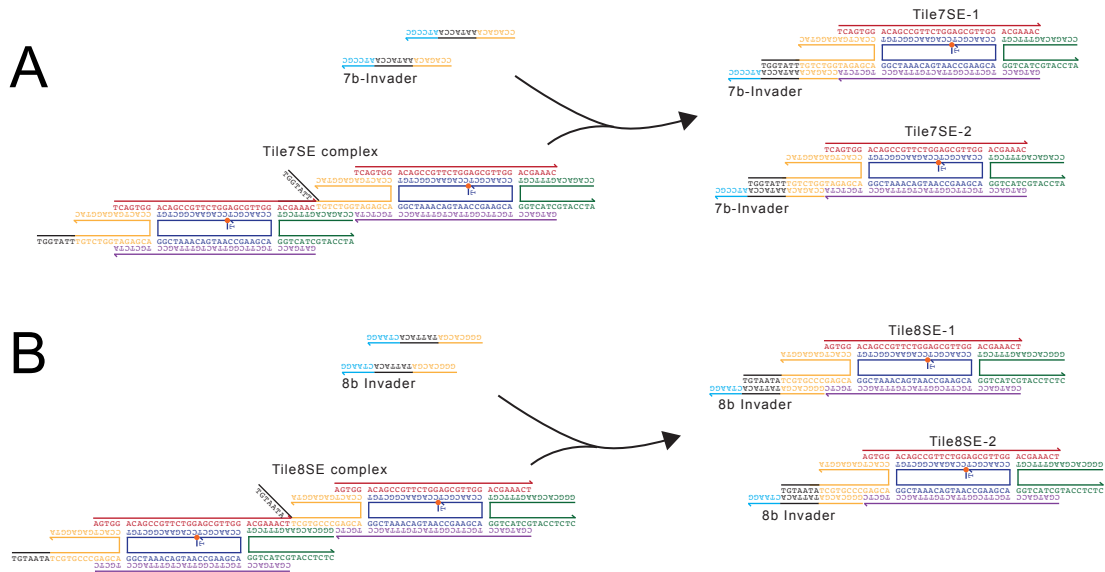


Figure 5.2: **Illustration of Invasion reactions of bound tiles** A: Interaction in 7 base-long sticky end tiles. B: Interaction in 8 base-long sticky end tiles.

#### Anti Invasion

The mechanism of tube invasion has been designed to be reversible: by including a toehold on the invader strand, it is possible to displace it from tiles using a complementary

anti-invader strand. By displacing and titrating the invader, the anti-invader restores the ability of tiles to nucleate and polymerize. This reaction is shown in Fig. 5.3 using two invaded tiles; displacement of the invader promotes inter-tile bond formation. (Stable bonds are formed only when both sticky ends bind to a nucleated site or growing lattice/tube)

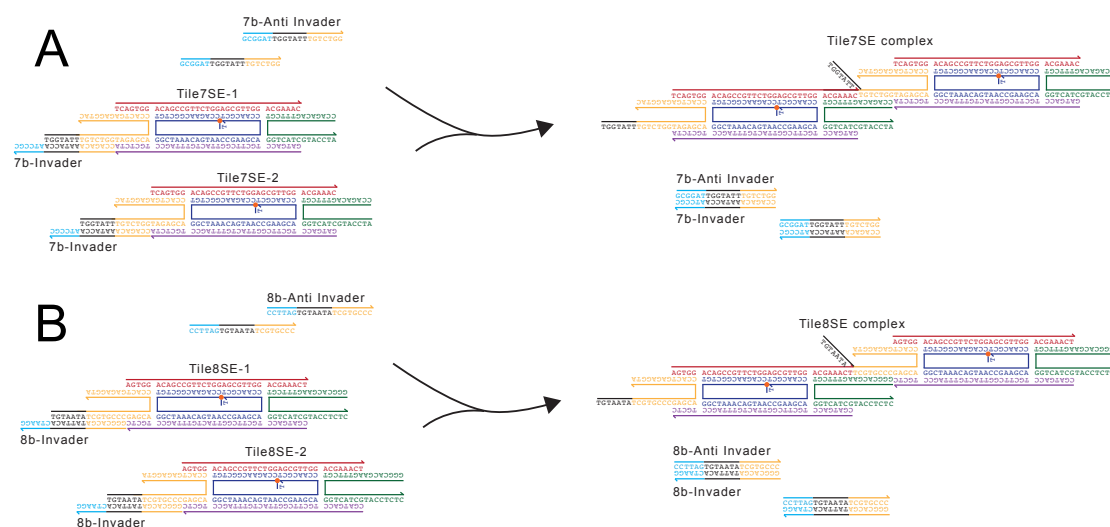


Figure 5.3: **illustration of anti-invasion reaction resulting in tube formation.** A: Interaction in 7 base-long sticky end tiles. B: Interaction in 8 base-long sticky end tiles.

### Side Reactions

The anti-invader strand is complementary to one of the sticky end domains in strand S4. This undesirable bond is presumably more stable 8 base than base-long sticky end tiles. We speculate that this interaction may contribute to the creation of a population of partially inactive tiles, and reduce nanotube polymerization rate; this hypothesis seems to be validated by experimental results on anti-invasion of 8 base-long sticky end tiles shown in Fig. 5.8.



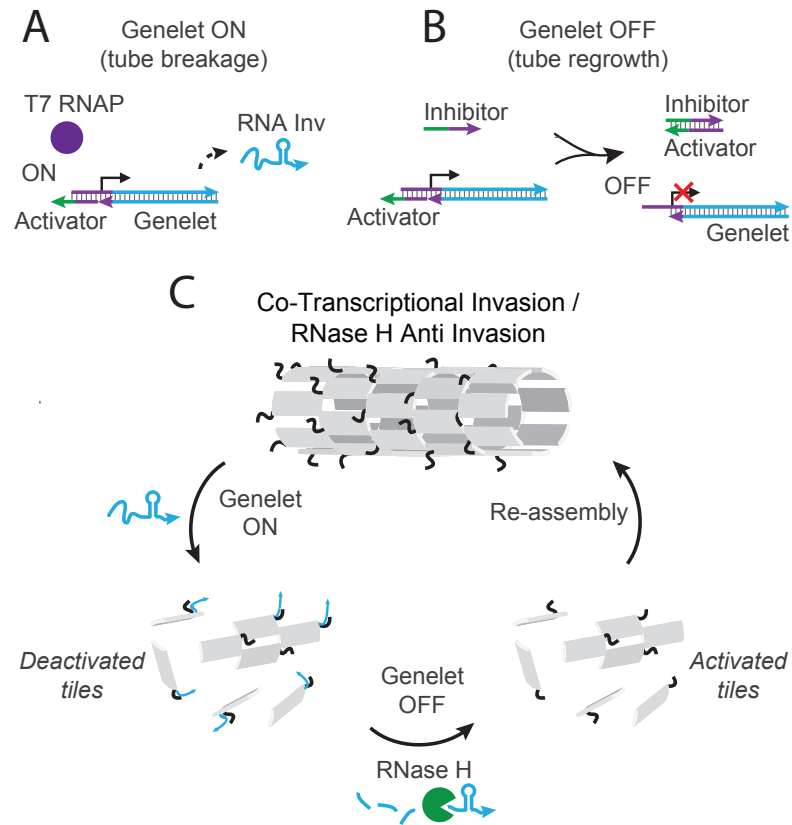


Figure 5.5: **Transpirational and Enzymatic control of DNA Nanotubes** A: Activation of genelet promoting transcription of RNA invader (genelet ON). B: Deactivation of genelet (genelet OFF) via inhibitor strand displacing bound activator from genelet. C: Schematic of nanotube dynamic. When genelet is ON, RNA invader is produced causing nanotube breakage. In presence of RNase H enzyme, turning genelet OFF results in reformation of nanotubes in solution.

Fig. 5.6 A illustrates the detailed reactions of invader transcription by T7 RNAP and the mechanism of inhibition of the genelet. Fig. 5.6 B is a schematic of tile invasion via RNA invader. Fig. 5.6 C illustrates RNase H-mediated degradation of invader which promotes reassembly.

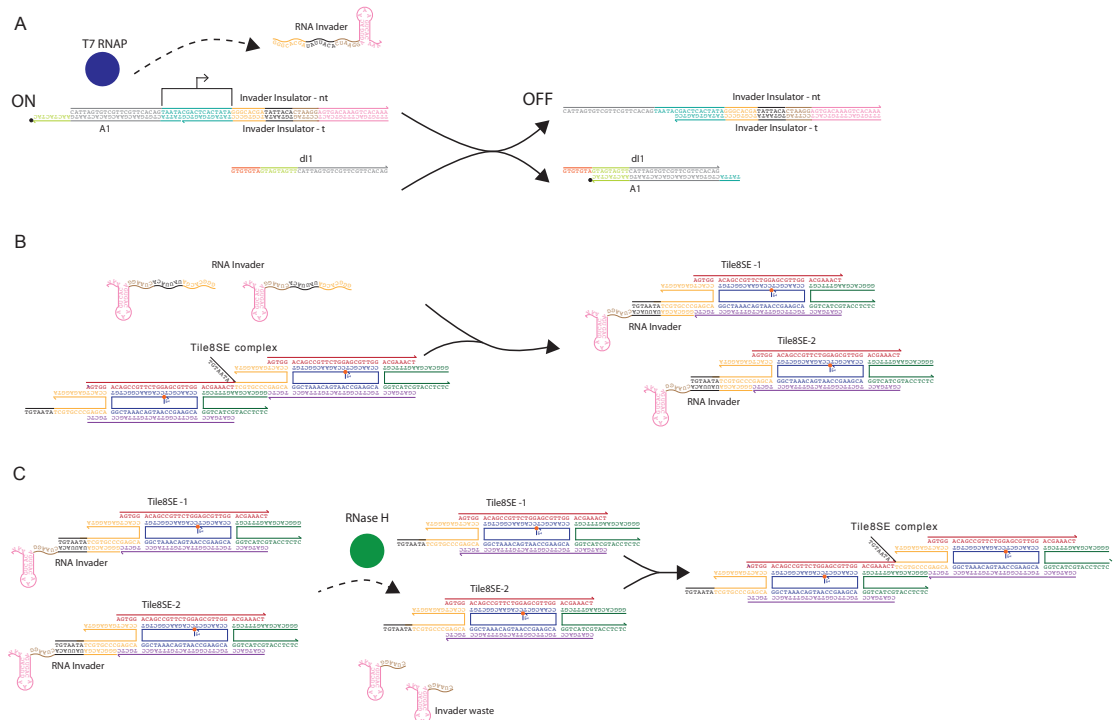


Figure 5.6: **Enzyme-driven invasion and anti-invasion reactions** A: A synthetic gene (Invader Insulator) is used to transcribe the species RNA invader. The gene can be turned off by displacement of the activator strand A1 [23] using an inhibitor strand dI1. (Species A1 and dI1 are the same used in the transcriptional oscillator described in Section 6.3.1, Figs. 6.2 and 6.3). B: Invasion reaction mediated by the RNA invader. C: RNA invader bound to tiles is degraded by RNase H, which results in the release of the sticky end domain. Tiles can therefore reassemble.

## 5.4 Results and Discussion

### 5.4.1 Invasion and anti-invasion of nanotubes with 8 and 7 base sticky ends

Nanotubes annealed from tiles having 7 and 8 base sticky ends are stable when incubated in transcription mix at 37° C. We further tested the effect of these temperature and buffer conditions on invasion and anti-invasion reactions. We find that invasion and

anti-invasion reactions on nanotubes annealed from 7 base sticky end tiles result in mean length profiles similar to what observed in 5 base sticky end tile nanotubes (Fig. 5.7). Regrowth after anti-invasion is slower in nanotubes annealed from 8 base sticky end tiles (Fig. 5.8), presumably due to the possibility of anti-invader binding to the sticky end of strand 4 (Fig. 4.6), and the formation of undesired complexes.

Fluorescence microscopy experiments were done by annealing tiles at  $1\mu\text{M}$  tile concentration in 1X transcription buffer (New England Biolab) and incubated at room temperature for 30 hours. Invader species was added at 5% concentration excess, and anti-invader was added to invaded nanotube solution at 10% concentration excess (relative to tile concentration). Violin plots and mean plots are shown in Figs. 5.7 and 5.8.

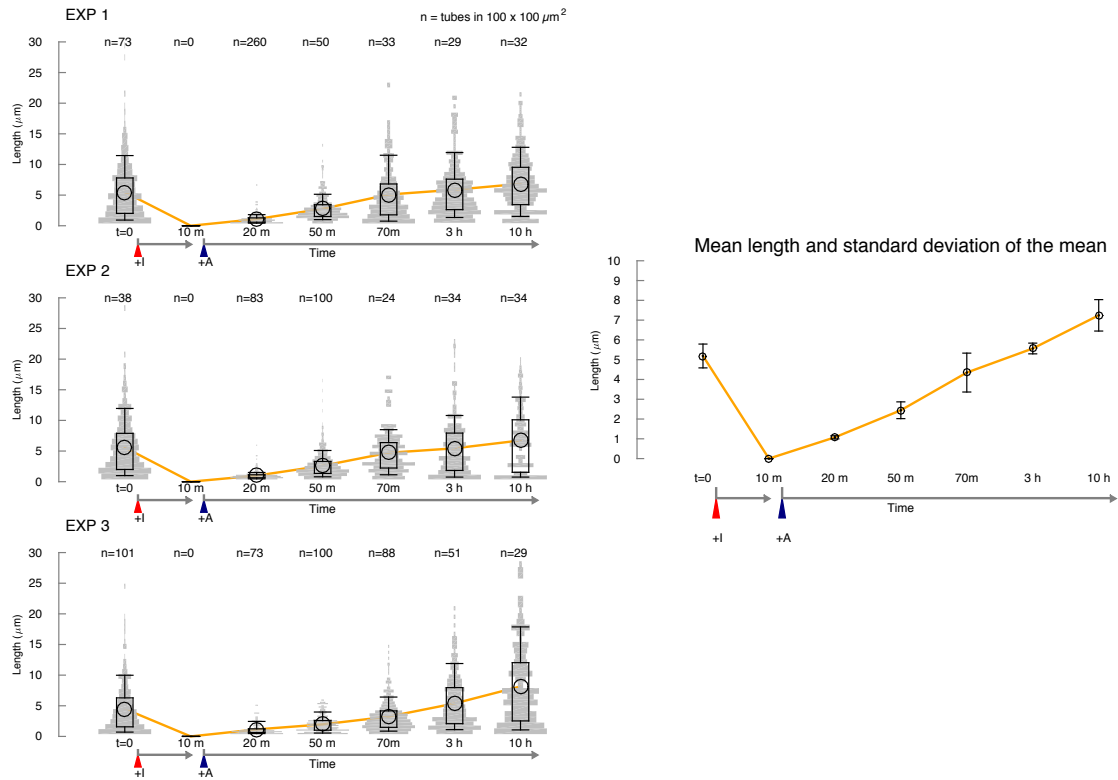


Figure 5.7: Invasion and anti-invasion of nanotubes assembled from tiles with 7 base-long sticky ends (100% toehold tiles). Addition of invader (marked by the red triangle) results in rapid disassembly of nanotubes (no nanotubes are visible in fluorescence microscopy images). When anti-invader is added (marked by the blue triangle) nanotubes regrow reaching a mean length which exceeds their initial mean length. In this case, binding of anti-invader to the sticky end of strand S4 seems to not contribute slower growth 4.6. Left: violin plots of each experiment. Right: mean and standard deviation of the mean for the experiments to the left.

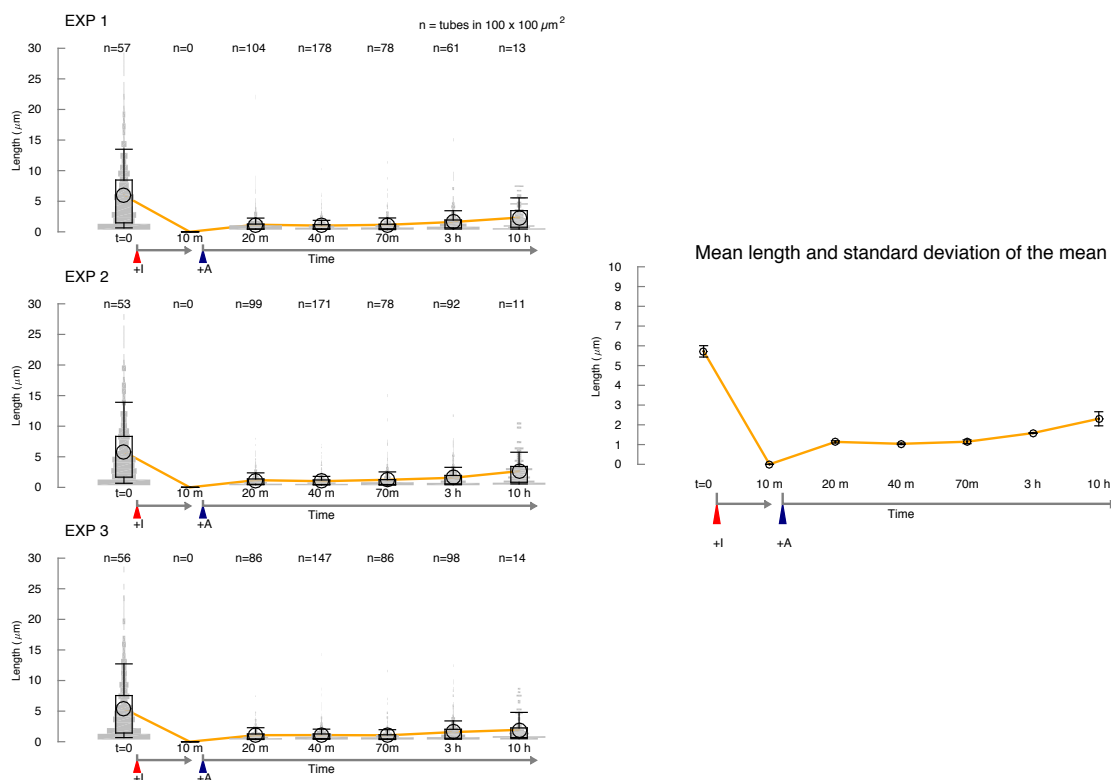


Figure 5.8: **Invasion and anti-invasion of nanotubes assembled from tiles with 8 base-long sticky ends (100% toehold tiles)**. Addition of invader (marked by the red triangle) results in rapid disassembly of nanotubes (no nanotubes are visible in fluorescence microscopy images). When anti-invader is added (marked by the blue triangle) nanotubes regrow reaching less than 50% the initial mean length. Limited regrowth may be due to two phenomena: 1) instability of the shortened tile arms, and 2) binding of anti-invader to one of the sticky ends of strand S4, which may form a stable complex in the 8 base-long sticky end tile as noted in Fig. 4.6. Left: violin plots of each experiment. Right: mean and standard deviation of the mean for the experiments to the left.

### T7 RNAP promotes disassembly of nanotubes

We designed DAE-E tiles that are stable in transcription mix and at 37°C by extending the length of their sticky ends to 7 and 8 bases. Nanotubes assembled from tiles having 7 base sticky ends are stable at 37°C and in transcription buffer, as shown in Fig. 5.9 A; however after addition of RNA polymerase and 30 minutes of incubation at 400 nM tile concentration and 37° C, the majority of tubes melt resulting in high contrast of fluorescence on surface of glass slide (background), and low number of tubes present in

solution as shown in Fig. 5.9 B.

Nanotubes assembled from tiles having 8 base sticky ends are stable at 37°C in transcription buffer and in the presence of T7 RNA polymerase, as long as nanotubes are incubated at tile concentration exceeding 500-600 nM, as shown in Figs. 5.10 and 5.11.

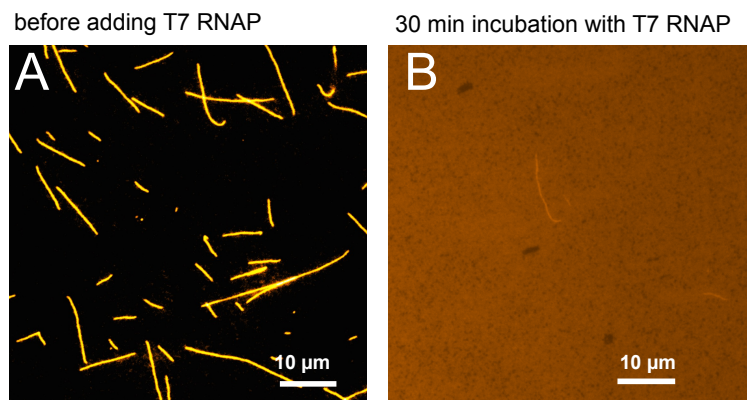


Figure 5.9: **Nanotubes assembled from tiles with 7 base sticky ends are not stable when incubated with T7 RNAP** Nanotubes were annealed at 5  $\mu\text{M}$  tile concentration, subsequently diluted to a 500 nM tile concentration and incubated in transcription buffer, at 37° C. A) Example image of nanotubes prior to addition of T7 RNA polymerase. B) Example image of nanotubes taken after 30 minutes addition of 10% (v/v) T7 RNA polymerase. Nanotubes annealed at higher tile concentration melt as well in the presence of T7 RNAP.

## 8 base sticky end nanotubes are stable in the presence of enzymes and transcription conditions

Nanotubes annealed from tiles having 8 base sticky ends were annealed at  $5\ \mu\text{M}$  tile concentration in 1X transcription buffer, subsequently diluted in transcription mix (1x transcription buffer, 20 mM  $\text{MgCl}_2$ , and 20 mM NTPs) at various tile concentrations (400 nM, 750 nM and  $2\ \mu\text{M}$ ) and incubated at  $37^\circ\text{C}$  (Fig. 5.10). Nanotubes incubated at 400 nM tile concentration melted after 15 hours at  $37^\circ\text{C}$  in RNA polymerase as shown in Fig. 5.10 A2. Nanotubes incubated at 750 nM and  $2\ \mu\text{M}$  tile concentration are stable in presence of RNA polymerase as shown in Fig. 5.10 B2 and C2. Nanotube length distributions for the 750 nM tile sample are shown in Fig. 5.11.

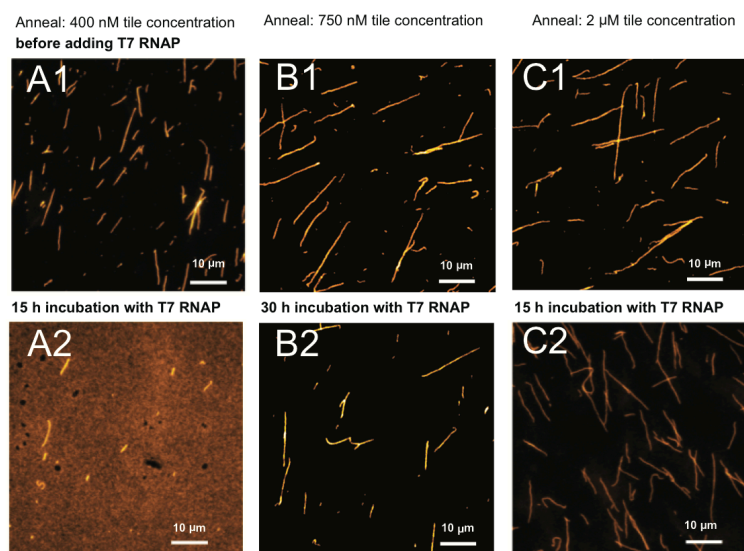


Figure 5.10: **Nanotubes annealed from tiles having 8 base sticky ends are stable in the presence of T7 RNA polymerase at high tile concentration.** were annealed at  $5\ \mu\text{M}$  tile concentration in 1X transcription buffer, and subsequently diluted in transcription mix (1x transcription buffer, 20 mM  $\text{MgCl}_2$ , and 20 mM NTPs) including 10% (v/v) T7 RNA polymerase. A1, B1, C1: Example images of nanotubes at 400 nM, 750 nM, and  $2\ \mu\text{M}$  tile concentration respectively, prior to addition of T7 RNA polymerase. A2: Example image of nanotubes incubated at 400 nM tile concentration in the presence of RNAP for 15 hours. B2: Example image of nanotubes incubated at 750 nM tile concentration in the presence of RNAP for 30 hours. C2: Example image of nanotubes incubated at  $2\ \mu\text{M}$  tile concentration in the presence of RNAP for 30 hours.

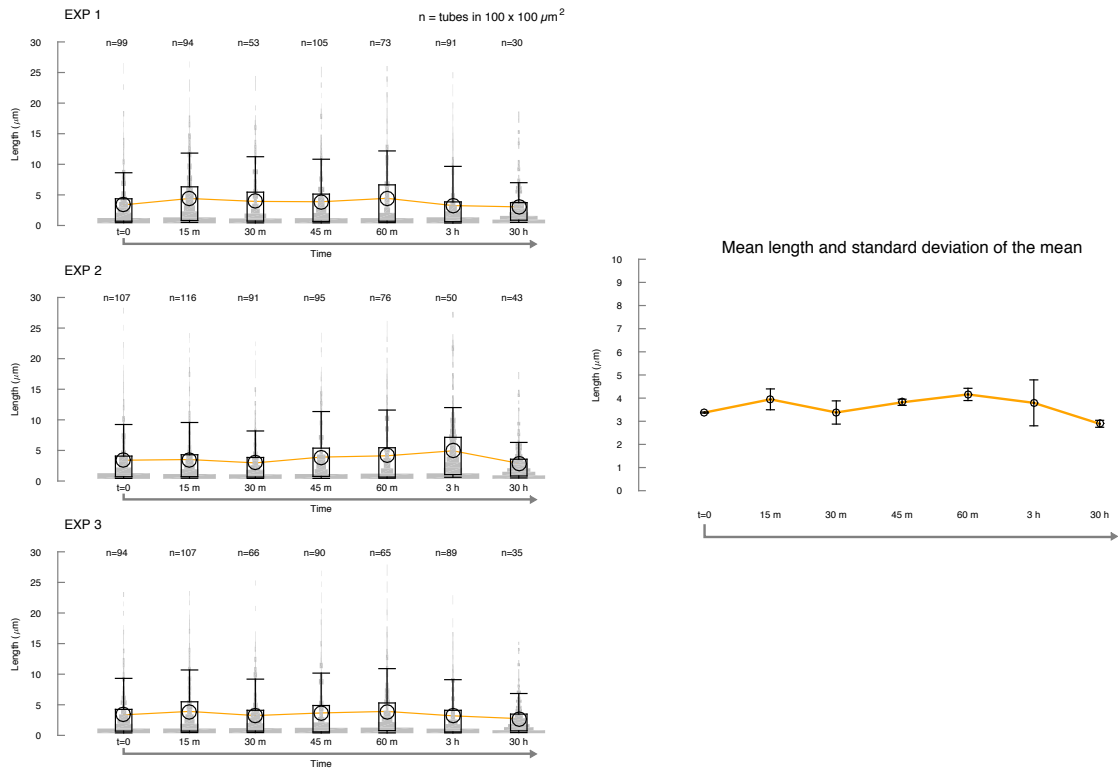


Figure 5.11: Nanotubes annealed from tiles having 8 base sticky ends are stable in the presence of T7 RNA polymerase at 750 nM tile concentration. Nanotubes were incubated at 37° C in transcription mix, in the presence of 10% (v/v) T7 RNAP. Left: Violin plots of length distributions tracked over time. Right: Mean and standard deviation of the mean of the results shown in the left panel.

## Invasion and anti-invasion reactions of nanotubes with 8 base sticky ends: bulk fluorimetry

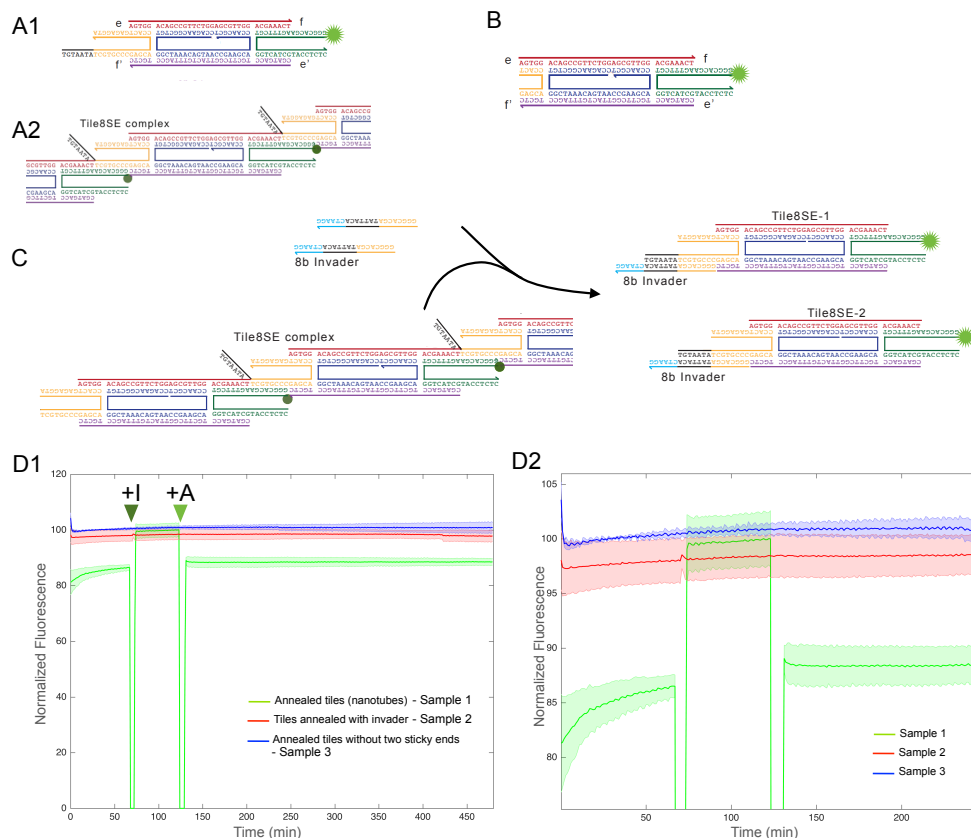


Figure 5.12: **Monitoring invasion and anti-invasion reactions using bulk fluorimetry** A1: 8 base SE tiles were labeled with a TAMRA fluorophore on the 5' end of strand 4. A2: Fluorescence is quenched when strand 4 sticky ends form a double stranded complex (assembled tiles). B: Partially blunt-ended 8 base SE tile with truncated strand 2 (tiles cannot assemble). C: Invasion reaction results in disassembly of sticky ends and therefore increase in fluorescence. D: Bulk fluorimetry data showing that invaded tiles exhibit fluorescence nearly identical to that of partially blunt-ended tiles (that are unable to assemble) and to that of tiles annealed with invader strands. Addition of invader to Sample 1 is marked by the dark green triangle (+I), and addition of anti-invader to Sample 1 is marked by the light green triangle (+A).

The fluorescence of a fluorophore attached to a single-stranded DNA can be altered upon its hybridization with a complementary DNA strand [47, 39]. Depending on the identity of the base pairs neighboring the fluorophore, the fluorescence either gets quenched or

enhanced. We took advantage of this phenomenon to track polymerization of DNA tiles by placing fluorophores at the sticky-end. Fig. 5.12 A1 shows the placement of TAMRA dye on the 8 base sticky end DNA tile (Fig. 5.1 B). Upon hybridization of the sticky ends, the adjacent G-C base pairs causes quenching of TAMRA fluorescence (Fig. 5.12 A2).

For characterizing the polymerization and depolymerization of DNA tiles using this technique, we annealed and compared the fluorescence of three samples. Sample 1: The tile shown in Fig. 5.12 A1 was annealed by itself. Sample-2: The tile in Fig. 5.12 A1 was annealed together with the invader strand (Fig. 5.12 A2). Sample-3: We annealed the partially blunt-ended tile in Fig. 5.12 B; the modified tile lacks two sticky ends and therefore cannot polymerize. We annealed the samples at 5  $\mu\text{M}$  tile concentration in 1x transcription buffer as described in Section 3.2.1. For Sample 2, the invader was added at 10% excess before annealing. Annealing Sample 1 results in nanotubes, Sample 2 results in invaded tiles and Sample 3 is a control for fluorescence of free monomers. After annealing, the samples were diluted to 1  $\mu\text{M}$  tile concentration in a solution containing 1x transcription buffer, 24 mM additional  $\text{MgCl}_2$ , 7.5 mM NTPs (each). This condition is similar to the oscillator-nanotube coupling buffer conditions (Section 6.4.1). By comparing the fluorescence of these three samples we can compare the effectiveness of invasion and anti-invasion reactions in typical oscillator coupling conditions.

We performed triplicate fluorescence measurements as described in Section 6.2.3 and 6.2.1. Figs. 5.12 D1 and D2 shows the mean and standard deviation of the mean of each triplicate experiment. Sample 1 (green trace) was allowed to stabilize for 70 minutes at 37° C; the moderate increase of the measured fluorescence indicates that the depolymerization rate of nanotubes is increased when the sample is heated from room

temperature to 37° C. After 70 minutes, 10% stoichiometric excess (to tile strands) of invader was added to Sample 1; 55 minutes after addition of invader, 20% stoichiometric excess of anti-invader (compared to tile strands) was added to Sample 1. Raw fluorescence measurements were normalized relative to Sample 3 (free monomer fluorescence) as detailed in Section 6.2.2. Fig. 5.12 D2 is zoomed version of the plot shown in Fig. 5.12 D1.

Comparison of fluorescence of samples in Fig. 5.12 D1 shows that fully formed tubes (Sample 1, green) exhibit significantly lower fluorescence than invaded tubes (Sample 2, red) and the control tiles (Sample 3, blue). This observation is consistent with our expectation that upon hybridization, the fluorescence of TAMRA is quenched. Further, the invaded tiles have fluorescence very close to that of control tiles or free monomers. This observation suggests that, upon invasion, almost all of the sticky-ended interactions are broken. When the invader is added to Sample 1, the fluorescence quickly jumps to values close to that of free monomers, suggesting that the breakage of sticky-ended interaction happens very fast. Upon addition of anti-invader to the invaded Sample 1, the fluorescence drops quickly. Our earlier microscopy results show that upon anti-invasion, tubes are visible only after 30-60 minutes. So the quick drop in fluorescence in this experiment suggests that the tiles start interacting with each other very quickly after anti-invasion, but it takes time for the tubes to grow to lengths that are visible under the optical microscope.

#### **5.4.2 Nanotube disassembly and reassembly via a cotranscribed RNA invader and RNase H**

We tested two reactions where invasion and anti-invasion are fueled by enzymes. The first reaction is cotranscriptional invasion of nanotubes directed by an individual syn-

thetic gene, that produces an RNA molecule designed to work as an invader. Nanotube were annealed from 8 base sticky end tiles in 1X transcription buffer and mixed with genelet and transcription mix at 1  $\mu$ M tile concentration. Genelet strands were separately annealed and mixed at 87.5 nM concentration with the transcription reaction mix (1x transcription buffer, 20 mM rNTPs and 14 mM MgCl<sub>2</sub>). The transcription mix was equilibrated at 37° C for 15 minutes, and then T7 RNAP (10% v/v), PPase (3% v/v), and RNAase H (2% v/v) enzymes were added to the mix. Transcription of RNA invader was activated by adding to the solution the ssDNA activator A1 125 nM concentration (A1 hybridizes to the incomplete T7 promoter on the non-template strand of the genelet), and to transcribe RNA invader strand for a total of 30 hours. After 60 minutes of reaction, nanotubes were completely broken, as shown in Fig. 5.13. Reaction schemes are shown in Fig. 5.3.2.

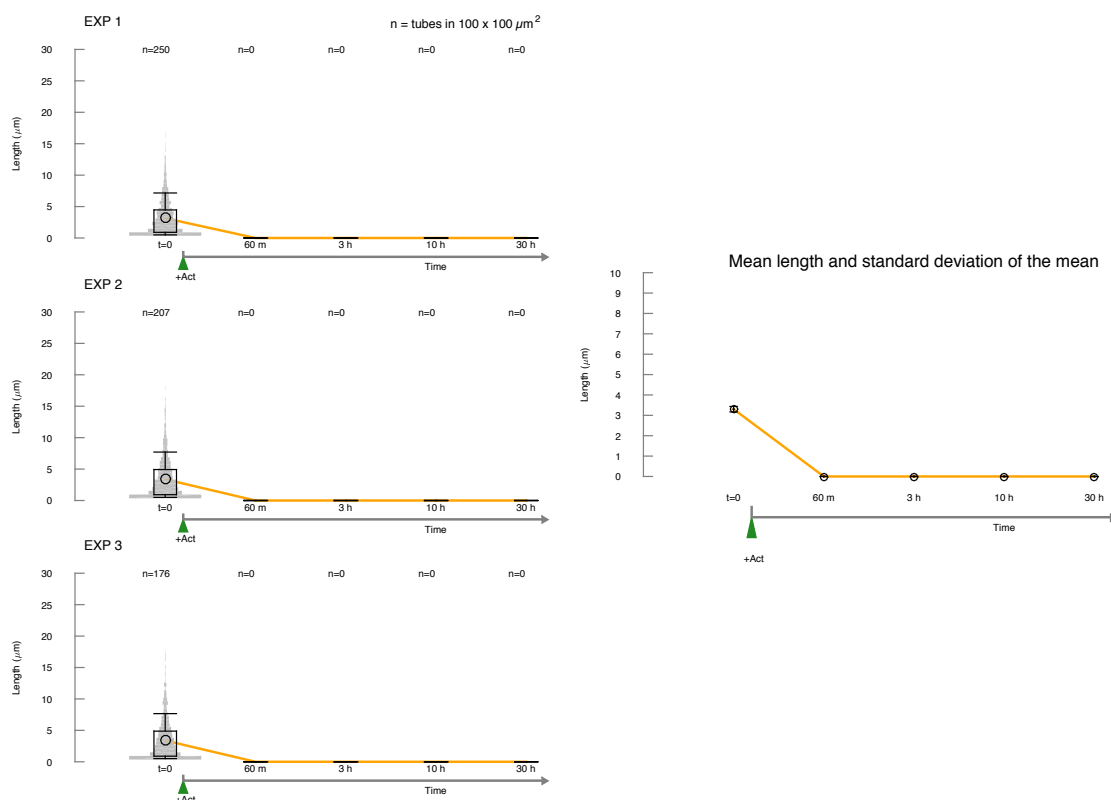


Figure 5.13: **Co-transcriptional invasion mediated by RNA** Left: violin plots of each experiment. Right: mean and standard deviation of the mean for the experiments to the left.

The second reaction tests RNase H mediated reactivation of tiles bound to invader (RNase H degrades RNA bound to DNA). Nanotubes were annealed from 8 base sticky end tiles in 1X transcription buffer and mixed with genelet and transcription mix at  $1 \mu\text{M}$  tile concentration. Genelet strands were separately annealed and mixed at  $87.5 \text{ nM}$  concentration with the transcription reaction mix (1x transcription buffer, 20 mM rNTPs and 14 mM  $\text{MgCl}_2$ ). The transcription mix was equilibrated at  $37^\circ \text{C}$  for 15 minutes, and then T7 RNAP (10% v/v), PPase (3% v/v), and RNAase H (2% v/v) enzymes were added to the mix. Transcription of RNA invader was activated by adding to the solution the ssDNA activator A1 125 nM concentration (A1 hybridizes to the incomplete T7 promoter on the non-template strand of the genelet), and allowed to

react for 30 minutes in presence of RNase H. After 30 minutes, transcription of RNA invader was stopped by adding 150 nM of inhibitor strand dI1, which displaces A1 from the promoter region. As transcription is turned off, RNase H-mediated degradation dominates, resulting in reactivation of individual tiles and tube reassembly (reaction schemes are shown in Fig. 5.6). Violin plots and mean nanotube length plots measured in these experiments are shown in Fig. 5.14.

Both reactions were tested at concentrations of T7 RNA polymerase and RNase H comparable to those used in the transcriptional oscillator experiments previously described by [23], [16], and [52].

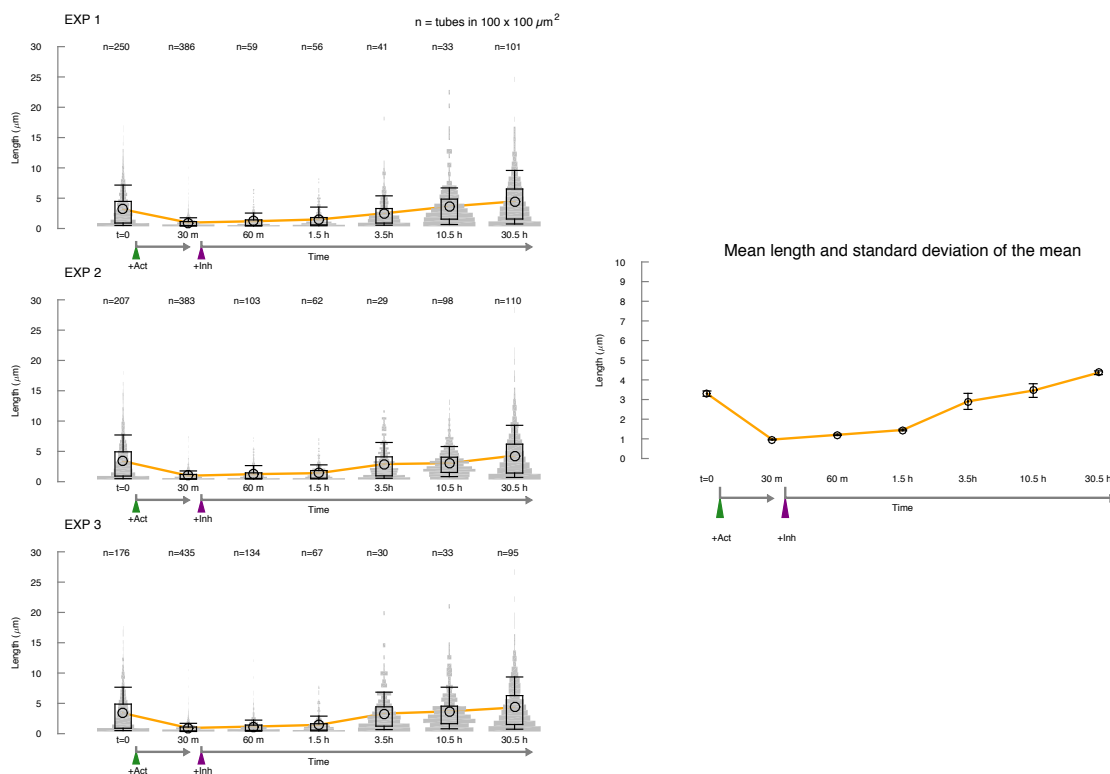


Figure 5.14: **Co-transcriptional invasion mediated by RNA, and RNase H-mediated anti-invasion of nanotubes assembled from 8 base-long sticky end tiles.** Left: violin plots of each experiment. Right: mean and standard deviation of the mean for the experiments to the left.

## 5.5 Concluding Remarks

Our experiments show that increasing sticky-end from 5-nt to 7-nt increases melting temperature of nanotubes as transcriptional conditions requires incubation temperature of 37°C. Additionally, extending sticky-end to 8 bases promotes nanotube assemblies that are resilient to (presumably non-specific) binding of T7 RNAP which can cause nanotubes to melt in solution. Transcription of RNA version of invader effectively disassembles nanotubes, and when genelet is turned OFF, in the presence of RNase H (along with T7 RNAP in solution), RNA invader is degraded from tile interaction resulting in timely, isothermal reformation of nanotubes.

## Chapter 6

# Autonomous Control of DNA

## Tile Self-Assembly with Synthetic

## Oscillator

## 6.1 Introduction

Building on the principle of toehold mediated branch migration [59], dynamic DNA nanotechnology has produced a variety of logic and signal processing circuits [45, 40, 6] and include up to a hundred DNA strands relying on methods that maximize strand interaction specificity and minimize crosstalk. These circuits can sense a variety of environmental triggers [29], and can be powered with enzymatic reactions enabling autonomous complex dynamics such as bistability and oscillations [24, 23, 34, 38].

### 6.1.1 Overview of Logic Circuits and Dynamic Circuits

As described in section 4.1.1, strand displacement is the process by which a DNA complex of two pre-hybridized strands is changed by displaying one strand, and replacing it with a different input strand. It has been shown that DNA based devices and its structure can be actively modulated through toehold-mediated branch migration [62]. Yurke *et al* reported a system where DNA was used as both the machine and fuel, where tweezers were able to switch between two states, open and closed. The alternating system was powered by the hybridization of fuel strands that either opened or closed the tweezers due to branch migration [60]. In 2004, Sherman and Seeman developed a molecular walker constructed of DNA [49]. As in the tweezers device, DNA strands were used as input to release the 'feet' of the walker from the DNA path; also through branch migration.

Further studies were conducted, optimizing the usage of strand displacement for controlling mechanical devices. In order to maintain devices such as the tweezers described above, fuel must be constantly added to the system. To avoid the need of adding an input strand at desired steps, strand-displacement cascades can be used.

Cascading simply uses the output of the resultant branch migration to act as an input further downstream [62]. Cascading can become very useful in many DNA based logic circuits.

Nucleic acid logic circuits can also be designed with enzymatic catalyst. Lu *et al* illustrated how the use of DNazymes could assist in controlling the transformations of nucleic acid based devices [32]. Additionally, DNazymes were described for the use of logic gates. DNazymes with well known catalytic activities, was shown to cleave specific domains of hybridized strands, exposing a sequence used to initiate branch migration of the walker DNA described above [51]. Kim *et al* designed a molecular oscillator using proteins to transcribe DNA cascading strands, used as inputs to either activate, or inhibit further production. RNazymes were also used in the system for degradation catalysts to power dynamic circuits[24].

We will use dynamic circuits containing enzymes to catalyze our system, transcribing RNA strands that will be used as a cascading input of branch migration. The enzymatic activity will provide a delay within our circuit that will allow for one of two states to be active (on or off). These two state will later translate to the dynamics of our tubes (breaking and growing).

## 6.2 Methods and Materials

### 6.2.1 Bulk fluorimetry

Bulk fluorescence experiments were performed using a Horiba Jobin Yvon Fluorlog 3 spectrofluorimeter. Samples were placed in 60 $\mu$ L quartz cuvettes purchased from Starna (#16.45F-Q-3/Z15), and incubated in the sample chamber at 37°C. The desired temperature was maintained using a water bath thermostat. To avoid evaporation, the

sample was covered with 50 $\mu$ L of hexadecane (MP Biomedical, LLC # 0219521880). Fluorescence emission of reporters was measured over three separate experiments and averaged accordingly.

In experiments including the molecular oscillator, excitation/emission for dye TYE665 (strand T21, Table 6.3) were set at 645 nm/665 nm according to the recommendation of the supplier IDT DNA.

In fluorimetry experiments involving TAMRA-labeled 8 base sticky end tiles, excitation/emission for TAMRA was set to 559 nm/583 nm according to the recommendation of the supplier IDT DNA.

### 6.2.2 Bulk fluorimetry data processing

Fluorescence measurements on the oscillator (Section 6.4.1), which track the on/off state of fluorescently labeled synthetic genes over time, were normalized and converted to concentrations using the following general formula:

$$C(t) = C_0 \frac{F(t) - F_{\min}}{F_{\max} - F_{\min}},$$

where  $C(t)$  is the concentration at time sample  $t$ ,  $C_{tot}$  is the (nominal) total concentration of the component being tracked,  $F(t)$  is the recorded fluorescence, and  $F_{\min}$  and  $F_{\max}$  are respectively minimum and maximum fluorescence values corresponding to fully quenched or free labeled strand. For instance,  $F_{\min}$  is the fluorescence of a fully quenched genelet when its quencher-carrying activator is bound to the promoter (active), while  $F_{\max}$  is the fluorescence of the gene when no activator is present (inactive). The ratio  $R = F_{\min}/F_{\max}$  should be independent of specific strand concentration and lamp intensity. However,  $F_{\min}$  and  $F_{\max}$  in some cases were not available simulta-

neously, therefore the normalization above was done as:

$$C(t) = C_{tot} \frac{F(t)/F_{max} - R}{1 - R},$$

and  $R$  was measured in separate experiments off line, from a calibration sample reproducing the buffer mix conditions of the experiment to be normalized. For the oscillator switch SW21, the signal of the reporter dye is directly proportional to the concentration of inactive switch. We therefore further processed the oscillator switch SW21 reporter signal to represent the *active* state of the switch:

$$C_{active}(t) = C_{tot} - C(t).$$

Fluorescence measurements of nanotube invasion and anti-invasion reactions (Section 5.4.1) were normalized using the fluorescence measured in a control sample including only free monomers (partially blunt ended tiles which cannot polymerize) as the maximum achievable fluorescence  $F_{max}$ . Since there could be bleaching of the fluorophore over long periods of time, the average fluorescence value of first one hour in the control sample was assumed as the maximum achievable value. The normalized fluorescence was thus computed as:

$$F_N(t) = F(t) \frac{100}{F_{max}}.$$

### 6.2.3 Transcription

Transcription mix was prepared mixing reagents for the following overall final concentrations: 1x transcription buffer (New England Biolabs, #B9012S), 5.5 mM each rNTP

(Epicentre Biotechnologies, Cat. n. RN02825), 30 mM MgCl<sub>2</sub> and 0.015 U/ $\mu$ l yeast inorganic pyrophosphatase (New England Biolabs, #M2403L).

T7 RNAP was purchased from Cellscript (200 U/ $\mu$ l, # C-T7300K). *E. coli* cloned RNase H was purchased from Ambion, Cat. n. AM2292 (10 U/ $\mu$ l).

#### 6.2.4 DNA Sequences

<i>Name</i>	<i>Tile with 8-base sticky ends</i>
8b S1	5'- AGT GGA CAG CCG TTC TGG AGC GTT GGA CGA AAC T
8b S2	5'- <b>TGT AAT ATC</b> GTG CCC GAG CAC CAC TGA GAG GTA
8b S3	5'-T Cy3/CCA GAA CGG CTG TGG CTA AAC AGT AAC CGA AGC ACC AAC GCT
8b S4	5'- GGG CAC GAA GTT TCG TGG TCA TCG TAC CTC TC
8b S5	5'- CGA TGA CCT GCT TCG GTT ACT GTT TAG CCT GCT C
8b Invader	5'- GGG CAC GAT ATT ACA CTA AGG
8B Anti-Invader	5'- CCT TAG TGT AAT ATC GTG CCC

Table 6.1: Sequences for tiles with 8-base long sticky ends, invaders and anti-invaders. Bold sequences indicate toehold domains. Strand interactions are shown in Fig. 5.1 B, 5.2 B, 5.3 B, and 5.4 B.

<i>Name</i>	<i>Insulator system producing invader for 8-base sticky end tile</i>
8b Ins-nt	5'- CAT TAG TGT CGT TCG TTC ACA GTA ATA CGA CTC ACT ATA GGG CAC GAT ATT ACA CTA AGG AGT GAC AAA GTC ACA AA
8b Ins-t	5'- TTT GTG ACT TTG TCA CTC CTT AGT GTA ATA TCG TGC CCT ATA GTG AGT CG
RNA invader	GGG CAC GAU AUU ACA CUA AGG <u>AGU GAC AAA GUC ACA AA</u>
dI1	5'-GTG TGT AGT AGT AGT TCA TTA GTG TCG TTC GTT CAC AG
A1	5'-TAT TAC TGT GAA CGA ACG ACA CTA ATG AAC TAC TAC

Table 6.2: DNA sequences for the insulator gene used to couple oscillator and nanotubes, together with its activator and inhibitor (which are the same as for switch 21 of the oscillator). The genelet includes a 3' end hairpin sequence to reduce transcription elongation; thus, the RNA invader includes a hairpin sequence (underlined). Fig. 5.6 shows the interactions among insulator components (activation and inhibition), production of RNA invader, invasion of tiles and RNase H-mediated reactivation of tiles.

<i>Name</i>	<i>Oscillator</i>
T12-t	5'- TTT CTG ACT TTG TCA GTA TTA GTG TGT AGT AGT AGT TCA TTA GTG TCG TTC GTT CTT TGT TTC TCC CTA TAG TGA GTC G
T12-nt	5'-AAG CAA GGG TAA GAT GGA ATG ATA ATA CGA CTC ACT ATA GGG AGA AAC AAA GAA CGA ACG ACA CTA ATG AAC TAC TAC TAC ACA CTA ATA CTG ACA AAG TCA GAA A
T21-t	5'-TTT CTG ACT TTG TCA GTA TTA TCA TTC CAT CTT ACC CTT GCT TCA ATC CGT TTT ACT CTC CCT ATA GTG AGT CG
T21-nt	5'-Tye665/CAT TAG TGT CGT TCG TTC ACA GTA ATA CGA CTC ACT ATA GGG AGA GTA AAA CGG ATT GAA GCA AGG GTA AGA TGG AAT GAT AAT ACT GAC AAA GTC AGA AA
dI1	5'-GTG TGT AGT AGT AGT TCA TTA GTG TCG TTC GTT CAC AG
A1	5'-TAT TAC TGT GAA CGA ACG ACA CTA ATG AAC TAC TAC
A2	5'-TAT TAT CAT TCC ATC TTA CCC TTG CTT CAA TCC GT

Table 6.3: DNA sequences for oscillator used to control the growth and decay of DNA nanotubes. Sequences are taken from [23, 16]. Gene sequences include a 3' end hairpin domain to reduce transcription elongation. Target strand interactions are shown in Fig. 6.2 and 6.3; a schematic of the oscillator reactions is shown in Fig. 6.1.

## 6.3 Reaction Schemes

### 6.3.1 Reactions designed to direct tube breakage and reassembly using an autonomous molecular oscillator

For the readers' convenience we report detailed strand interactions for the oscillator system used to direct nanotube assembly and disassembly; figures 6.1, 6.2 and 6.3 are adapted from [23, 16, 52]. Fig. 6.4 summarizes the architecture used to interconnect the oscillator and the nanotubes, which builds on results obtained in [16]. This is done using an insulating gene, which decouples the sequences of the insulator and the sequence of the RNA invader, and additionally reduces consumption of oscillator components (RNA transcription works as an amplification mechanism). This architecture, however, cannot mitigate consumption of RNase H, which degrades RNA invader bound to the tiles, creating an additional load on the oscillator system. To compensate for this consumption, the oscillator was tuned in a regime where RNase H is abundant; this topic is discussed further in Section 6.4.1.

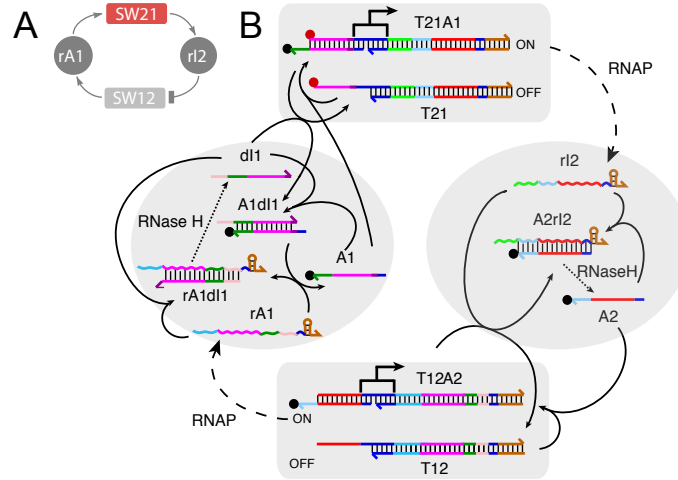


Figure 6.1: **Topology of the oscillator and its biochemical reactions.** A: Topology of the synthetic molecular oscillator used in our experiments: two artificial genetic switches (SW12 and SW21) are mutually interconnected through their RNA transcripts (rA1 and rI2) forming a negative feedback loop. B: Reactions occurring in the system. Functionally distinct domains (toeholds, regulatory domains, spacers, promoter and hairpin regions) are colored consistently with strand schematics in Figs. 6.2 and 6.3. Red and black dots on gene T21 and activator A1 are fluorophore-quencher pairs used as reporters on the active/inactive state of the switch. Solid arrows indicate reactions between oligonucleotides; dashed arrows indicate enzymatic reactions (transcription and degradation). Figure is adapted from [23, 16, 52].

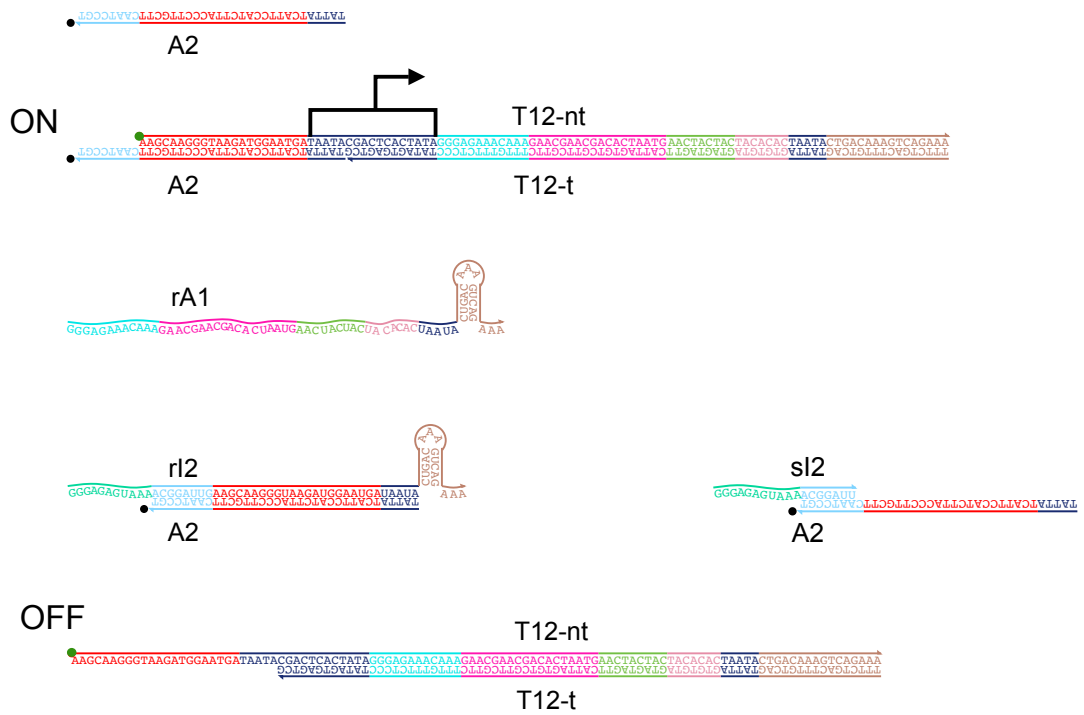


Figure 6.2: **Switch 12 strands and their domain interactions.** This figure shows strands components of SW12 and their interactions, with functional domains in different colors. The mathematical model of the oscillator includes all complexes shown in this figure, including complex sI2·A2 which is the result of interactions between A2 and products of incomplete degradation of RNase H which can reach up to 7 bases [59, 41].

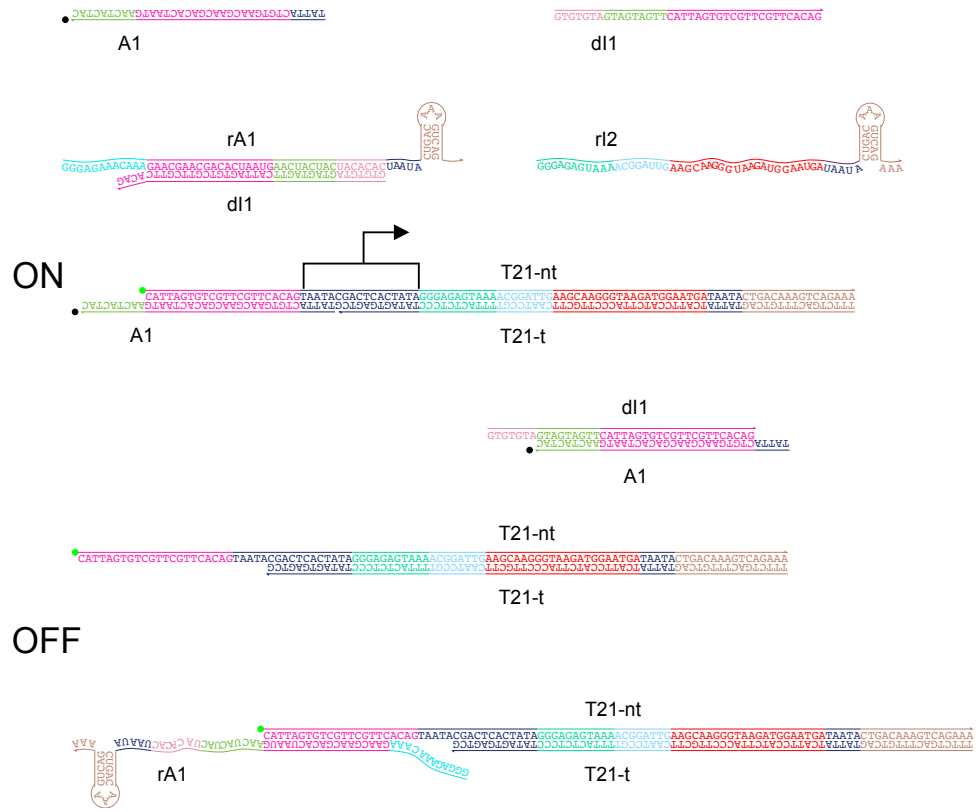


Figure 6.3: **Switch 21 strands and their domain interactions.** As Fig. 6.2, we show sequences for SW21 with functional domains in different colors. The mathematical model of the oscillator includes all complexes shown in this figure.

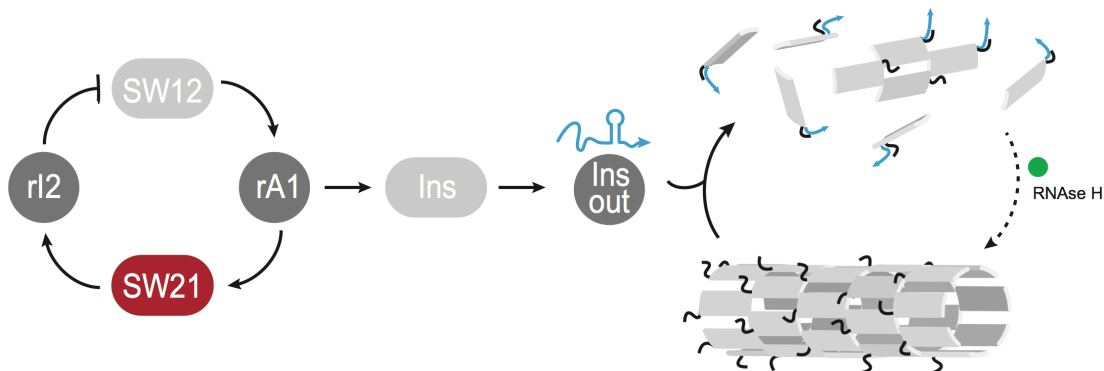


Figure 6.4: **The oscillator was used to direct nanotube assembly and disassembly using an insulator gene.** This scheme summarizes the topology of interconnection of the oscillator and the nanotubes. The insulator gene (Fig. 5.6) was designed to be activated and inactivated by strands A1 and dI1 of the oscillator, and its transcript is an RNA invader. Tile reactivation is promoted by RNase H degradation. Strands and reactions for the transcriptional insulator, invasion, and RNase H anti-invasion are shown in Fig. 5.6.

## 6.4 Results and Discussion

### 6.4.1 Directing nanotube disassembly and reassembly using a synthetic transcriptional oscillator

The oscillator was tuned to operate in a regime of high RNase H concentration, because RNase H is needed to promote nanotube regrowth by degrading RNA invader bound to the tiles. Obtaining large amplitude oscillations in this regime requires an increase in RNAP concentration [44]. Amplitude is defined as the peak-well difference in T21 fluorescence, corresponding to the on-off state of switch S21; this amplitude is directly proportional to the on-off ratio of the insulator as well, which has the same activation/inhibition domains of T21. Activity of genelet T21 was tracked by labeling T21 non-template strand with TYE665, and A1 with Iowa Black quencher as done in previous reports [23, 16]. Fluorescence of T21 was tracked analyzed using Horiba Jobin

Yvon Fluorolog 3 system as described in Section 6.2.1. Nanotube length distributions were assessed by imaging samples from the bulk solution with a fluorescence microscope (see Section 3.2.2); samples were taken at time stamps specified in each figure.

Amplitude and frequency in this molecular oscillator cannot be independently tuned [44]: large amplitude correlates with a large (slow) oscillation period. In addition, there is significant variability in the achievable oscillator behavior depending on the lot of RNAP and RNase H. As a result of these two challenges, our experiments focus on only two operating points: in the first we obtained a single, slow oscillation with large amplitude followed by a slow drift to a steady state; in the second, we tuned the circuit to exhibit two faster oscillations. In all our experiments, we used RNAP from a single lot (Rp-Lot 1), and RNase H from two different lots (Rh-Lot 1 and Rh-Lot 2).

Oscillator sequences were premixed in a DNA stock solution containing: 1x transcription buffer, 20 mM rNTPs, 14 mM MgCl<sub>2</sub>, and annealed 8 base sticky end nanotubes. To control nanotube assembly and disassembly via oscillator inputs and outputs, RNA invader genelet activated by oscillator strand A1 was added to the solution.

**Single-oscillation experiments** These experiment were done using a single lot of RNAP and RNase H. The final concentrations of the oscillator strands were: T12 120 nM; T21 250 nM; dI1 600 nM, A1: 250 nM in the absence of insulator, 320 nM in the presence of insulator; A2 600 nM; insulator template (when present) 65 nM. T7 RNAP 10% (v/v), PPase 3% (v/v), and RNase H 2% (v/v) (Rh-Lot 1).

**Double-oscillation experiments** **Single-oscillation experiments** These experiment were done using a single lot of RNAP (Rp-Lot 1) and RNase H (Rh-Lot 1). The final concentrations of the oscillator strands were: T12 120 nM; T21 250 nM; dI1 700 nM, A1: 250 nM in the absence of insulator, this concentration was adjusted

to 250+X nM in the presence of X nM insulator template; A2 600 nM; the insulator template concentration was varied as specified in each experiment below. T7 RNAP 10% (v/v) (Rp-Lot 1), PPase 2.6% (v/v), and RNase H 2.75% (v/v) (Rh-Lot 2).

## Control experiment: oscillator and nanotubes in the absence of of insulator

This experiment was conducted using experimental conditions defined in the single-oscillation operating point, in the absence of insulator template.

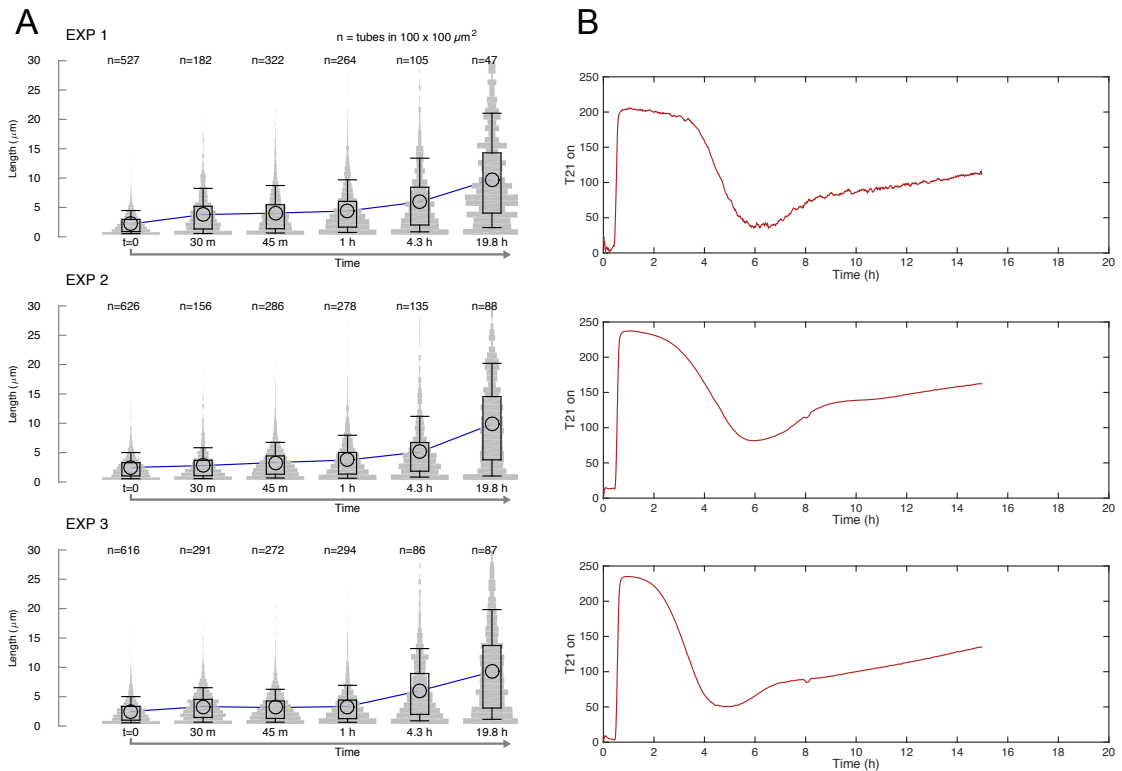


Figure 6.5: **Oscillator and nanotubes in the absence of insulator gene.** Nanotubes at  $1 \mu\text{M}$  tile concentration were incubated in the same sample as the oscillator reaction, in the absence of insulator gene (which directs co-transcriptional invasion by producing an RNA invader). In these conditions, the nanotube mean length increases over time excidding that measured in control experiments (Fig. 5.14). Left: Violin plots of nanotube length distributions. Right: Corresponding normalized oscillator traces (fraction of active T21).

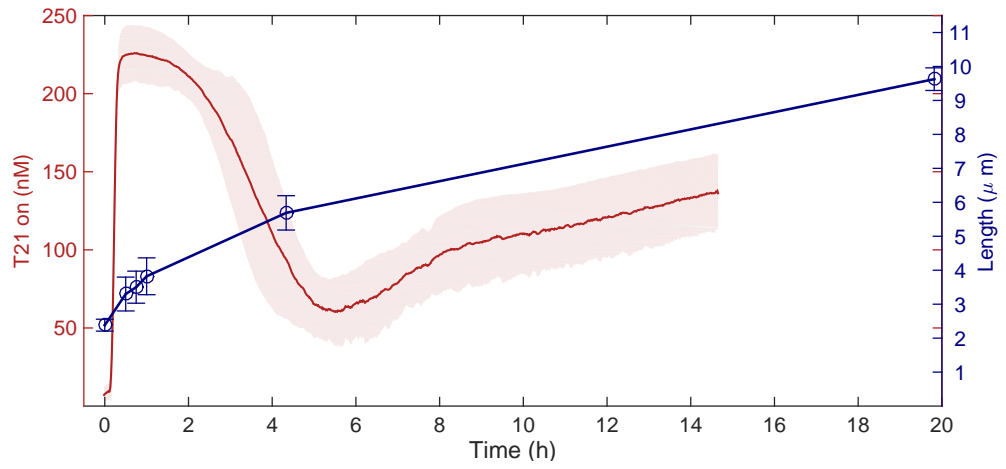


Figure 6.6: **Mean nanotube length and averaged oscillator behavior.** We computed and overlapped the mean and standard deviation of nanotube length and active T21 concentration from Fig. 6.5.

## Oscillator directing nanotubes: 750 nM tile concentration

This experiment was conducted using the single-oscillation operating point conditions.

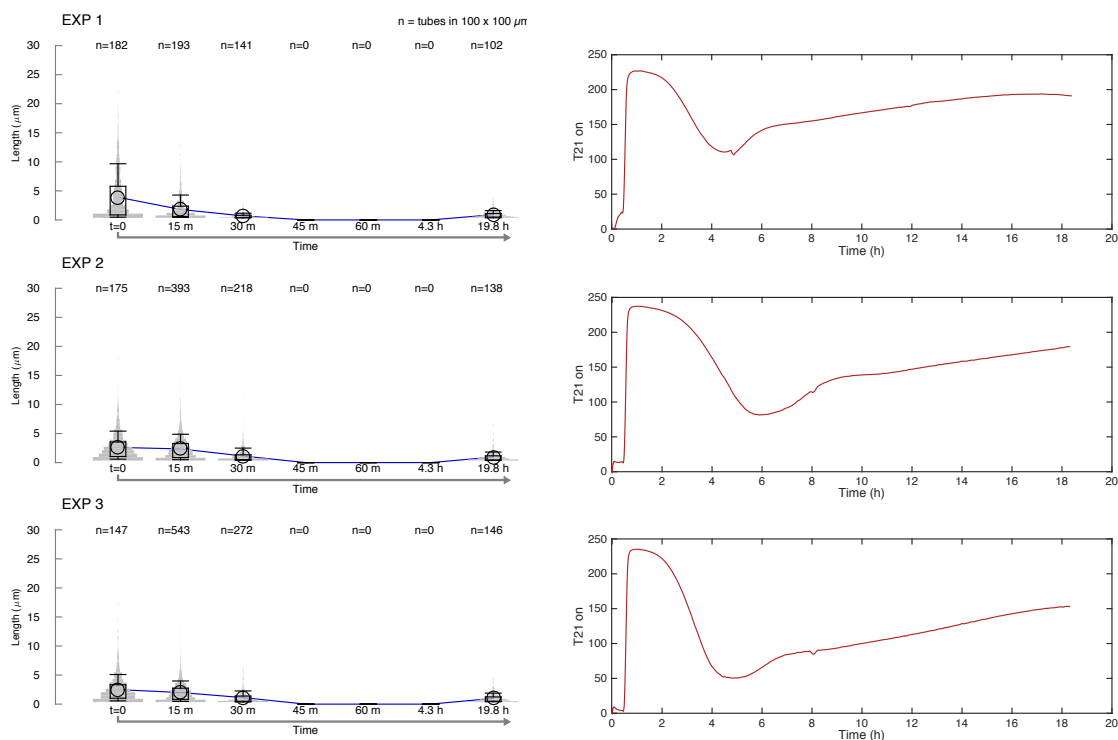


Figure 6.7: **Nanotube growth directed by the oscillator circuit; 750 nM total tile concentration.** Nanotubes annealed from a total concentration of 750 nM tiles were incubated in the same sample as the oscillator reaction in the presence of insulator gene (which directs co-transcriptional invasion by producing an RNA invader). In these low-monomer concentration conditions, nanotubes quickly break after starting the reactions yet regrowth (mediated by RNase H) is suppressed presumably due to the low monomer concentration. Left: Violin plots of nanotube length distributions. Right: Normalized oscillator traces (fraction of active T21).

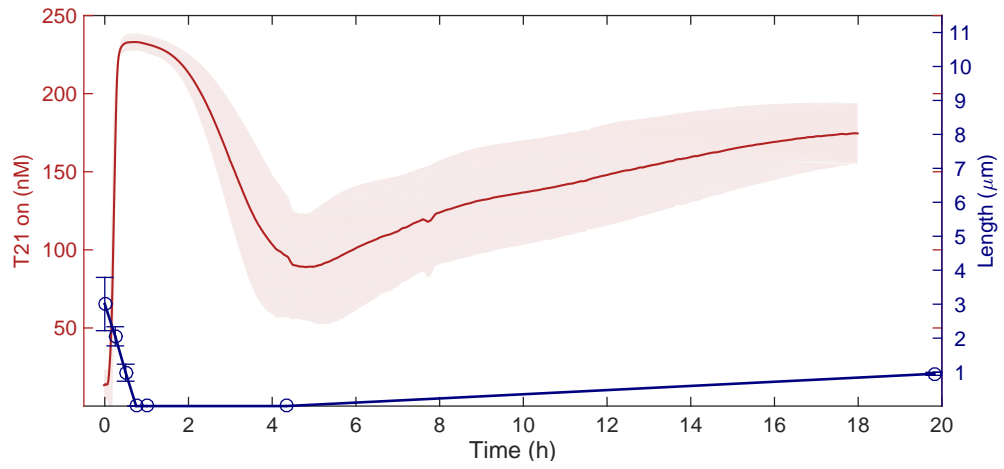


Figure 6.8: **Mean nanotube length and averaged oscillator behavior; 750 nM total tile concentration.** We computed and overlapped the mean and standard deviation of nanotube length and active T21 concentration from Fig. 6.7.

## Oscillator directing nanotubes: 1000 nM tile concentration

This experiment was conducted using experimental conditions defined in the single-oscillation operating point.

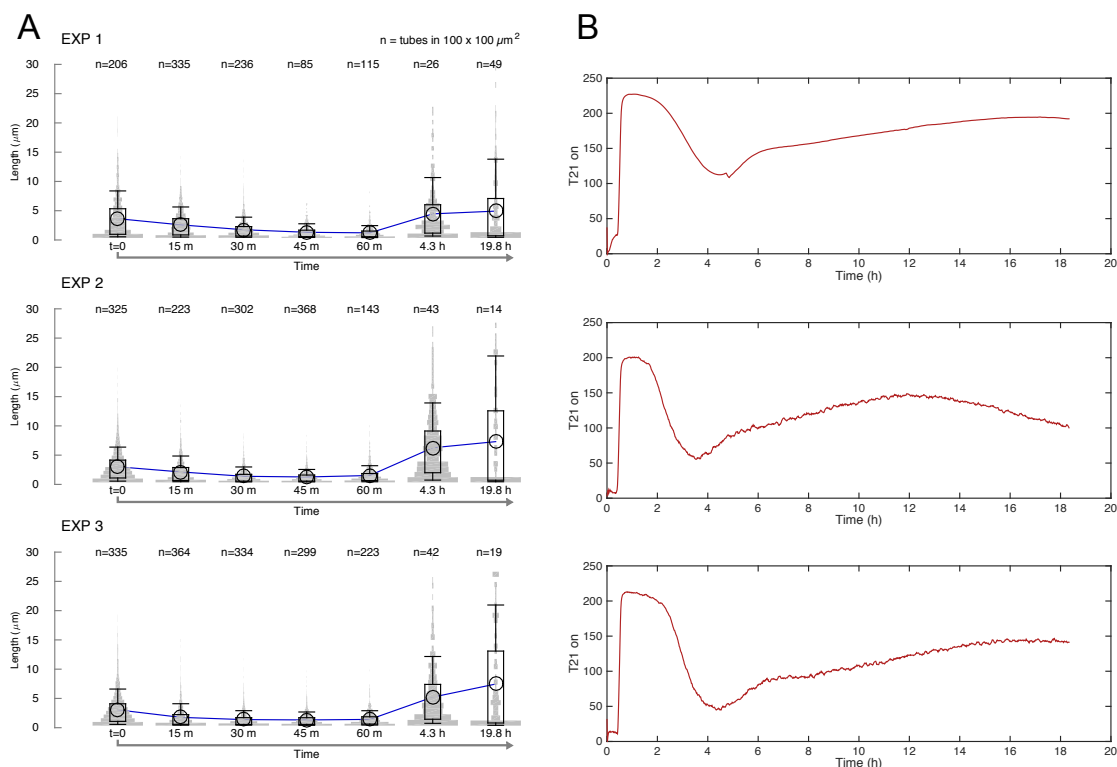


Figure 6.9: **Nanotube growth directed by the oscillator circuit; 1000 nM total tile concentration.** Nanotubes annealed from a total concentration of 1000 nM tiles were incubated in the same sample as the oscillator reaction in the presence of insulator gene (which directs co-transcriptional invasion by producing an RNA invader). Nanotubes break after starting the oscillator reaction by adding enzymes when the insulator is active. When T21 turns off, the insulator activity is also reduced; this means that RNase H degradation dominates over production of invader, and nanotube regrowth is promoted. Left: Violin plots of nanotube length distributions. Right: Corresponding normalized oscillator traces (fraction of active T21).

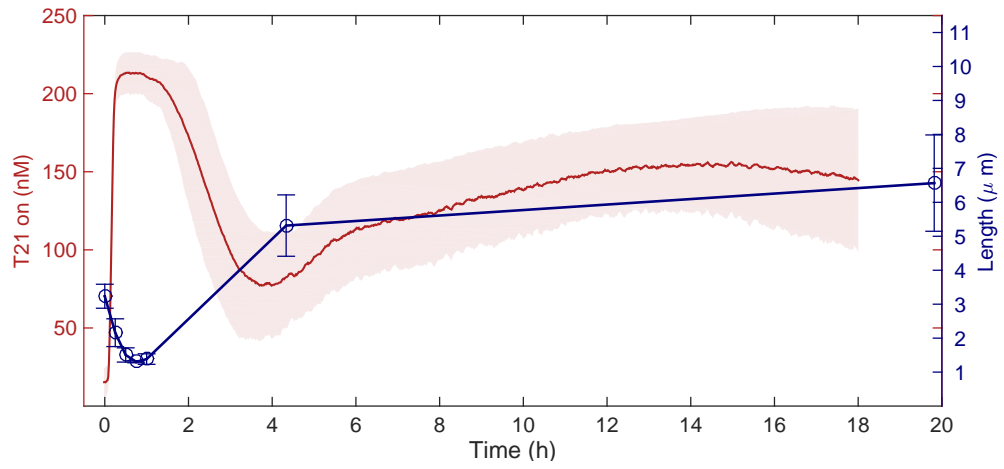
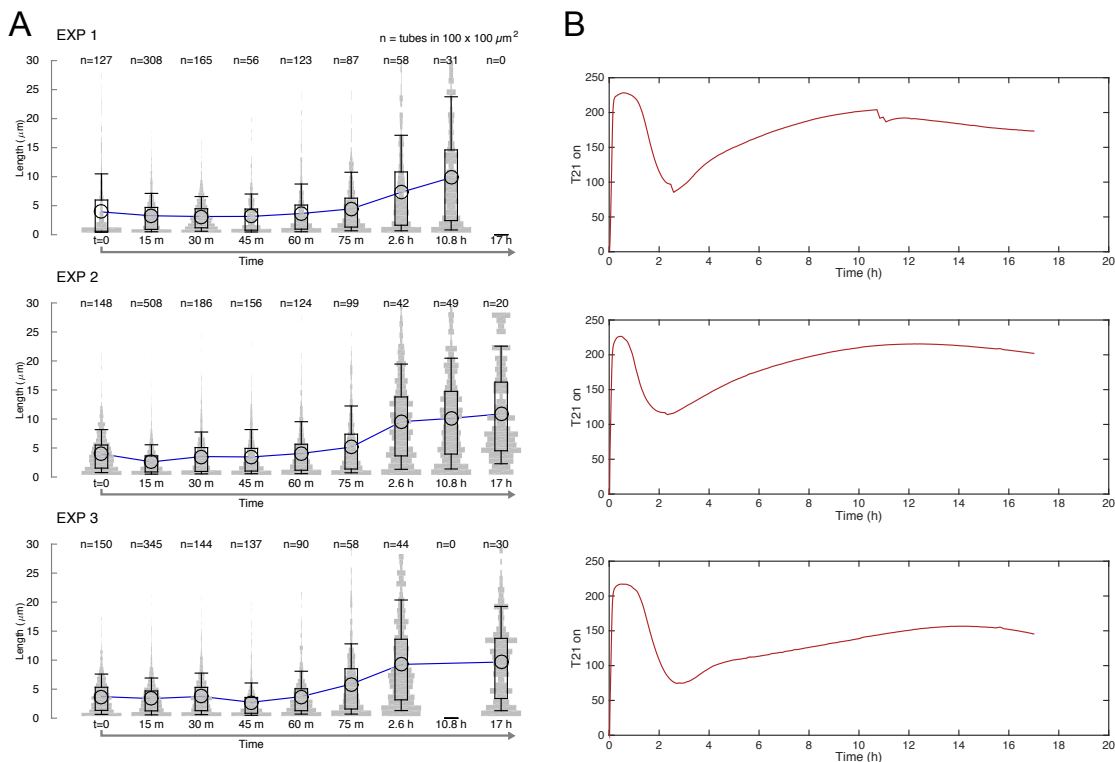


Figure 6.10: **Mean nanotube length and averaged oscillator behavior; 1000 nM total tile concentration.** We computed and overlapped the mean and standard deviation of nanotube length and active T21 concentration as a function of time from Fig. 6.9.

## Oscillator directing nanotubes: 1500 nM tile concentration

This experiment was conducted using the single-oscillation operating point conditions.



**Figure 6.11: Nanotube growth directed by the oscillator circuit; 1500 nM total tile concentration.** Nanotubes annealed from a total concentration of 1500 nM tiles were incubated in the same sample as the oscillator reaction in the presence of insulator gene (which directs co-transcriptional invasion by producing an RNA invader). After the oscillator reaction starts (addition of enzymes) the insulator is active, yet breakage is not effective presumably due to the high concentration of tiles, but growth is halted until T21 begins to be turned off. When T21 turns off, the insulator activity is also reduced, and less invader is produced. RNase H degradation dominates over production of invader, and facilitates rapid growth of nanotubes. Left: Violin plots of nanotube length distributions. Right: Corresponding normalized oscillator traces (fraction of active T21).

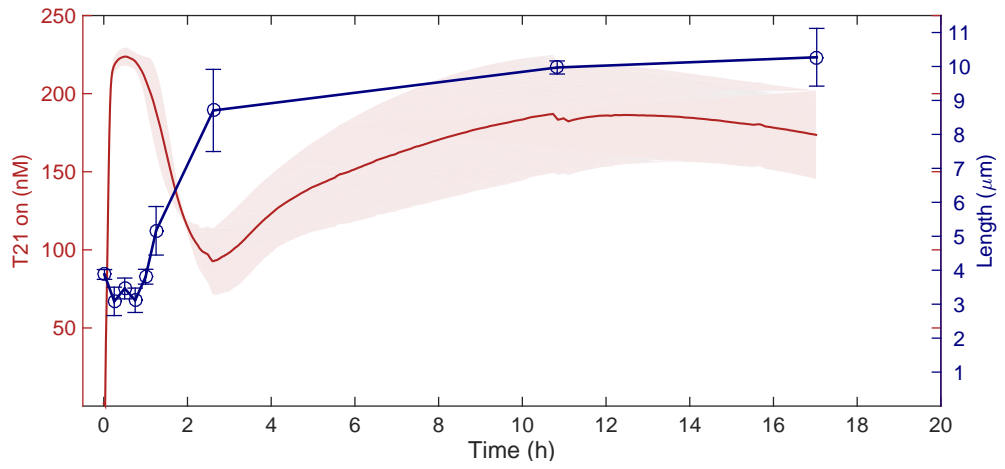


Figure 6.12: **Mean nanotube length and averaged oscillator behavior; 1500 nM total tile concentration.** We computed and overlapped the mean and standard deviation of nanotube length and active T21 concentration as a function of time from Fig. 6.11.

### Oscillator directing nanotubes: 1000 nM tile concentration, 70 nM insulator

This experiment was conducted using experimental conditions defined in the double-oscillation operating point.

We report only violin plots and individual oscillator traces. The mean and standard deviation of nanotube length and active T21 concentration as a function of time are plotted in Fig. 6.14 below.

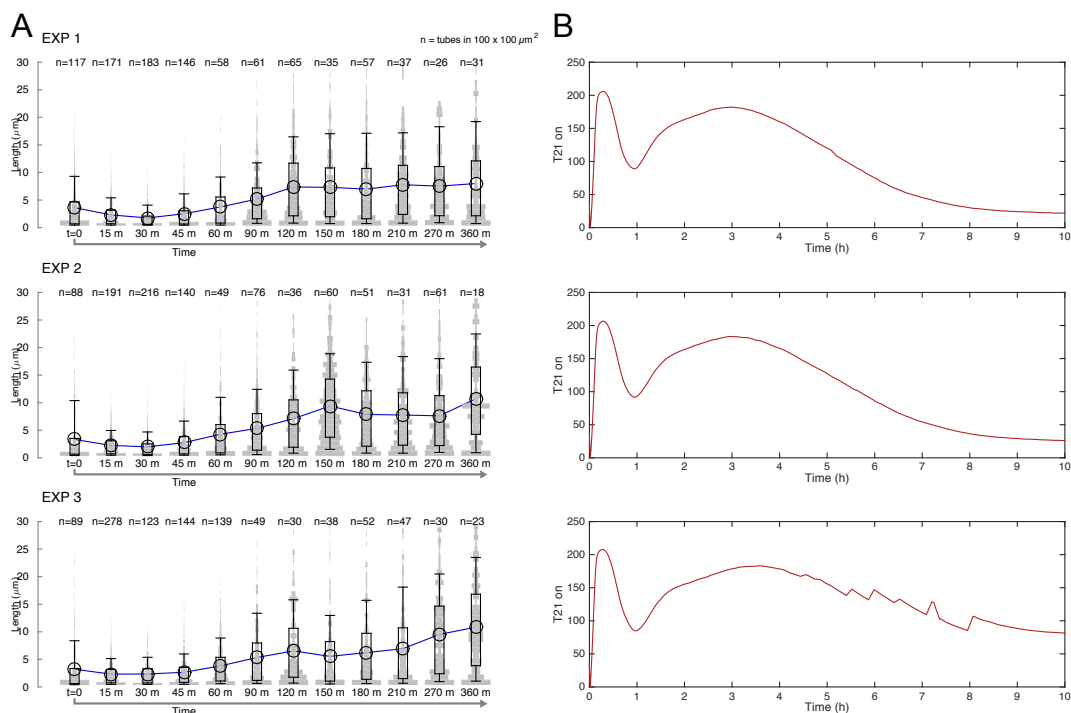


Figure 6.13: **Nanotube growth directed by the oscillator circuit; 1000 nM tile concentration, 70 nM insulator.** Nanotubes annealed from a total concentration of 1000 nM tiles were incubated in the same sample as the oscillator reaction in the presence of 70 nM insulator gene (which directs co-transcriptional invasion by producing an RNA invader). Left: Violin plots of nanotube length distributions. Right: Corresponding normalized oscillator traces (fraction of active T21).

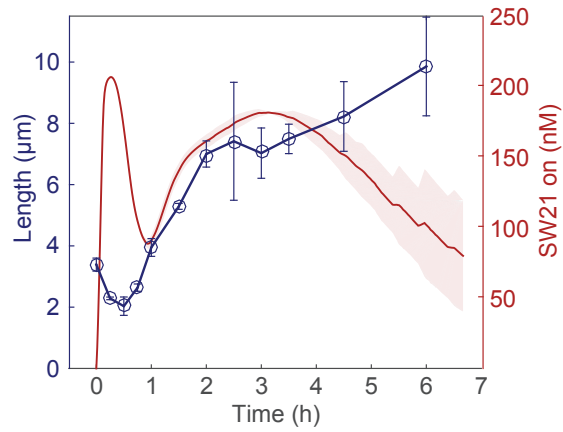


Figure 6.14: **Nanotube growth directed by the oscillator circuit; 1000 nM tile concentration, 70 nM insulator** Triplicate experiments testing the two-oscillation operating point in the presence of insulator at 70 nM, which confirm that as the fraction of SW21 increases (and so does the invader concentration), there is a decrease in mean nanotube length.

## Oscillator directing nanotubes: 1000 nM tile concentration, 100 nM insulator

This experiment was conducted using experimental conditions defined in the double-oscillation operating point.

Here we report violin plots and individual oscillator traces. The mean and standard deviation of nanotube length and active T21 concentration as a function of time are plotted in Fig. 6.16 below.

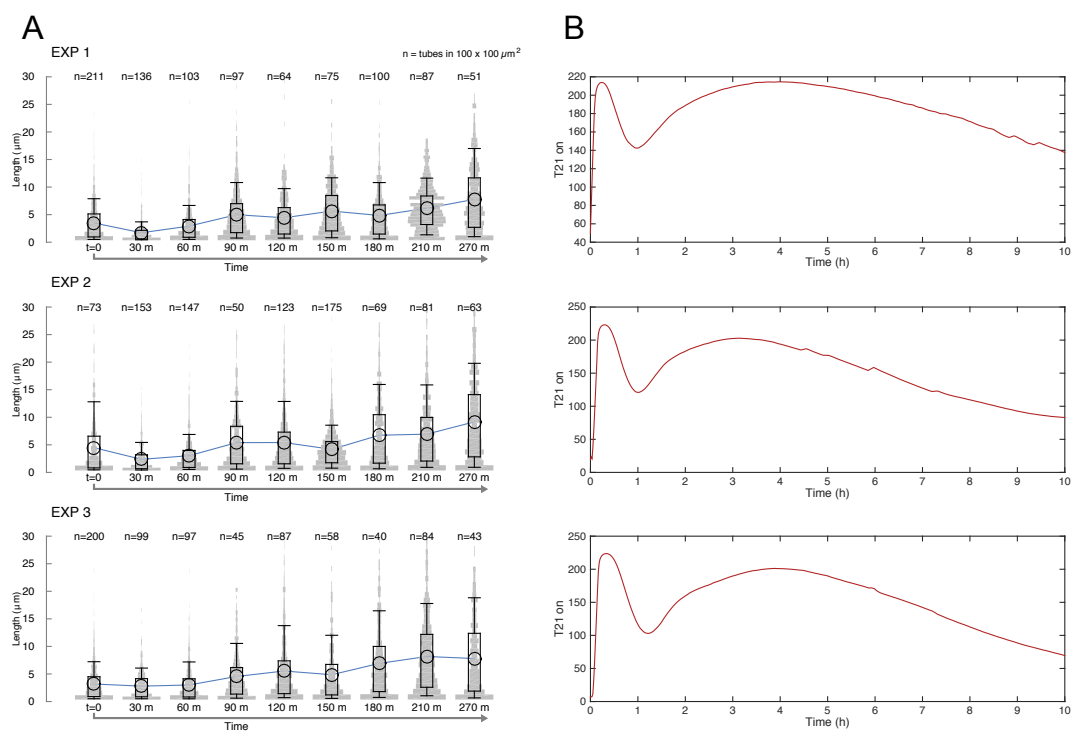


Figure 6.15: **Nanotube growth directed by the oscillator circuit; 1000 nM tile concentration, 100 nM insulator.** Nanotubes annealed from a total concentration of 1000 nM tiles were incubated in the same sample as the oscillator reaction in the presence of 100 nM insulator gene (which directs co-transcriptional invasion by producing an RNA invader). Left: Violin plots of nanotube length distributions. Right: Corresponding normalized oscillator traces (fraction of active T21).

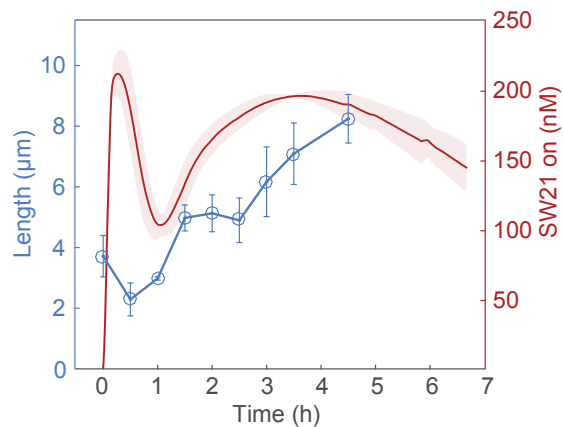


Figure 6.16: **Nanotube growth directed by the oscillator circuit; 1000 nM tile concentration, 100 nM insulator.** Triplicate experiments testing the two-oscillation operating point in the presence of insulator at 100 nM (right), which confirm that as the fraction of SW21 increases (and so does the invader concentration), there is a decrease in mean nanotube length.

## Oscillator directing nanotubes: 1000 nM tile concentration, insulator titration

This experiment was conducted using experimental conditions defined in the double-oscillation operating point.

Here we report violin plots and individual oscillator traces. The mean and standard deviation of nanotube length and active T21 concentration as a function of time are plotted in Fig. 6.18 below.

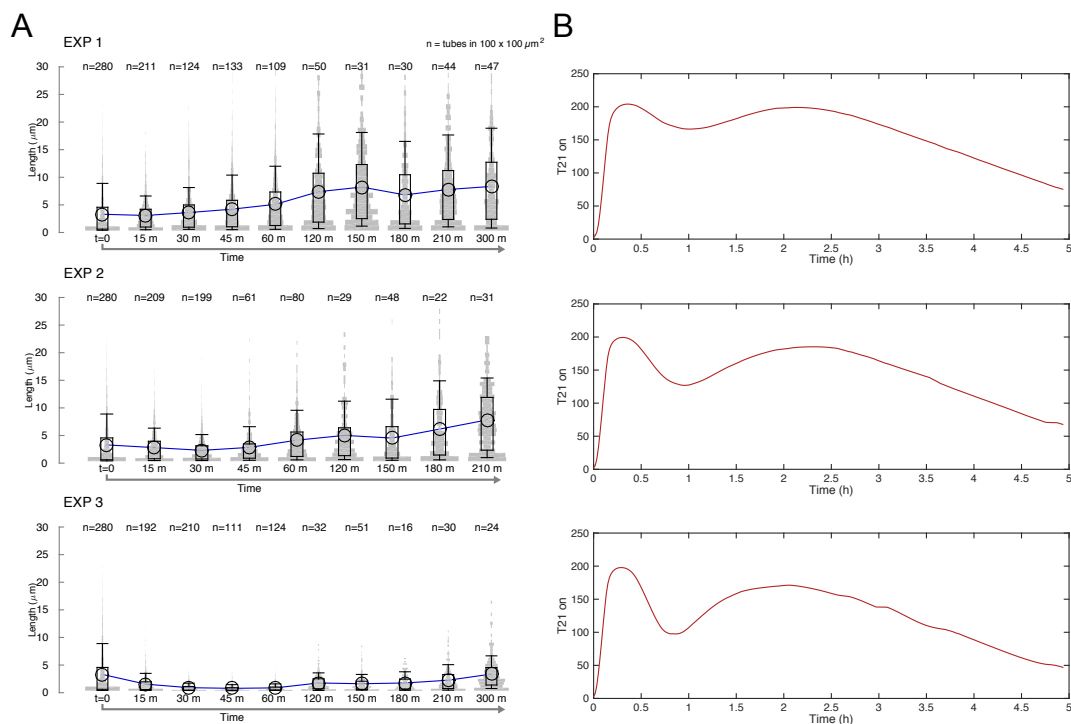


Figure 6.17: **Nanotube growth directed by the oscillator circuit; 1000 nM tile concentration, varying concentration of insulator.** Nanotubes annealed from a total concentration of 1000 nM tiles were incubated in the same sample as the oscillator reaction in the presence of different amounts of insulator gene (which directs co-transcriptional invasion by producing an RNA invader); insulator concentration from top to bottom row is: 150 nM, 100 nM and 50 nM. Left: Violin plots of nanotube length distributions. Right: Corresponding normalized oscillator traces (fraction of active T21).

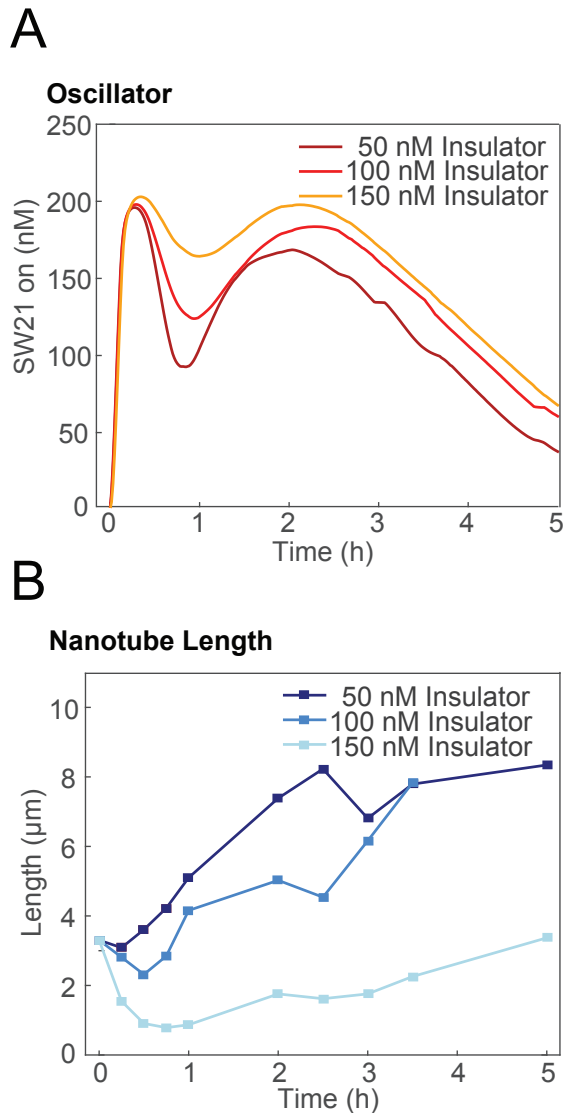


Figure 6.18: **Nanotube growth directed by the oscillator circuit; 1000 nM tile concentration, varying concentration of insulator.** We tuned the transcriptional oscillator to exhibit two oscillations. At this operating point, keeping the tile concentration fixed at  $1 \mu\text{M}$  tiles, we titrated the concentration of insulator genelet concentrations 50 nM, 100 nM, and 150 nM. Increasing insulator concentration causes oscillator amplitude to decrease (A) and nanotube mean length to decrease on average (B). At 100 nM insulator, the mean length decreases at two distinct points in time when the fraction of SW21 increases.

## 6.5 Concluding Remarks

Our results show we were able to successfully couple double crossover tile based nanotubes to synthetic oscillator circuit. By varying enzyme volume ratio (enzyme activity)

of T7 RNAP and RNase H in solution, we tuned oscillator to have either one or two complete cycles. In turn, the tuning of the oscillator behavior was reflected in the number of break-grow cycles nanotubes experienced. We were also able to control the performance of dynamic nanotube breakage and regrowth by either varying coupled tile concentration, or insulator concentration.

## **Chapter 7**

## **Conclusion**

Our work has demonstrated that the self-assembly of micron sized DNA nanostructures can be dynamically and reversibly controlled in a programmable manner using Watson-Crick based interaction of nucleic acid strands. By designing monomer components that have self-assembling ability, we can integrate a level of complexity by individually activating and deactivating components with various DNA strands acting as inputs. We demonstrate this concept by introducing accessible breakage points, or overhand toehold domains, to existing DNA double crossover tiles which form nanotubes isothermally. Through toehold mediated strand displacements, our nanotube structures are therefore controllable by other DNA or RNA input strands. We show that nanotube disassembly can be achieved by designing inter-tile bond invading strands, and assembly can be restored by displacement and titration of invaders by complementary anti-invader molecule. Invader and anti-invader inputs could be released by a variety of DNA networks or molecular processes. In this work, we focus on transcriptional networks and show that an artificial transcriptional oscillator can be used to direct DNA nanotube assembly. We take advantage of enzymes fueling transcriptional networks to produce RNA invaders and to degrade tile-bound invaders to restore polymerization.

Earlier demonstrations of DNA nanostructure control using strand displacement have focused on contraction/relaxation of lattices [15, 1], modulation of relative position of nanostructured components having limited size [18], and triggering growth [65] of tile-based structures. The transcriptional oscillator used in our experiments has been used to direct motion of DNA tweezers, one of the simplest molecular machines [16].

## 7.1 Lessons Learned

Coupling a nonlinear dynamical system with downstream pathways is quite challenging. We found that calibration of the circuit components that are depleted by processes simultaneously present in solution is necessary due to resource limitations (RNAP, RNase H). Insulation can mitigate this problem in cases where it is possible to sense and amplify the concentration of a critical component. In nature, there is constant replenishment of components through gradient reactions. For example, cells are not closed systems. Membranes allow transport of molecules sometimes between phospholipids in cases of osmosis, or through transport channels by way of proteins. Therefore, there is a constant turnover of components that maintains a desired state. In a closed system, such as the case of our couple nanotubes to synthetic oscillator, where components are fixed, there arise a problem of the accumulation of unwanted/degraded products which could in turn slow down and perturb the oscillator kinetics.

## 7.2 Outlook

What larger, more complex systems can we build with the current tools available?

Figure 7.1 illustrates the overall goal of developing responsive nucleic acid biomaterials. Like in nature, our synthetic self assembling materials can react to upstream signals processed through a cascade network of reactions (similar to the described oscillator in our work). In our study, we have focused on the coupling of dynamic circuits to self-assembling components, all composed of similar nucleic acid material.

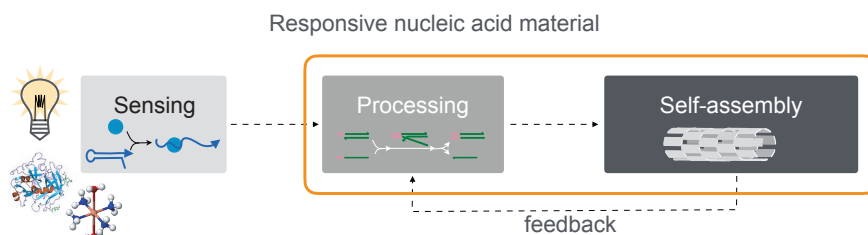


Figure 7.1: **Responsive nucleic acid biomaterials could be built by modularly interconnecting sensing, processing, and self-assembling components** Nucleic acids nanotechnology has an expandable toolkit of sensing devices such as aptamers and ribozymes [3], as well as logic and dynamic signal processing devices [62], and nanostructures [66]. These components can be engineered to operate together modularly as a responsive material with programmable behaviors, and could potentially exploit feedback for self-regulation. As a proof of principle, in this paper we demonstrate that it is possible to use complex nucleic acid circuits to direct self-assembly of tubular DNA nanostructures (orange box).

There are many available methods of sensing and detecting biological and chemical components and species [7, 21, 28]. Integration of sensors for processing environmental stimuli could yield responsive structures to stimuli. For example, such stimulants could include pH, light, biochemical signals, and temperature. With our proposed architecture being compatible with most DNA tiles [56, 27], we may be able to implement such concepts for large dynamic structures which could be functionalized to get responsive DNA scaffolds [48, 30] or origami (monodisperse). Similar architecture to what we propose could also be used to elicit active responses in more complex materials organized by DNA such as nanoparticles [37] and droplets [19]. Ultimately, cellular sensors and signal processing modules could be transduced into RNA signals to direct artificial nanostructures inside cells to create artificial organelles or localizing scaffolds, alternative to the cytoskeleton. These are all potential concepts stemming from our research findings that can be implemented in future research to come.

# References

- [1] F. A. Aldaye and H. F. Sleiman. Dynamic DNA templates for discrete gold nanoparticle assemblies: control of geometry, modularity, write/erase and structural switching. *Journal of the American Chemical Society*, 129(14):4130–4131, 2007.
- [2] E. Benson, A. Mohammed, J. Gardell, S. Masich, E. Czeizler, P. Orponen, and B. Högberg. DNA rendering of polyhedral meshes at the nanoscale. *Nature*, 523(7561):441–444, 2015.
- [3] M. Blind and M. Blank. Aptamer selection technology and recent advances. *Molecular TherapyNucleic Acids*, 4(1):e223, 2015.
- [4] R. F. Bruinsma, W. M. Gelbart, D. Reguera, J. Rudnick, and R. Zandi. Viral self-assembly as a thermodynamic process. *Physical review letters*, 90(24):248101, 2003.
- [5] J. Chen and N. C. Seeman. Synthesis from dna of a molecule with the connectivity of a cube. *Nature*, 350(6319):631–633, 1991.
- [6] Y.-J. Chen, N. Dalchau, N. Srinivas, A. Phillips, L. Cardelli, D. Soloveichik, and G. Seelig. Programmable chemical controllers made from DNA. *Nature nanotechnology*, 8(10):755–762, 2013.
- [7] Y. Cui, Q. Wei, H. Park, and C. M. Lieber. Nanowire nanosensors for highly sensitive and selective detection of biological and chemical species. *Science*, 293(5533):1289–1292, 2001.
- [8] E. W. Dent and K. Kalil. Axon branching requires interactions between dynamic microtubules and actin filaments. *The Journal of Neuroscience*, 21(24):9757–9769, 2001.
- [9] D. Doty. Theory of algorithmic self-assembly. *Communications of the ACM*, 55(12):78–88, 2012.
- [10] S. M. Douglas, H. Dietz, T. Liedl, B. Högberg, F. Graf, and W. M. Shih. Self-assembly of DNA into nanoscale three-dimensional shapes. *Nature*, 459(7245):414–418, 2009.
- [11] S. M. Douglas, A. H. Marblestone, S. Teerapittayanon, A. Vazquez, G. M. Church, and W. M. Shih. Rapid prototyping of 3d DNA-origami shapes with caDNAo. *Nucleic acids research*, page gkp436, 2009.
- [12] G. L. Eichhorn and Y. A. Shin. Interaction of metal ions with polynucleotides and related compounds. xii. the relative effect of various metal ions on DNA helicity. *Journal of the American Chemical Society*, 90(26):7323–7328, 1968.

- [13] A. Ekani-Nkodo, A. Kumar, and D. K. Fygenson. Joining and scission in the self-assembly of nanotubes from DNA tiles. *Physical review letters*, 93(26):268301, 2004.
- [14] A. D. Ellington and J. W. Szostak. In vitro selection of rna molecules that bind specific ligands. *Nature*, 346(6287):818–822, 1990.
- [15] L. Feng, S. H. Park, J. H. Reif, and H. Yan. A two-state DNA lattice switched by DNA nanoactuator. *Angewandte Chemie International Edition*, (42):4342–4346, 2003.
- [16] E. Franco, E. Friedrichs, J. Kim, R. Jungmann, R. Murray, E. Winfree, and F. C. Simmel. Timing molecular motion and production with a synthetic transcriptional clock. *Proceedings of the National Academy of Sciences*, 108(40):E784–E793, 2011.
- [17] T. Fu and N. Seeman. DNA double-crossover molecules. *Biochemistry*, 32(13):3211–3220, 1993.
- [18] T. Gerling, K. F. Wagenbauer, A. M. Neuner, and H. Dietz. Dynamic DNA devices and assemblies formed by shape-complementary, non–base pairing 3D components. *Science*, 347(6229):1446–1452, 2015.
- [19] M. Hadorn, E. Boenzli, K. T. Sørensen, H. Fellermann, P. E. Hotz, and M. M. Hanczyc. Specific and reversible DNA-directed self-assembly of oil-in-water emulsion droplets. *Proceedings of the National Academy of Sciences*, 109(50):20320–20325, 2012.
- [20] Y. He, T. Ye, M. Su, C. Zhang, A. E. Ribbe, W. Jiang, and C. Mao. Hierarchical self-assembly of dna into symmetric supramolecular polyhedra. *Nature*, 452(7184):198–201, 2008.
- [21] J. Homola. Surface plasmon resonance sensors for detection of chemical and biological species. *Chemical reviews*, 108(2):462–493, 2008.
- [22] Y. Ke, L. L. Ong, W. M. Shih, and P. Yin. Three-dimensional structures self-assembled from DNA bricks. *science*, 338(6111):1177–1183, 2012.
- [23] J. Kim and E. Winfree. Synthetic *in vitro* transcriptional oscillators. *Molecular Systems Biology*, 7:465, 2011.
- [24] J. Kim, K. S. White, and E. Winfree. Construction of an *in vitro* bistable circuit from synthetic transcriptional switches. *Molecular Systems Biology*, 1:68, 2006.
- [25] S. Ko, H. Liu, Y. Chen, and C. Mao. Dna nanotubes as combinatorial vehicles for cellular delivery. *Biomacromolecules*, 9(11):3039–3043, 2008.
- [26] D. Kushner. Self-assembly of biological structures. *Bacteriological reviews*, 33(2):302, 1969.
- [27] T. H. LaBean, H. Yan, J. Kopatsch, F. Liu, E. Winfree, J. H. Reif, and N. C. Seeman. Construction, analysis, ligation, and self-assembly of DNA triple crossover complexes. *Journal of the American Chemical Society*, 122(9):1848–1860, 2000.

- [28] N. V. Lavrik, M. J. Sepaniak, and P. G. Datskos. Cantilever transducers as a platform for chemical and biological sensors. *Review of scientific instruments*, 75(7):2229–2253, 2004.
- [29] B. Li, A. D. Ellington, and X. Chen. Rational, modular adaptation of enzyme-free DNA circuits to multiple detection methods. *Nucleic acids research*, 39(16):e110–e110, 2011.
- [30] D. Liu, S. H. Park, J. H. Reif, and T. H. LaBean. DNA nanotubes self-assembled from triple-crossover tiles as templates for conductive nanowires. *Proceedings of the National Academy of Sciences of the United States of America*, 101(3):717–722, 2004.
- [31] W. Liu, H. Zhong, R. Wang, and N. C. Seeman. Crystalline two-dimensional dna-origami arrays. *Angewandte Chemie*, 123(1):278–281, 2011.
- [32] Y. Lu and J. Liu. Functional dna nanotechnology: emerging applications of dnazymes and aptamers. *Current opinion in Biotechnology*, 17(6):580–588, 2006.
- [33] P.-A. Monnard and D. W. Deamer. Membrane self-assembly processes: Steps toward the first cellular life. *The Anatomical Record*, 268(3):196–207, 2002.
- [34] K. Montagne, R. Plasson, Y. Sakai, T. Fujii, and Y. Rondelez. Programming an in vitro DNA oscillator using a molecular networking strategy. *Molecular systems biology*, 7(1):–, 2011.
- [35] K. Namba. Roles of partly unfolded conformations in macromolecular self-assembly. *Genes to Cells*, 6(1):1–12, 2001.
- [36] F. Nédélec, T. Surrey, and E. Karsenti. Self-organisation and forces in the microtubule cytoskeleton. *Current opinion in cell biology*, 15(1):118–124, 2003.
- [37] M. N. O'Brien, M. R. Jones, B. Lee, and C. A. Mirkin. Anisotropic nanoparticle complementarity in DNA-mediated co-crystallization. *Nature materials*, 14(8):833–839, 2015.
- [38] A. Padirac, T. Fujii, and Y. Rondelez. Bottom-up construction of in vitro switchable memories. *Proceedings of the National Academy of Sciences*, 109(47):E3212–E3220, 2012.
- [39] A. Padirac, T. Fujii, and Y. Rondelez. Quencher-free multiplexed monitoring of DNA reaction circuits. *Nucleic acids research*, 40(15):e118–e118, 2012.
- [40] L. Qian and E. Winfree. Scaling up digital circuit computation with DNA strand displacement cascades. *Science*, 3:1196–1201, 2011.
- [41] J. Rizzo, L. K. Gifford, X. Zhang, A. M. Gewirtz, and P. Lu. Chimeric RNA-DNA molecular beacon assay for ribonuclease H activity. *Molecular and Cellular Probes*, 16:277–283, 2002.
- [42] P. W. Rothemund. Folding DNA to create nanoscale shapes and patterns. *Nature*, 440(7082):297–302, 2006.

- [43] P. W. Rothemund, A. Ekani-Nkodo, N. Papadakis, A. Kumar, D. K. Fygenson, and E. Winfree. Design and characterization of programmable dna nanotubes. *Journal of the American Chemical Society*, 126(50):16344–16352, 2004.
- [44] M. Schwarz-Schilling, J. Kim, C. Cuba, M. Weitz, E. Franco, and F. C. Simmel. Building a synthetic transcriptional oscillator. *Cell Cycle Oscillators: Methods and Protocols*, pages 185–199, 2016.
- [45] G. Seelig, D. Soloveichik, D. Y. Zhang, and E. Winfree. Enzyme-free nucleic acid logic circuits. *science*, 314(5805):1585–1588, 2006.
- [46] N. C. Seeman. Dna in a material world. *Nature*, 421(6921):427–431, 2003.
- [47] C. A. Seidel, A. Schulz, and M. H. Sauer. Nucleobase-specific quenching of fluorescent dyes. 1. nucleobase one-electron redox potentials and their correlation with static and dynamic quenching efficiencies. *The Journal of Physical Chemistry*, 100(13):5541–5553, 1996.
- [48] J. Sharma, R. Chhabra, A. Cheng, J. Brownell, Y. Liu, and H. Yan. Control of self-assembly of DNA tubules through integration of gold nanoparticles. *Science*, 323(5910):112–116, 2009.
- [49] W. B. Sherman and N. C. Seeman. A precisely controlled dna biped walking device. *Nano Letters*, 4(7):1203–1207, 2004.
- [50] P. Subsoontorn, J. Kim, and E. Winfree. Ensemble bayesian analysis of bistability in a synthetic transcriptional switch. *ACS synthetic biology*, 1(8):299–316, 2012.
- [51] Y. Tian, Y. He, Y. Chen, P. Yin, and C. Mao. A dnazyme that walks processively and autonomously along a one-dimensional track. *Angewandte Chemie International Edition*, 44(28):4355–4358, 2005.
- [52] M. Weitz, J. Kim, K. Kapsner, E. Winfree, E. Franco, and F. C. Simmel. Diversity in the dynamical behaviour of a compartmentalized programmable biochemical oscillator. *Nature chemistry*, 6(4):295–302, 2014.
- [53] E. Winfree, F. Liu, L. A. Wenzler, and N. C. Seeman. Design and self-assembly of two-dimensional dna crystals. *Nature*, 394(6693):539–544, 1998.
- [54] E. Winfree, F. Liu, L. A. Wenzler, and N. C. Seeman. Design and self-assembly of two-dimensional DNA crystals. *Nature*, 394(6693):539–544, 1998.
- [55] H. Yan, X. Zhang, Z. Shen, and N. C. Seeman. A robust dna mechanical device controlled by hybridization topology. *Nature*, 415(6867):62–65, 2002.
- [56] H. Yan, S. H. Park, G. Finkelstein, J. H. Reif, and T. H. LaBean. DNA-templated self-assembly of protein arrays and highly conductive nanowires. *Science*, 301(5641):1882–1884, 2003.
- [57] D. Yarar, C. M. Waterman-Storer, and S. L. Schmid. A dynamic actin cytoskeleton functions at multiple stages of clathrin-mediated endocytosis. *Molecular biology of the cell*, 16(2):964–975, 2005.
- [58] P. Yin, H. M. Choi, C. R. Calvert, and N. A. Pierce. Programming biomolecular self-assembly pathways. *Nature*, 451(7176):318–322, 2008.

- [59] B. Yurke and A. P. Mills. Using DNA to power nanostructures. *Genetic Programming and Evolvable Machines*, 4:111–122, 2003.
- [60] B. Yurke, A. J. Turberfield, A. P. Mills, F. C. Simmel, and J. L. Neumann. A dna-fuelled molecular machine made of dna. *Nature*, 406(6796):605–608, 2000.
- [61] J. N. Zadeh, C. D. Steenberg, J. S. Bois, B. R. Wolfe, M. B. Pierce, A. R. Khan, R. M. Dirks, and N. A. Pierce. Nupack: analysis and design of nucleic acid systems. *Journal of computational chemistry*, 32(1):170–173, 2011.
- [62] D. Y. Zhang and G. Seelig. Dynamic DNA nanotechnology using strand-displacement reactions. *Nature Chemistry*, 3(2):103–113, 2011.
- [63] D. Y. Zhang and E. Winfree. Control of dna strand displacement kinetics using toehold exchange. *Journal of the American Chemical Society*, 131(47):17303–17314, 2009.
- [64] D. Y. Zhang, A. J. Turberfield, B. Yurke, and E. Winfree. Engineering entropy-driven reactions and networks catalyzed by dna. *Science*, 318(5853):1121–1125, 2007.
- [65] D. Y. Zhang, R. F. Hariadi, H. M. T. Choi, and E. Winfree. Integrating DNA strand-displacement circuitry with DNA tile self-assembly. *Nature Communications*, 4, 2013.
- [66] F. Zhang, J. Nangreave, Y. Liu, and H. Yan. Structural DNA nanotechnology: state of the art and future perspective. *Journal of the American Chemical Society*, 136(32):11198–11211, 2014.
- [67] F. Zhang, S. Jiang, S. Wu, Y. Li, C. Mao, Y. Liu, and H. Yan. Complex wireframe DNA origami nanostructures with multi-arm junction vertices. *Nature nanotechnology*, 10(9):779–784, 2015.
- [68] Y. Zhang and N. C. Seeman. Construction of a dna-truncated octahedron. *Journal of the American Chemical Society*, 116(5):1661–1669, 1994.
- [69] Z. Zhao, Y. Liu, and H. Yan. Organizing dna origami tiles into larger structures using preformed scaffold frames. *Nano letters*, 11(7):2997–3002, 2011.
- [70] J. Zheng, J. J. Birktoft, Y. Chen, T. Wang, R. Sha, P. E. Constantinou, S. L. Ginell, C. Mao, and N. C. Seeman. From molecular to macroscopic via the rational design of a self-assembled 3d DNA crystal. *Nature*, 461(7260):74–77, 2009.